MODELING H_2 ADSORPTION IN CARBON-BASED STRUCTURES

A Thesis

by

KEVIN ANTHONY LAMONTE

Submitted to the Office of Graduate Studies of
Texas A&M University
in partial fulfillment of the requirements for the degree of

MASTER OF SCIENCE

May 2008

Major Subject: Chemical Engineering

MODELING H$_2$ ADSORPTION IN CARBON-BASED STRUCTURES

A Thesis

by

KEVIN ANTHONY LAMONTE

Submitted to the Office of Graduate Studies of
Texas A&M University
in partial fulfillment of the requirements for the degree of

MASTER OF SCIENCE

Approved by:

Chair of Committee,   Perla Balbuena
Committee Members,   Mariah Hahn
                                    Michael Hand
Head of Department,   Michael Pishko

May 2008

Major Subject: Chemical Engineering

ABSTRACT

Modeling H_2 Adsorption in Carbon-Based Structures. (May 2008)

Kevin Anthony Lamonte, B.S., University of North Texas

Chair of Advisory Committee: Dr. Perla Balbuena

Hydrogen storage has been identified as a primary bottleneck in the large-scale implementation of a hydrogen-based economy. Many research efforts are underway to both improve the capacity of existing hydrogen storage systems and develop new systems. One promising area of research is hydrogen physi-sorbed into carbon-based structures such as nanotubes and graphene. Two novel systems consisting of a phthalocyanine salt with a large cation were studied.

Ab initio, density functional theory, and molecular dynamics simulations of tetramethylammonium lithium phthalocyanine (TMA-LiPc) and trimethyl-(2-trimethylazaniumylethyl) azanium phthalocyanine (TMA2-Pc) were undertaken to estimate the H_2 gas-solid adsorption uptake (wt/wt) as a function of pressure and temperature. For TMA-LiPc, the maximum H_2 binding energy was approximately 0.9 kcal/mol for an isolated system and 1.2 kcal/mol for a crystal. H_2 adsorption at the optimal inter-layer distance of 8.49 Å ranged from 2.1% to 6.0% (wt/wt) at 300 K, 2.5% to 6.5% at 273K, 3.3% to 7.2% at 236K, 5.2% to 8.6% at 177K, and 10.4% to 11.7% at 77K. At ILD 10 Å H_2 adsorption was about 1.5% (wt/wt) higher at all points. For TMA2-Pc, the maximum H_2 binding energy was approximately 1.3 kcal/mol for an isolated system and 1.2 kcal/mol for a crystal. H_2 adsorption at the optimal inter-layer distance of 8.12 Å ranged from 0.5% to 2.6% (wt/wt) at 300 K, 0.6% to 2.8% at 273K, 0.8% to 3.2% at 236K, 1.4% to 3.9% at 177K, and 4.5% to 6.0% at 77K. At ILD 10 Å H_2 adsorption ranged from about 0.1% (wt/wt) at 40 bar to 0.5% higher at 250 bar.

The behavior of H_2 adsorption for both TMA-LiPc and TMA2-Pc were compared. The adsorbed H_2 probability density was compared to pair correlation function data and surfaces of constant binding energy. Regions of relatively high H_2 density appear to correlate well with the binding energy, but the total adsorption does not, indicating that the adsorption is driven by factors other than binding energetics.

Lithium ion transport in TMA2-Pc was also investigated for suitability as an electrolyte medium for use in lithium ion battery systems.

To Sesalee

ACKNOWLEDGMENTS

TABLE OF CONTENTS

LIST OF TABLES

LIST OF FIGURES

FIGURE   Page

FIGURE   Page

CHAPTER I

INTRODUCTION

A. Motivation

Hydrogen combustion can theoretically produce three times the energy per mass (~140 MJ/kg) [1] as gasoline combustion (~44 MJ/kg) [2]. For this reason, hydrogen is often promoted as a contender for energy needs traditionally associated with other hydrocarbons such as transportation and consumer power generation. Although hydrogen is currently primarily produced from hydrocarbons, it can also be obtained from electrolysis and thermochemical cracking of water, rendering it both renewable and carbon neutral. However, hydrogen has a very low energy density per unit volume at ambient conditions (~0.0107 MJ/L [2], compared to gasoline at ~31.1 MJ/L [2]), making commercialization difficult.

The United States Department of Energy has published a roadmap defining key technology milestones that must be reached before a large-scale "hydrogen economy" will be feasible [3]. Two of the most critical targets are volumetric to gravimetric energy density ratios that correlate to a weight uptake of 6% and 12%. At 6% weight uptake hydrogen could be used to meet minimum performance goals; at 12% uptake hydrogen could be used extensively throughout the economy. Only one hydrogen storage system noted in the DOE roadmap can meet the minimum goal: an advanced liquified hydrogen storage tank at 8.2%. Other systems fall far short of the goal, including compressed gas (3.7% at 700 bar), standard liquid hydrogen tanks (4.2%), and metal hydrides (1.2% to 3.4%). The DOE roadmap also identifies direct adsorption into carbon nanostructures as a viable option.

The journal model is *IEEE Transactions on Automatic Control.*

Carbon-based systems that have been investigated include single-walled carbon nanotubes (SWNTs), multi-walled carbon nanotubes (SWNTs), carbon fibers, and graphene sheets. Interest in SWNTs in particular has grown sharply due to its potential to directly meet the DOE target: Dillon et al. estimated that SWNTs could adsorb between 5% to 10% wt/wt [4] from temperature programmed desorption spectroscopy measurements, and further measurements by Yamanaka et al. suggest maximum adsorption between 8.5% to 9.5% wt/wt [5]. Though SWNTs can store sufficient hydrogen, total desorption is difficult at room temperature. Also, the high adsorbtion for SWNTs has not been seen in all studies: Poirier et al. tested adsorption of SWNTs and carbon fibers and found adsorption of approximately 2.7% and 0.7% respectively [6]. Computational studies of SWNTs indicate that adsorption can be increased by doping and possibly by introducing defects in the walls [7]. A study of MWNTs by Hou et al. [8] show adsorption between 2% and 4.5% at room temperature depending on tube diameter. Zhang studied several systems based on corannulene [9] and found H_2 adsorption in the range of 0.5% to 2.5% at room temperature. In general, carbon-based systems are promising but do not yet meet the DOE storage targets.

This investigation focuses on two carbon-based systems and estimates the hydrogen uptake properties for both of these systems. One of these systems was also investigated for Li ion transport properties. Additional characteristics are examined to determine the physical feasibility of the models.

B. *Ab initio* / DFT methods

Several quantum chemistry techniques have been developed to predict molecular characteristics from first principles. These techniques can be divided into three ma-

jor categories: *ab initio*, density functional theory (DFT), and semi-empirical methods. *Ab initio* methods refer to techniques that directly solve the time-independent Schrödinger Equation $\Psi H = \Psi E$; the two most common *ab initio* methods are Hartree-Fock and Møller-Plesset perturbation theory [10]. *Ab initio* methods require no parameterization and are considered the most rigorous computations available, however they are also the most computationally expensive methods in use. DFT methods solve for the electron density first using a functional and then back-solve for the wave function Ψ. Though a true universal functional has been proven to exist [11], it has not yet been discovered, so current DFT functionals require parameters fitted to experimental data. Only a few parameters are needed to model the entire periodic table and results are often very close to *ab initio* but an order of magnitude less computationally expensive. As such, DFT is generally considered less formally rigorous than *ab initio* but still close to a fundamental method. Semi-empirical methods are heavily-parameterized models that generally are fitted to work for only the most common atoms and rely on experimental data. Semi-empirical methods often produce results quite close to both *ab initio* and experimental methods, but are not generalizable across the entire periodic table [12] and hence are not considered rigorous, however they are the least computationally expensive method and can model much larger systems than is currently feasible with *ab initio* or DFT.

In this study B3LYP DFT [13] was used to estimate the molecular geometry, charge distribution, crystal structure, H_2 binding energy, dipole moment, and polarizability. AM1 [14] and PM3 [15] semi-empirical methods were used to estimate crystal structure. Hartree-Fock [10] was used for one frequency calculation.

C. Molecular dynamics methods

Molecular dynamics (MD) methods produce results that can be used to obtain statistical thermodynamics properties and hence can be tested at the macro scale. For example, MD results include velocities of all particles that can be related to temperature via [16]

$$\langle v \rangle = \left(\frac{8kT}{\pi m} \right)^{1/2}$$

where $\langle v \rangle$ is the average velocity of all particles in the system, k is the Boltzmann constant, m is the particle mass, and T is the system temperature. Other properties that can be estimated from MD include system properties like pressure and energy and material properties such as the binary diffusion coefficient, viscosity, and ionic conductivity. In this study MD was used to estimate the H_2 uptake (wt/wt), the H_2 self-diffusion coefficient, the H_2 probability density around the solid crystal macromolecules, and the Li ion binary diffusion coefficient.

MD simulates atomic centers as fixed points connected by unbreakable bonds with forces acting on the atoms that depend on the system configuration and empirical parameters. The force functions and parameters taken together are referred to as a "force field"; MD programs may implement one or many force fields. An MD program modifies atomic velocities and forces according to Newton's Second Law of Motion in order to control the total system energy, which is generally defined by a sum of individual contributions like the following:

$$\sum E_K + \sum E_R + \sum E_\theta + \sum E_{ijkl} + \sum E_{vdw} + ... = E_{total} \qquad (1.1)$$

Each energy term above can be expanded in many ways. The terms above are:

- E_K: the kinetic energy of the atomic centers.

- E_R: the bond length potential.

- E_θ: the bond angle potential.

- E_{ijkl}: the dihedral angle potential.

- E_{vdw}: the van der Waal's non-bonded potential, also referred to as the 12-6 Lennard-Jones potential, or simply the Lennard-Jones potential.

All terms are usually defined to be at their minimum at known experimental values. Other terms such as external electric or magnetic fields can be included.

As in statistical thermodynamics, MD simulations use ensembles (canonical, grand canonical, etc.) to fix some combination of volume, temperature, pressure, or energy to particular values and allow the others to fluctuate about the equilibrium value. In this study all of the MD used the NVT ensemble, which fixed the number of molecules, volume, and temperature, and allowed the pressure and energy to fluctuate.

After an MD system has been created and executed, the results may be analyzed with a variety of tools in order to compare to experimental results. The first step in analysis is verifying that the MD system is both energetically and mechanically stable. Energetic stability is easily verified from the MD results (in this case, the DL_POLY OUTPUT file). For these systems, energetic stability is assured when the total system energy is at (or oscillating about) the minimum. Only data collected during this time period might be physically realizable and is thus appropriate to compare against experimental data. Figure 1 shows one example of the energy vs time behavior of a system. For this system, the configuration data is recorded between time steps 300000 ps and 800000 ps, with the energy minimum first achieved near 100000 ps. Since the system is fluctuating around the energy

minimum during the recording phase, all of the recorded configuration data will be at an energetically stable state and can be used for further analysis.
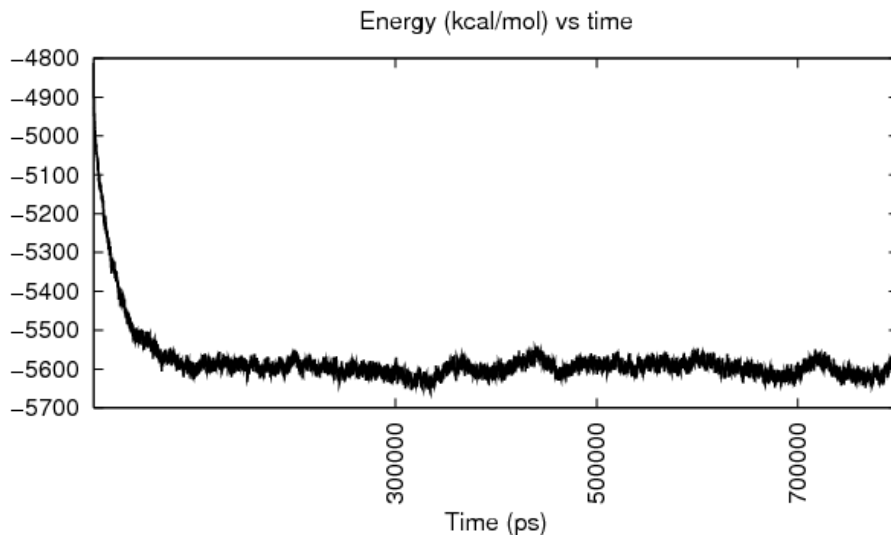
Fig. 1. Example of energy versus time

Mechanical stability can be verified via the *velocity autocorrelation function* (VACF). The VACF is typically defined as [17]

$$VACF(t) = \frac{\sum_{i}^{N_\tau} \sum_{j}^{N} \vec{v_j}(\tau)\vec{v_j}(\tau + t)}{N_\tau N \sum_{i}^{N_\tau} \sum_{j}^{N} \vec{v_j}(\tau)\vec{v_j}(\tau)}$$

where N is the number of particles, N_τ is the number of "time origins", τ is the current time origin, and $\vec{v_j}$ is the velocity of the jth particle. For gas- and liquid-phase systems, the VACF starts at 1 and begins a damped oscillation about zero; most gas systems such as the example in Figure 2 damp very quickly. Solid-phase system also oscillate about zero, but may not be damped. In all phases, so long as the oscillations are not growing, the system is mechanically stable. The DL_POLY

utility program `vacf.f` is used to compute the VACF from the MD results (in this case, the DL_POLY `HISTORY` file).
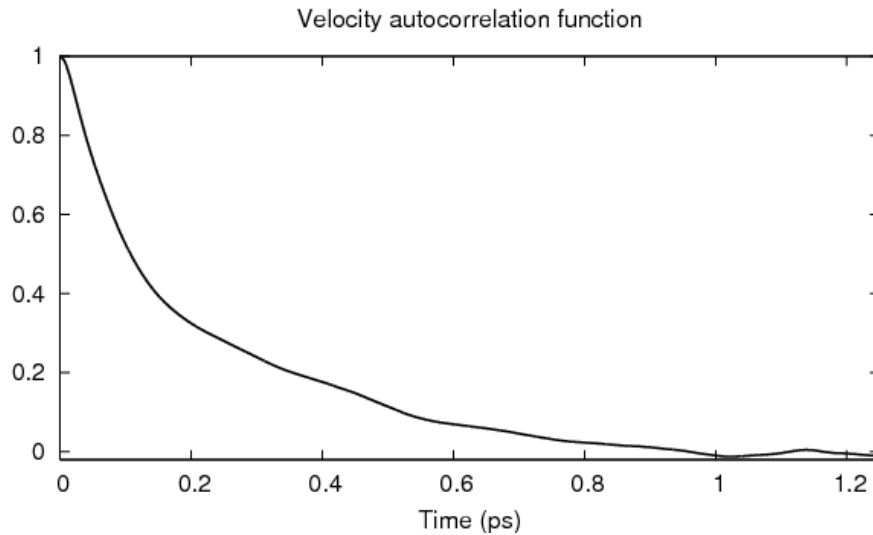
Fig. 2. Example of velocity autocorrelation function

Once energetic and mechanical stability have been assured, the results can be analyzed for insights into system motion, structure, and energetics, and compared to experimental properties.

The self-diffusion coefficient of a fluid can be computed directly from MD results via the Einstein relation [18]:

$$D = \frac{1}{6} \lim_{t \to \infty} \frac{1}{(N-1)} \sum_{i=1}^{N} \frac{d}{dt} \left\langle [\mathbf{r}_i(t) - \mathbf{r}_i(t_0)]^2 \right\rangle$$

The limit is the slope of the *mean square displacement* (MSD) function as $t \to \infty$. The MSD is also equal to half the integral of the VACF. Figure 3 shows one example of the MSD function of a system. The DL_POLY utility program `msd.f` is used to compute the MSD from the MD results (in this case, the DL_POLY `HISTORY` file).
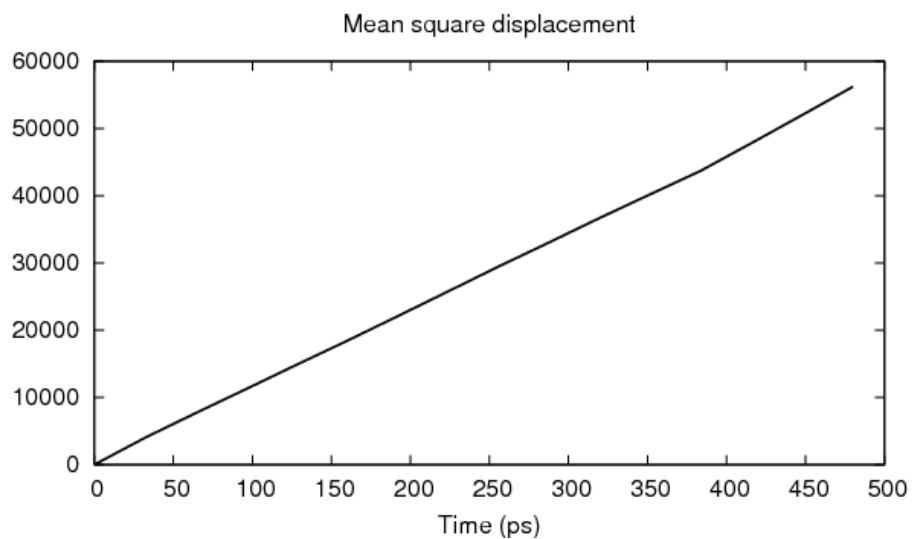
Fig. 3. Example of mean square displacement function
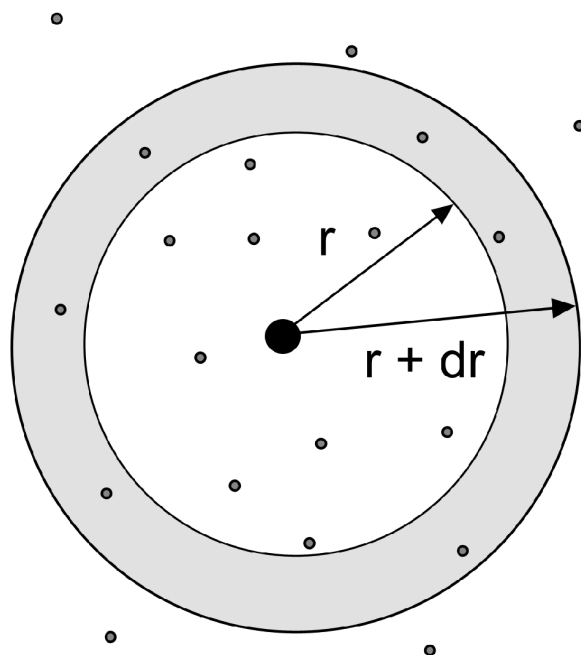
Fig. 4. Graphical depiction of pair correlation function $g_{ij}(r)$

The *pair correlation function* $g_{ij}(r)$ is a measure of the semi-stable structure present in a system. $g_{ij}(r)$ is measured by counting the number of particles of type j located in a shell within a certain distance r of a particle of type i [19] as depicted in Figure 4 and normalizing this value by dividing it by the bulk density of element j. As r goes to a large value beyond which the two particles do not interact, $g_{ij}(r)$ goes to 1. (Some texts use the term *radial distribution function $g(r)$* synonymously with $g_{ij}(r)$ and some define $g(r)$ as the non-normalized count of particles, e.g. $g(r) = \rho g_{ij}(r)$. For clarity, this study will always use the term *pair correlation function* and mean the normalized value.) Every pair of atom types has a distinct pair correlation function, so for example in a simulation containing only water molecules three pair correlations would be produced: one for oxygen and oxygen, one for oxygen and hydrogen, and one for hydrogen and hydrogen. DL_POLY reports the $g_{ij}(r)$ data in the RDFDAT file. An example of $g_{ij}(r)$ between a solid-phase TMA-LiPc site and a gas-phase H_2 is given in Figure 5. In this example one can see a strong peak value of 7 at about 4.5 Å, indicating that in general up to 7 times the bulk density of H_2 particles are near the atomic site on the crystal in a shell between about r=4 Å and r=4.5 Å. This corresponds to the ring around the TMA-LiPc cation in the corresponding H_2 density surface shown in Figure 6.

It is possible to directly visualize the H_2 probability density around the crystal by analyzing the configuration data in the MD results. Given a sequence of N system configurations, one can count the number of configurations in which a particular atom type was near a fixed point and divide that by N to yield a probability of finding that atom at that point. So long as the cutoff distance is smaller than the atomic radius, one can say that any atom within the cutoff distance of that point was an atom that was "at" that point. After the probability has been computed at regular grid points in a three-dimensional space standard tools can be used to plot

Pair correlation function
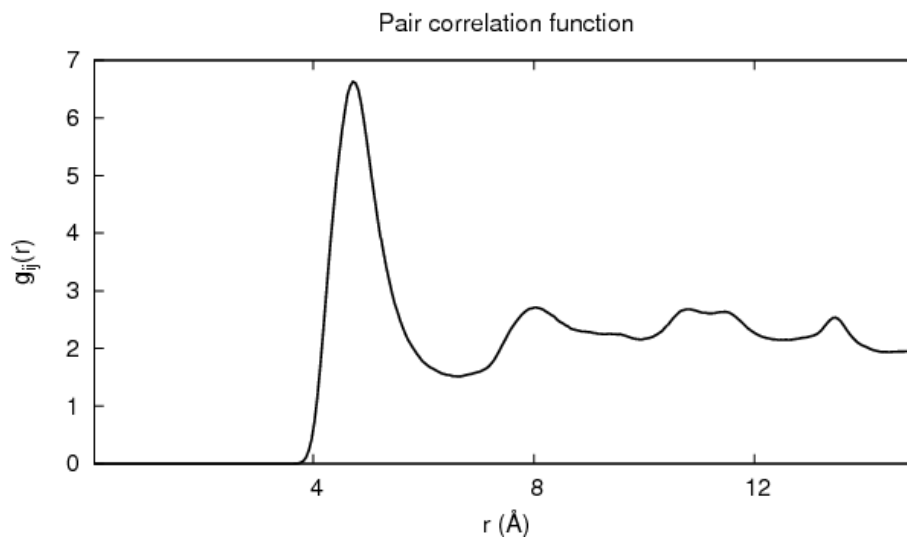
Fig. 5. Example of pair correlation function

the three-dimensional constant probabiliy surfaces.

DL_POLY did not ship with a utility to perform this analysis, so the ChENL application `smoosh_history` was written to do so. It reads in the DL_POLY `HISTORY` file, computes the three-dimensional grid of probability points, and writes the grid to a Gaussian 2003 formatted "cube file" which can be rendered in GaussView. The cutoff distance is 0.7 Å and the spacing between grid points was 0.33 Bohr, corresponding to the "coarse" grid option of GaussView. Figure 6 shows an example of the 20% probability surface for one system.

The surfaces of constant physi-sorption binding energy can also be visualized via the ChENL application `h_lj_density`. These surfaces correspond to the $\sum E_{vdw}$ term of Equation 1.1, i.e. at any point along the surface of constant binding energy ΔE the sum of van der Waals interactions between one H_2 molecule and every atom of the macromolecule is ΔE. One type of surface produced is that of a single crystal unit cell as shown in Figure 7; this surface directly corresponds to the *ab initio* / DFT
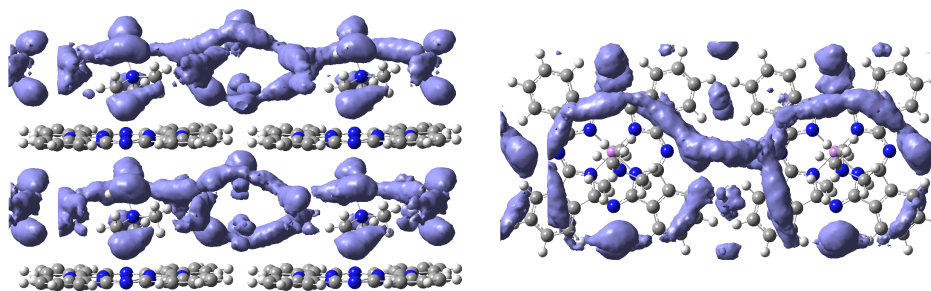
Fig. 6. Example of H_2 probability density surface

case and can be used to estimate the expected H_2 binding energies for *ab initio* / DFT systems. Another type of surface produced is that of a unit cell within a crystal of infinite extent as shown in Figure 8. This surface corresponds to the energy within a full crystal like those tested by MD.

D. Computational tools

The *ab initio*, DFT, and semi-empirical calculations were performed by the Gaussian 2003 suite (G03) [20]. The MD simulations were performed by the DL_POLY 2.0 molecular simulation package [21]. GaussView 3.09 [22], Cerius^2 [23], and GNUPLOT [24] were used for visualization. GNU Octave [25] was used for parameter fitting and other analyses. File format conversions and some analyses were performed by the ChENL suite [26].

E. Goals

Tetramethylammonium lithium phthalocyanine (TMA-LiPc) and trimethyl- (2-trimethylazaniumylethyl) azanium phthalocyanine (TMA2-Pc) were studied to estimate H_2 adsorption properties. Further investigation into lithium ion trans-
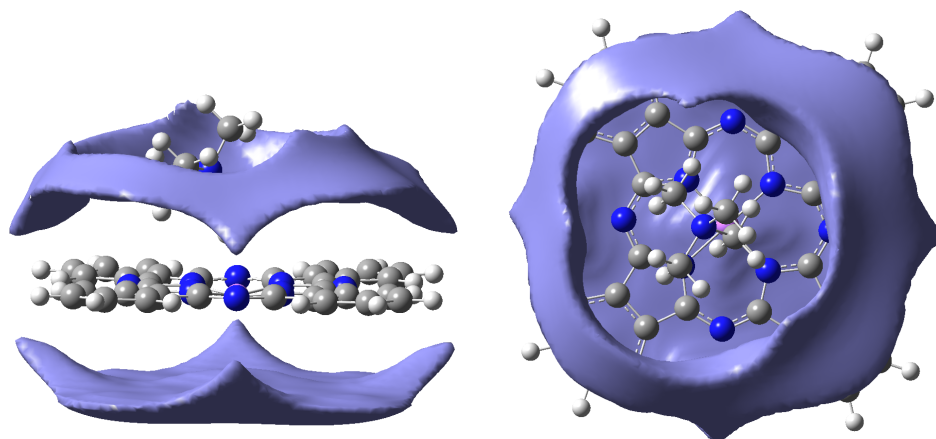
(a) 0.5 kcal/mol
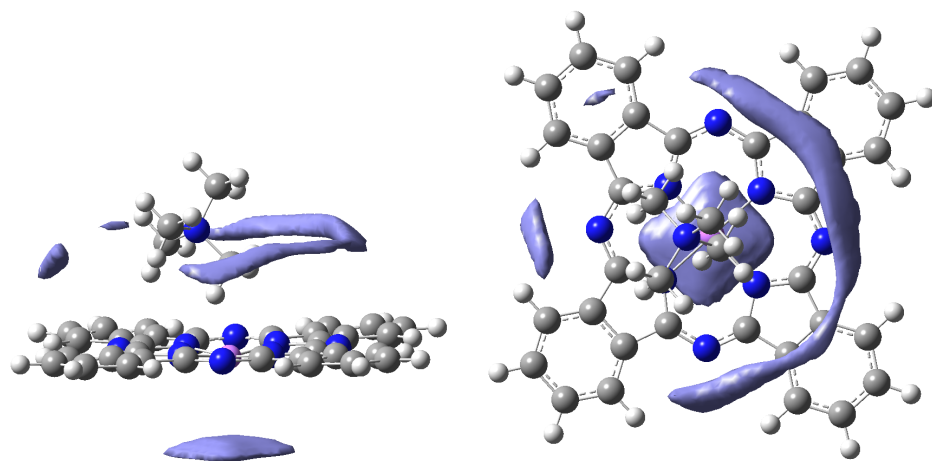
(b) 0.9 kcal/mol

Fig. 7. Example of H_2 single unit cell binding energy surfaces
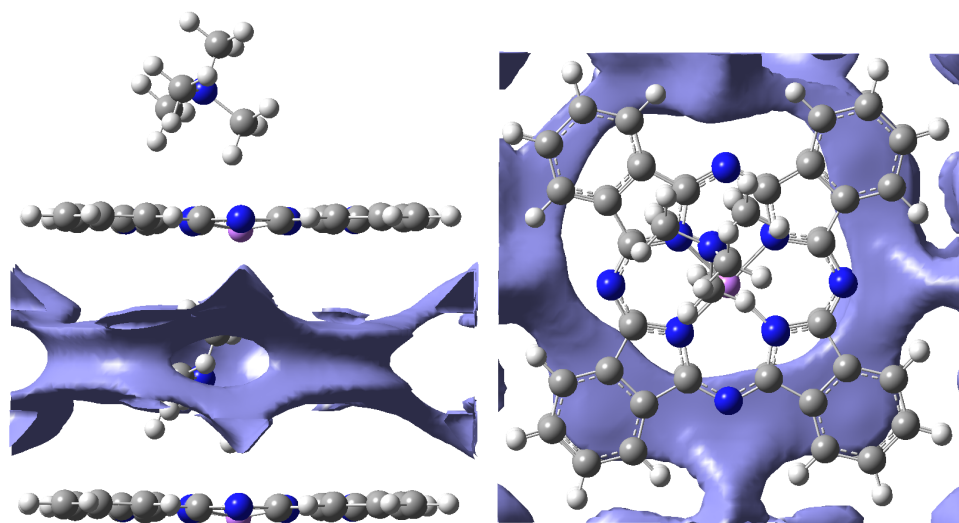
(a) 0.9 kcal/mol
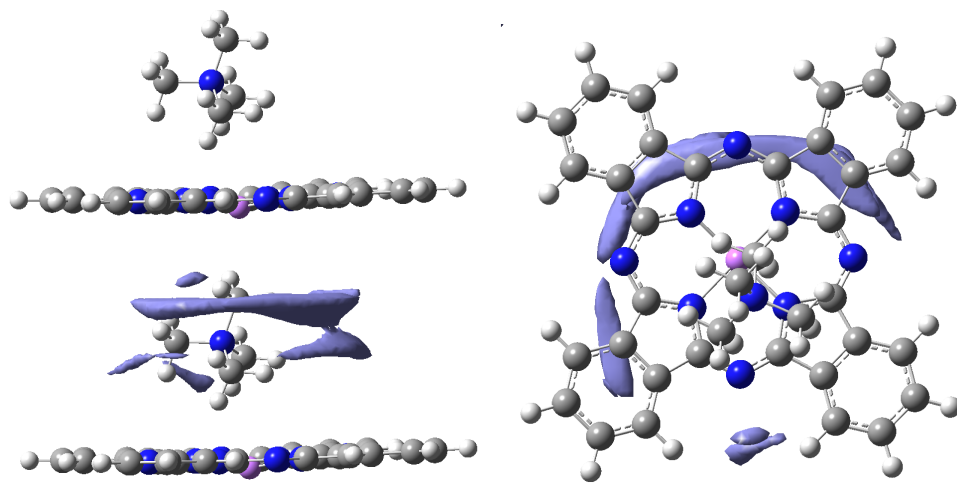
(b) 1.2 kcal/mol

Fig. 8. Example of H_2 infinite crystal binding energy surfaces

port in TMA2-Pc was also undertaken. The overall procedure followed through this study was as follows:

1. The geometry of a crystal unit monomer was estimated from *ab initio* / DFT.

2. A crystal structure of the system was proposed based on *ab initio* / DFT and experimental data.

3. Parameter values for the MD force field were estimated from *ab initio* / DFT.

4. The MD simulations were built and executed.

5. The MD results were analyzed for adsorption and transport properties.

CHAPTER II

H$_2$ ADSORPTION IN TETRAMETHYLAMMONIUM LITHIUM PHTHALOCYANINE (TMA-LIPC)

A. Optimized geometry

B3LYP DFT with a basis set of 6-31g(d,p) was used to optimize the geometry of a single molecule; the resulting geometry is shown in Figure 9. Larger basis were attempted but proved computationally infeasible for the overall analysis. The computed dipole moment was 14.23 Debye and the volumetric polarizability was 631.08 Bohr^3 = 9.352×10^{-23} cm^3. The Mulliken charge distribution is shown in Figure 10. The charges range from -0.614 to +0.406; the maximum values are in the inner ring carbon and nitrogen atoms on the phthalocyanine (Pc).

(a) Top   (b) Side
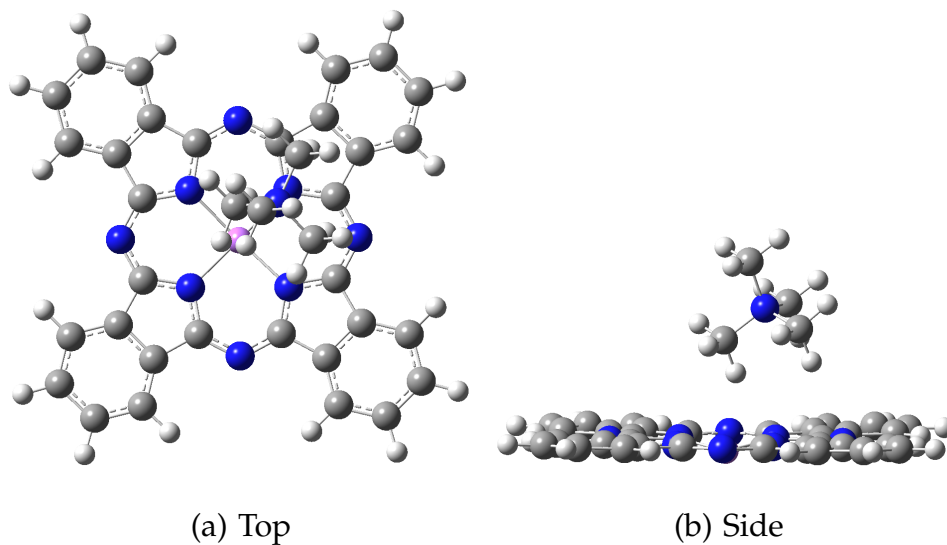
Fig. 9. TMA-LiPc optimized geometry
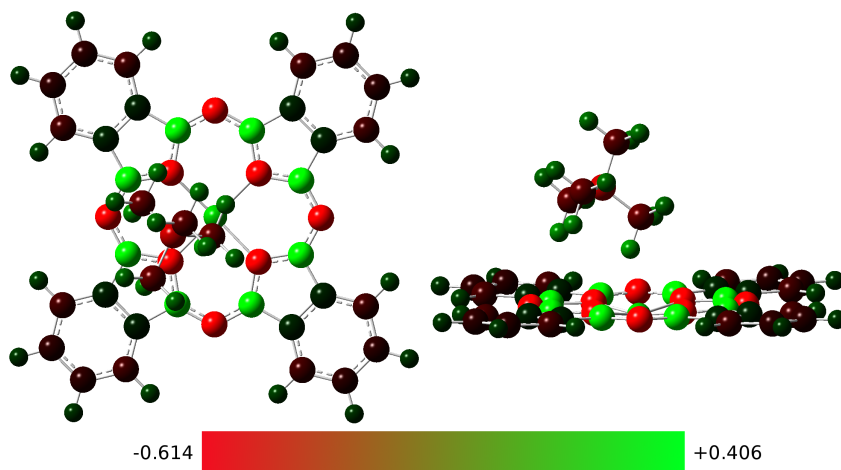
Fig. 10. TMA-LiPc charge distribution

B. Crystal structure

This system is not yet known to have been synthesized, and similar systems were not found in the Cambridge Structural Database [27].

DFT with the B3LYP/6-31g(d,p) basis set was used to optimize a dimer system. The initial and final configurations are shown in Figure 11. The initial distance between molecules was 8.36 Å. During optimization the two TMA-LiPc units separated slightly and the two Pc tilted to form an angle of about 36 degrees. The final distance between the TMA cations was 8.24 Å and the average distance between corresponding atoms was 8.49 Å.

Several larger systems were attempted at AM1 and PM3, but only one AM1 fully completed (the rest failed due to errors). MD systems (using the TMA2-Pc Li ion force field described in Chapter IV) were also run at various temperatures. Resulting crystal structures from the AM1 and MD are shown in Figure 12. It is not immediately clear from these structures if TMA-LiPc forms a regular crystal

(a) Beginning structure   (b) Ending structure
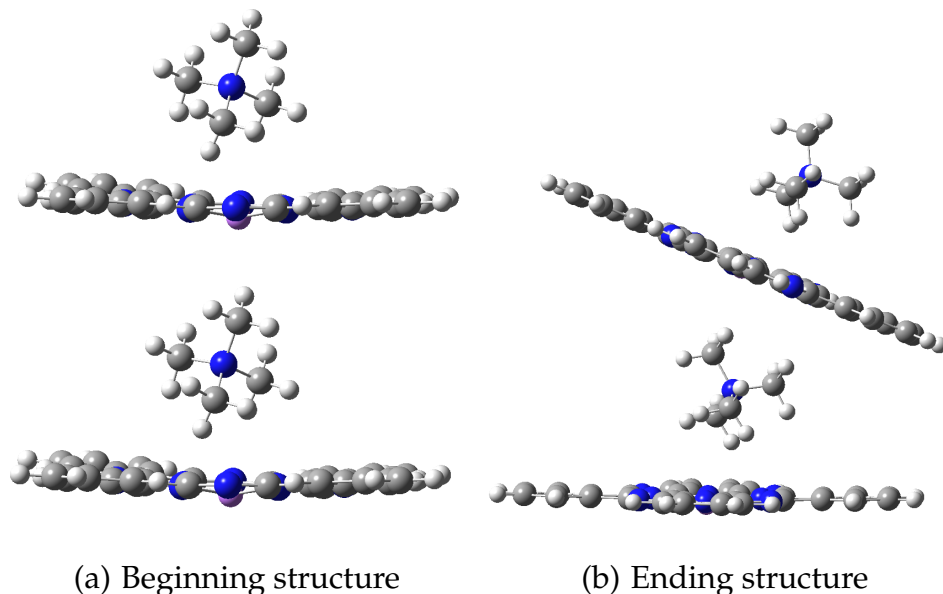
Fig. 11. TMA-LiPc optimized dimer

solid. The AM1 system does seem to indicate that a regular T-shaped structure may result with more TMA-LiPc units in the system, however the MD results show no discernible pattern. The MD force field does not seem to model this particular system very well, despite its basis in successful general force fields.

C. MD force field

The MD simulations were designed to estimate the physi-sorption behavior of gaseous H_2 in solid TMA-LiPc. Solid TMA-LiPc was therefore set as a system of fixed atom centers and H_2 was allowed to move freely, and the only interactions included were non-bonded van der Waals interactions modeled using the 12-6 Lennard-Jones potential with parameters derived from the Lorentz-Berthelot mixing rules:

$$E_{vdw} = 4\epsilon_{ij}\left(\left(\frac{\sigma_{ij}}{r}\right)^{12} - \left(\frac{\sigma_{ij}}{r}\right)^{6}\right)$$
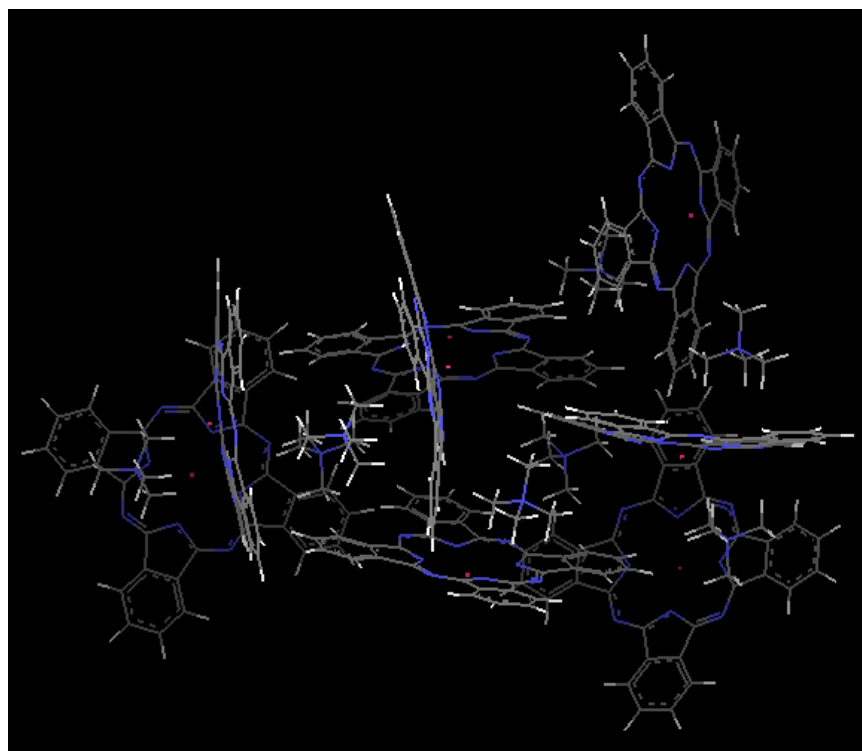
(a) AM1
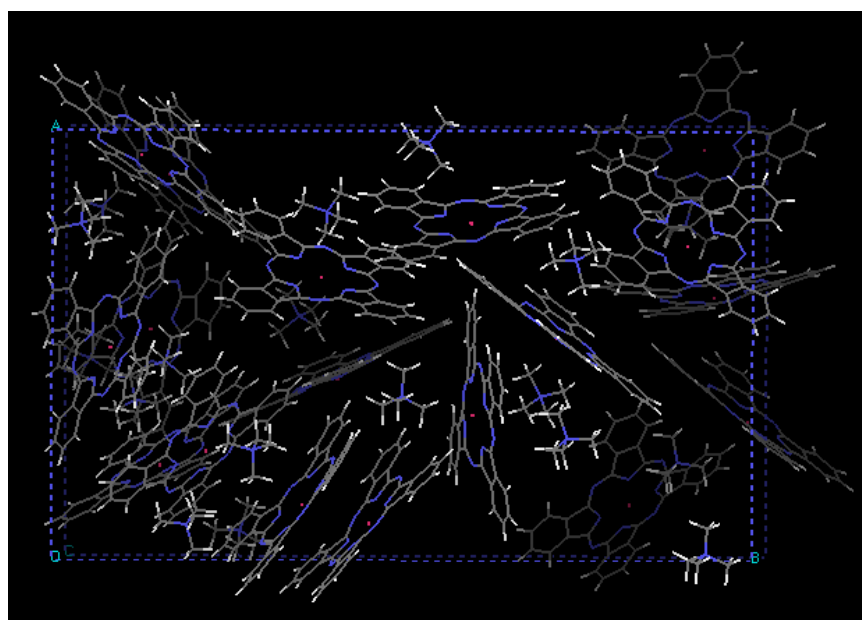
(b) MD

Fig. 12. TMA-LiPc crystal structure

$$\epsilon_{ij} = \sqrt{\epsilon_i \epsilon_j}$$

$$\sigma_{ij} = \frac{\sigma_i + \sigma_j}{2}$$

where ϵ_i is the non-bonded minimum energy between two molecules of species i and σ_i is the molecular diameter of species i.

TMA-LiPc has a large dipole moment and induces a dipole in H_2 at close distances, which in turn produces a net increase in binding energy over that predicted by a general force field. It was thought that the induced dipole potential might measurably affect the mean adsorption behavior, so it was decided to modify the van der Waals interaction to include some portion of the induced dipole potential.

The mean potential between a permanent dipole and an induced dipole is given by [28]:

$$\Gamma_{ij} = -\frac{\alpha_i \mu_j^2 + \alpha_j \mu_i^2}{(4\pi\epsilon_0)^2 \, r_{ij}^6}$$

where α_i is the molecular polarizability, μ_i is the dipole moment, ϵ_0 is the permittivity of free space, and r_{ij} is the distance between the two molecules. For convenience α_i is converted to the volumetric polarizability [29] with units of volume via:

$$\alpha' = \frac{\alpha}{4\pi\epsilon_0}$$

leading to

$$\Gamma_{ij} = -\frac{\alpha'_i \mu_j^2 + \alpha'_j \mu_i^2}{(4\pi\epsilon_0) \, r_{ij}^6}$$

A custom force field developed by Gomez-Gualdron estimates the net physisorbtion binding energy of the combined 12-6 Lennard-Jones and mean induced dipole interaction potentials by apportioning the total induced dipole interaction

to each molecule site and refitting the Lennard-Jones parameters:

$$E_{vdw,i} = 4\epsilon_{ij}\left(\left(\frac{\sigma_{ij}}{r}\right)^{12} - \left(\frac{\sigma_{ij}}{r}\right)^{6}\right) + w_i \Gamma_{ij} \tag{2.1a}$$

$$= 4\epsilon_{ij}\left(\left(\frac{\sigma_{ij}}{r}\right)^{12} - \left(\frac{\sigma_{ij}}{r}\right)^{6}\right) - w_i \frac{1}{4\pi\epsilon_0} \frac{\mu_{molecule}\alpha'_{H_2} + \mu_{H_2}\alpha'_{molecule}}{r^6} \tag{2.1b}$$

$$\approx 4\epsilon'_{ij}\left(\left(\frac{\sigma'_{ij}}{r}\right)^{12} - \left(\frac{\sigma'_{ij}}{r}\right)^{6}\right) \tag{2.1c}$$

Here the original force field parameters are ϵ_{ij} and σ_{ij} and the refitted parameters are ϵ'_{ij} and σ'_{ij}. w_i is a weighting factor specific to one TMA-LiPc site. Γ_{ij} as a function of r^{-6} can be computed up front. The dipole moment of H_2 is zero; the volumetric polarizability of H_2 is 8.21×10^{-25} cm^3 [30]; the dipole moment of TMA-LiPc computed using B3LYP/6-31g is 14.4 Debye. With these values Γ_{ij} is:

$$\Gamma_{ij} = -\frac{1056250}{r_{ij}^6} \text{ meV}$$
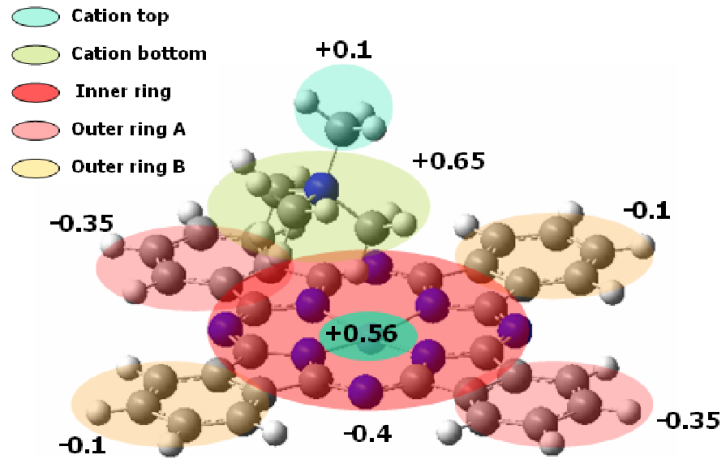
Fig. 13. TMA-LiPc charge regions

Gomez-Gualdron's method to determine the weighting factors w_i was as fol-

lows:

1. The induced dipole moment on H_2 was computed for multiple locations of H_2 with respect to TMA-LiPc along several paths. For each point on the path, the H_2 was oriented with the bond along the line connecting the center of the TMA-LiPc and the site of interest. Each path consisted of 11 points in total: 6 points between 2.5 Å and 5 Å inclusive spaced 0.5 Å apart, and five points from 6 Å to 10 Å inclusive space 1 Å apart. Distance was measured from the site on TMA-LiPc to the near atom of the hydrogen molecule.

2. The arithmetic average of the dipole moment on H_2 for all of the points along one path was denoted $(\mu_i)_{av}$.

3. The paths were chosen according to the six regions depicted in Figure 13. The regions were chosen based on the atomic charges of TMA-LiPc computed from the electrostatic potential. Each region contains atoms of similar charge and close proximity. The regions were named cation top, cation bottom, inner ring, outer ring A, outer ring B, and Li.

4. A separate path was computed for each atom type within a region, e.g. both inner ring C and inner ring N each had a separate path.

5. Only paths corresponding to C, N, and Li sites were included. Paths for H sites were computed but discarded since they had very little contribution.

6. The partial contribution to the induced dipole from each region was denoted S_i and computed as
$$S_i = \frac{(\mu_i)_{avg} N_i}{\sum (\mu_i)_{avg} N_i}$$
where N_i is the number of atoms of a particular species within a region.

7. The weighting factor w_i for a path was the partial contribution from all of the like atoms within that region towards S_i:

$$w_i = \frac{S_i}{N_i}$$

Table I shows the final weighting factors. The majority weights were assigned to the inner ring carbons and nitrogens, the center lithium, and the cation top carbon.

Table I. TMA-LiPc weighting factors w_i

Atom type	$(\mu_i)_{avg}$	N_i	S_i	w_i
Outer ring A - C	0.06	8	12.87	0.016
Outer ring B - C	0.05	8	10.72	0.013
Inner ring - C	0.17	8	36.46	0.046
Inner ring - N	0.11	8	23.59	0.029
Cation - C and N	0.08	4	8.58	0.021
Cation top - C	0.15	1	4.02	0.040
Li	0.14	1	3.75	0.038

Once the weighting factors were determined, the Lennard-Jones parameters were refitted according to Equation 2.1. Table II shows both the original and the refitted parameters. In all cases, the refitted parameters had lower σ'_{ij} and higher ϵ'_{ij}, meaning the H_2 would be able to approach closer to the site of interest and would also have greater binding energy at the energy minimum. Figure 14 shows one example of the original and refitted Lennard-Jones potential functions, in this case for the inner ring carbon.

H_2 was modeled as a single site with parameters from [31]; C and N used parameters from DREIDING [32]; Li used the same values as [33].
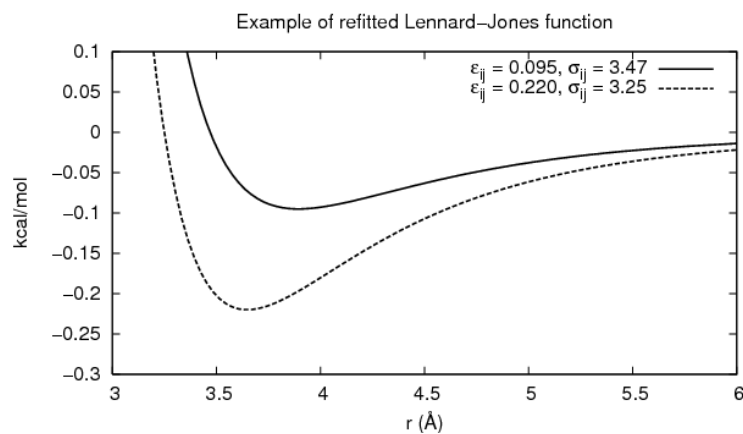
Fig. 14. Refitted Lennard-Jones potential functions

Table II. TMA-LiPc refitted Lennard-Jones parameters

Atom type	ϵ_i kcal/mol	σ_i Å	w_i	ϵ'_i kcal/mol	σ'_i Å
H	0.068	2.96	0.000	0.068	2.96
Outer ring A - C	0.095	3.47	0.016	0.180	3.25
Outer ring B - C	0.095	3.47	0.013	0.176	3.30
Inner ring - C	0.095	3.47	0.046	0.220	3.25
Inner ring - N	0.077	3.26	0.029	0.120	3.05
Cation - C	0.095	3.47	0.021	0.190	3.30
Cation - N	0.077	3.26	0.021	0.100	3.10
Cation top - C	0.095	3.47	0.040	0.210	3.25
Li	0.036	2.37	0.038	0.230	2.55

D.   MD procedure

For the MD crystal structure, a simple stacked cubic system was chosen with 8.49 Å as the inter-layer distance (ILD) and 13.85 Å as the inter-molecule distance in accordance with earlier studies involving phthalocyanine [33]. Molecules were arranged in a $3 \times 3 \times 2$ structure as depicted in Figure 15. An additional gas-phase volume containing 770 H_2 molecules was appended to each system with the gas-phase volume chosen such to match the desired initial pressure. The pressure in the gas-phase region was approximated by the ideal gas law. The H_2 molecules were simulated as single-site Lennard-Jones hard spheres and initially arranged in a uniform grid within the gas-phase region. A rectangular orthorhombic periodic boundary condition was used. The TMA-LiPc molecules were frozen and only Lennard-Jones interactions were allowed between them and the H_2 molecules and between pairs of H_2 molecules. Each simulation ran for a total of 800 ps, with the first 300 ps used to reach equilibrium. System configurations were recorded every 2 ps for the remaining 500 ps, for a total of 251 recorded system configurations. For each system configuration, the percent weight uptake of H_2 in the crystal was calculated and the number of H_2 molecules in the gas phase were counted to determine the gas-phase pressure. The weight uptake is the ratio of mass of H_2 adsorbed over mass of crystal plus mass of H_2 adsorbed. All H_2 molecules not located within the gas-phase region were assumed to be adsorbed.
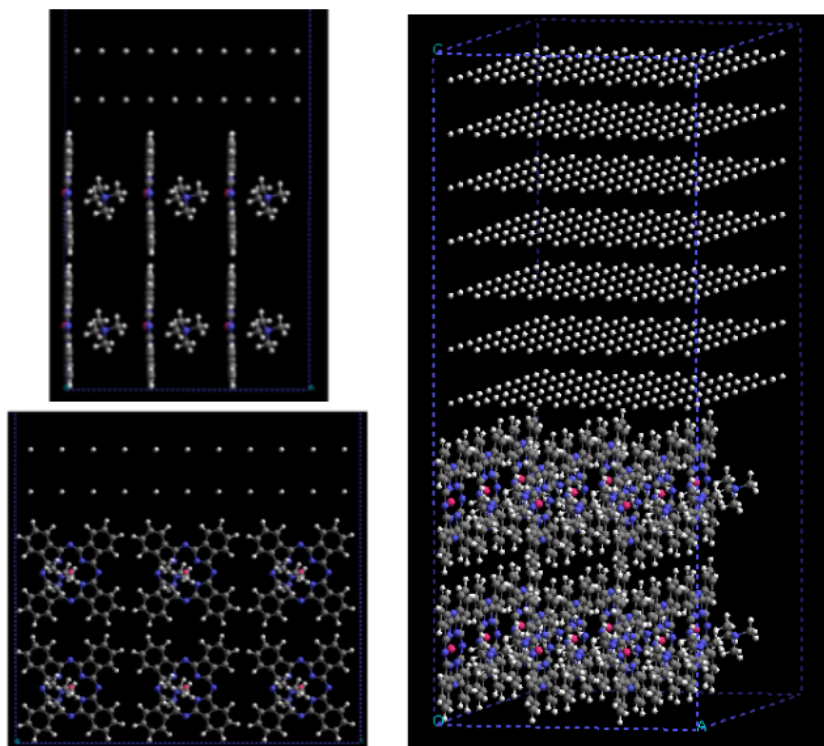
(a) Start
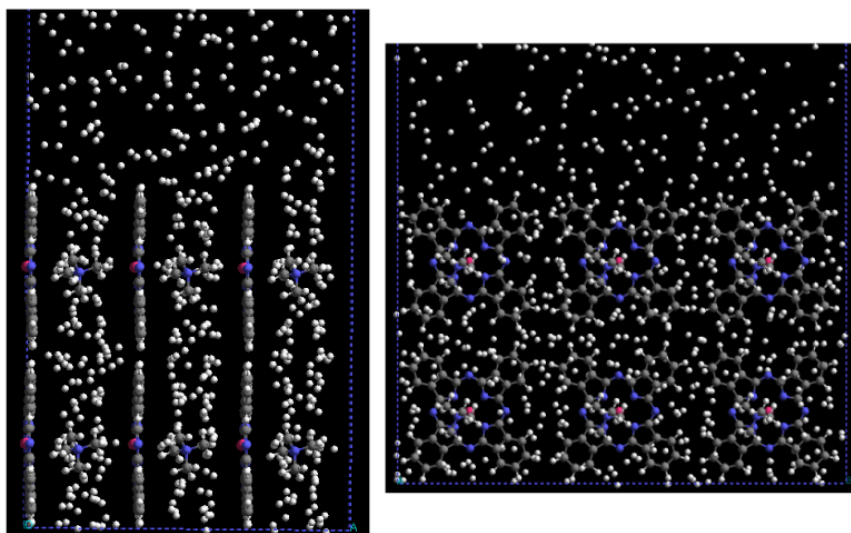
(b) End

Fig. 15. TMA-LiPc start and end configurations

E.   Results and discussion

1.   H$_2$ adsorption

The H$_2$ adsorption isotherms are shown in Figure 16. The raw data is reported in Appendix A Table VIII.

At room temperature the adsorption ranges from 2% at 43 bar to 7% at 277 bar. The maximum possible adsorption appears to be about 12% at ILD 8.49 Å and 13% at ILD 10 Å at T = 77 K. As expected, the adsorption is directly proportional to pressure and inversely to temperature. Also the adsorption is about 1.5% (wt/wt) higher at ILD 10 Å than at ILD 8.49 Å for all pressures and temperatures. This system can meet the DOE minimum target of 6% at temperatures below 177 K and the ultimate performance goal of 12% at temperatures below 77 K.

2.   H$_2$ self-diffusion coefficient

The self-diffusion coefficient of H$_2$ should differ markedly at the gas/solid interface than for the pure species if the H$_2$ is in fact adsorbing into the solid. To test this, MD simulations of pure gas H$_2$ were created using the same conditions and force fields as the gas/solid systems. Figure 17 shows the H$_2$ self-diffusion coefficient as a function of pressure and temperature and ILD. The raw data is reported in Appendix A Table IX. Figure 18 shows how the H$_2$ self-diffusion coefficient compares between the gas/solid systems (all points from ILD 8.49 Å) and the pure gas systems. In all cases, the H$_2$ self-diffusion coefficient is indeed lower in the gas/solid systems. As expected, the self-diffusion coefficient is directly proportional to temperature and inversely to pressure. However, it does not seem to relate correlate concisely with ILD. At low temperatures, the self-diffusion coefficient is lower at ILD 10 Å, but at higher temperatures it seems to be essentially identical
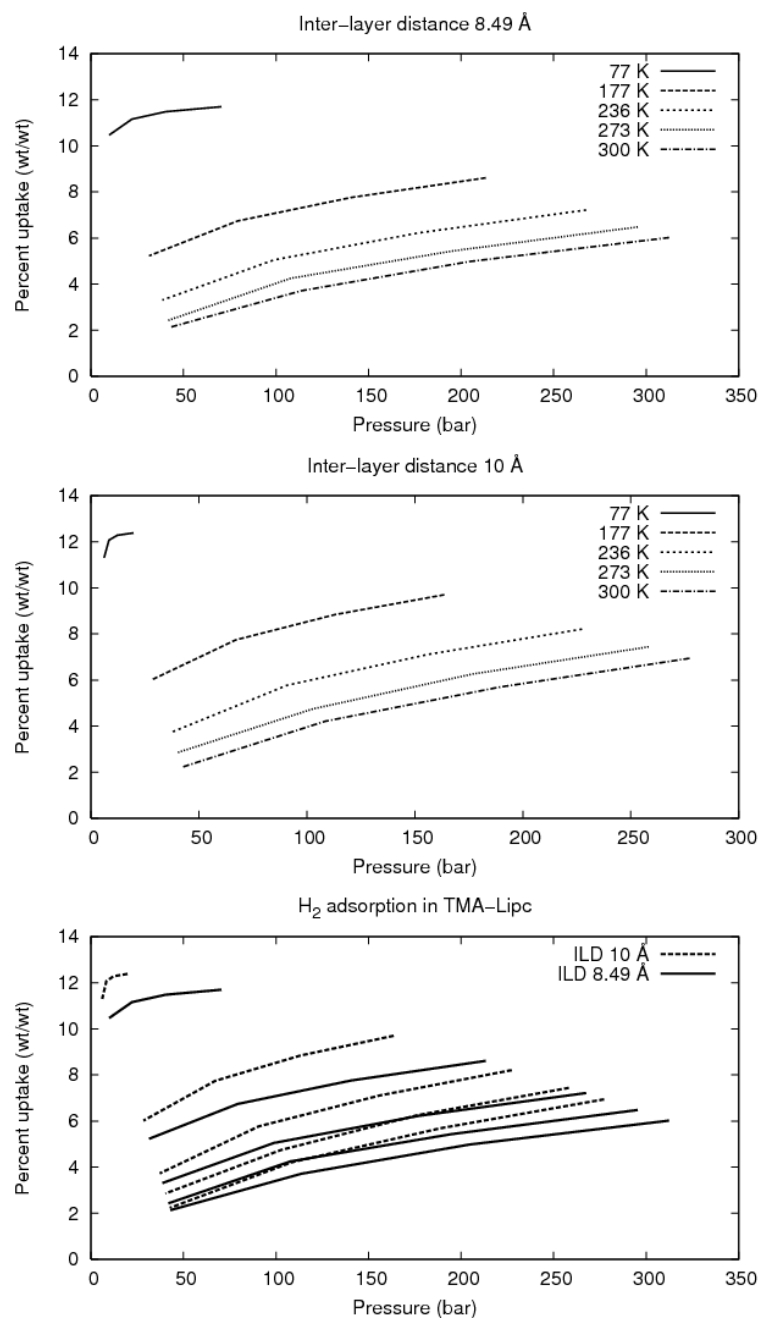
Fig. 16. TMA-LiPc adsorption isotherms

between ILD 10 Å and ILD 8.49 Å.

3.   Pair correlation functions

The $g_{ij}(r)$ pair correlation functions can indicate if the adsorbed H_2 tends to accumulate in particular areas around the macromolecule. Figure 19 shows the $g_{ij}(r)$ pair correlation function between the center nitrogen in the TMA cation and the H_2 gas at different pressures, temperatures, and ILD. In all cases, there is a strong peak at r = 5 Å. In the first two graphs there is also a common secondary peak between r = 9 Å and r = 11 Å.

The first graph is at approximately constant pressure and ILD and varying temperature. The 177 K and 213 bar line is lower than at 300 K and 204 bar; this indicates that since the bulk density is greater at lower temperature the total adsorption near the cation is higher for T = 177 K than at T = 300 K. The second graph is at constant temperature and ILD and varying pressure. The trend is that at higher pressure the value is lower, indicating that since the bulk density is greater at higher pressure; this is consistent with the isotherms. The final graph is at constant pressure and temperature and varying ILD. In this case the two lines are essentially identical between r = 0 Å and r = 7 Å, but differ significantly between r = 7 Å and r = 12 Å. The difference in adsorption between ILD 8.49 Å and ILD 10 Å cannot be inferred from the pair correlation function alone.

4. H_2 adsorption region

The H_2 density probability corresponding to the cases of the $g_{ij}(r)$ pair correlation functions above were then generated directly from the DL_POLY HISTORY file. Figure 20 shows the 20% H_2 probability densities at ILD 8.49 Å, 177 K, 213 bar and
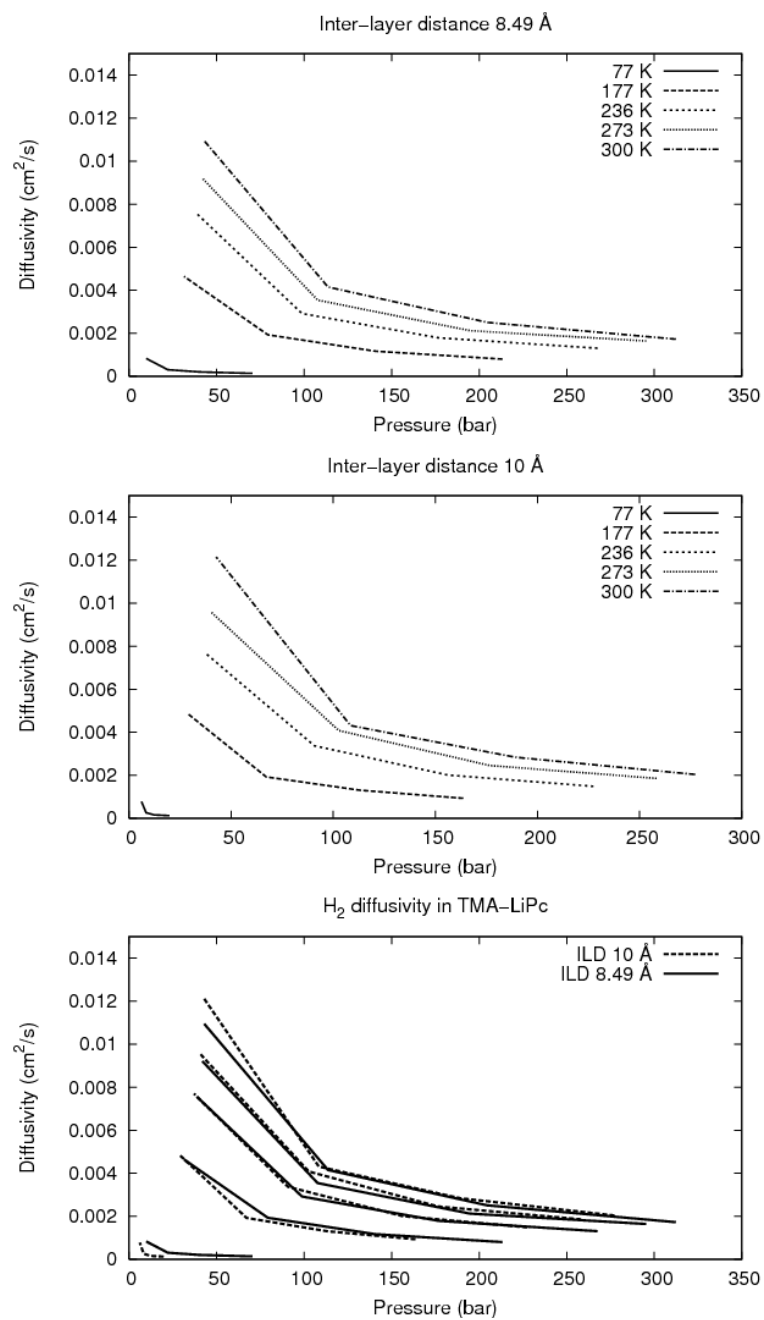
Fig. 17. TMA-LiPc H_2 self-diffusion coefficient
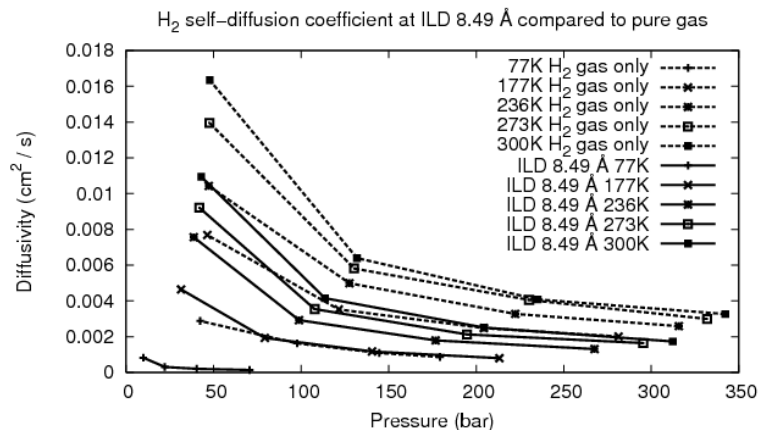
Fig. 18. TMA-LiPc H_2 self-diffusion coefficient comparison with pure gas

ILD 8.49 Å, 300 K, 204 bar. Figure 21 shows the 20% H_2 probability densities at
ILD 8.49 Å, 177 K, 31 bar, ILD 8.49 Å, 177 K, 79 bar, and ILD 8.49 Å, 177 K, 213
bar. Figure 22 shows the 5% H_2 probability densities at ILD 8.49 Å, 300 K, 42.655
bar and ILD 10 Å, 300 K, 42.919 bar. As in the $g_{ij}(r)$ plots above, one can see that
as temperature decreases, the high-adsorption region increases (Figure 20); and as
pressure increases, the high-adsorption region increases (Figure 21). However, the
behavior as ILD increases from 8.49 Å to 10 Å is different: the high-adsorption
region changes shape and splits into two rings separated by about 1.5 Å.

This explains the behavior of the $g_{ij}(r)$ plot of Figure 19 C. The initial peak at r =
5 Å corresponds to the adsorption region immediately surrounding the cation and
is controlled by the fact that the hard-sphere limit σ_{ij} for the TMA outer hydrogens
is ~3 Å, making the distance between the center nitrogen and the Lennard-Jones
minimums of the TMA hydrogens about 5 Å. The behavior between r = 7 Å and r
= 12 Å reflects the differing density profile in the remaining space. We see that at
ILD 10 Å, $g_{ij}(r)$ has two small peaks near r = 9 Å and r = 11 Å, but at ILD 8.49 Å
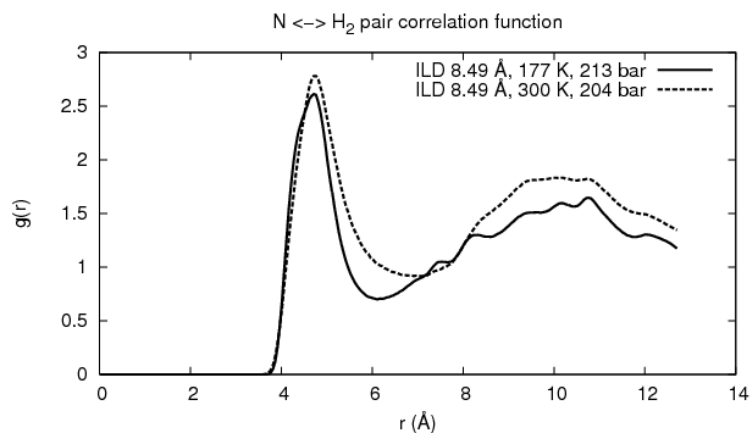
(a) At constant pressure and ILD
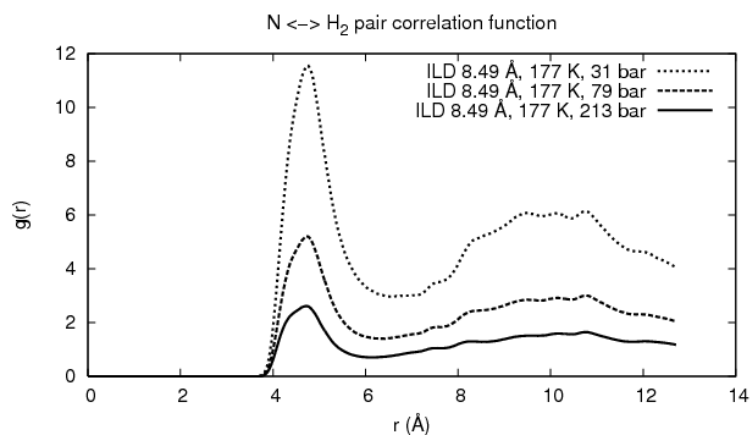
(b) At constant temperature and ILD
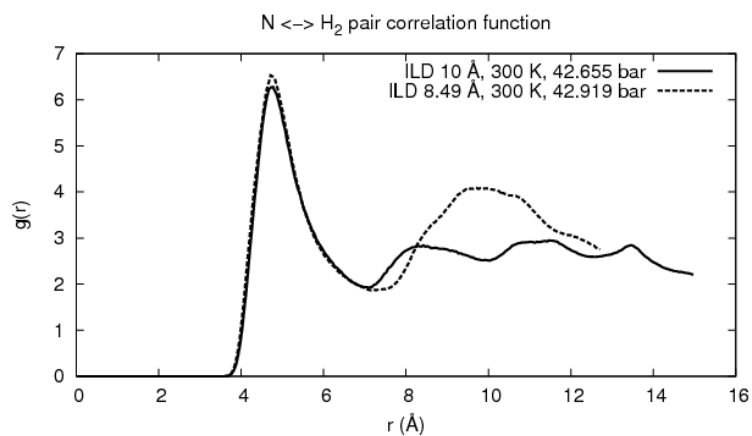
(c) At constant pressure and temperature

Fig. 19. Pair correlation functions between TMA-LiPc cation N and H_2
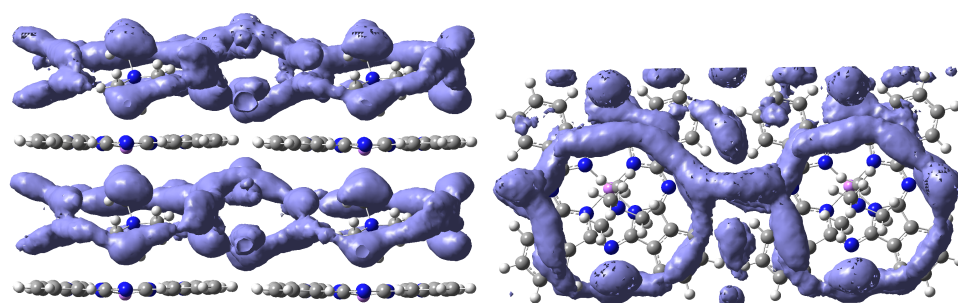
(a) 177 K
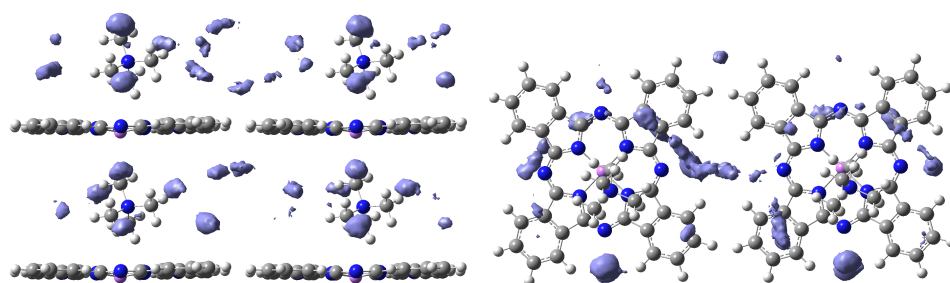
(b) 300 K

Fig. 20. TMA-LiPc H_2 probability surface at ILD 8.49 Å and constant pressure and varying temperature
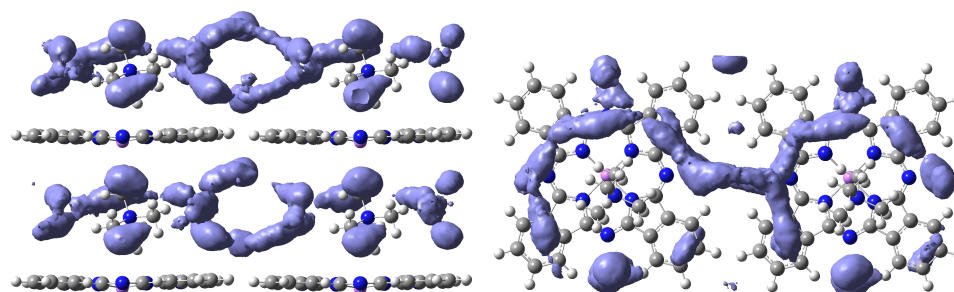
(a) 31 bar
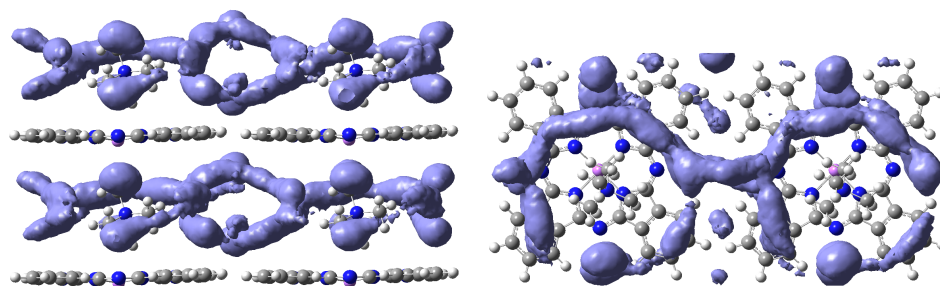
(b) 79 bar
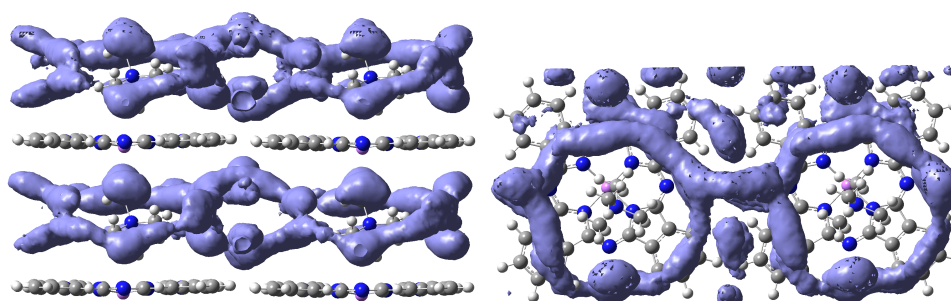
(c) 213 bar

Fig. 21. TMA-LiPc H_2 probability surface at ILD 8.49 Å and constant temperature and varying pressure
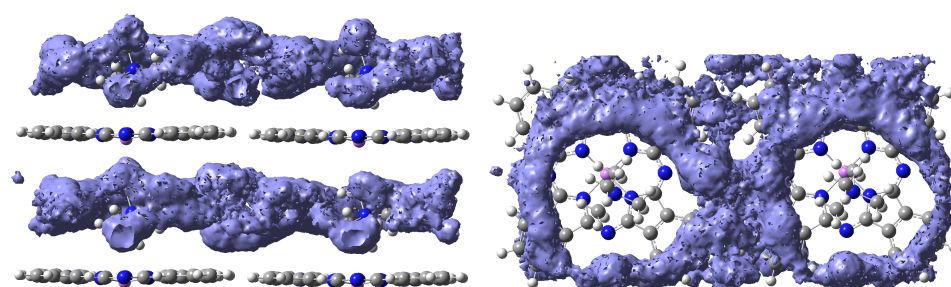
(a) ILD 8.49 Å
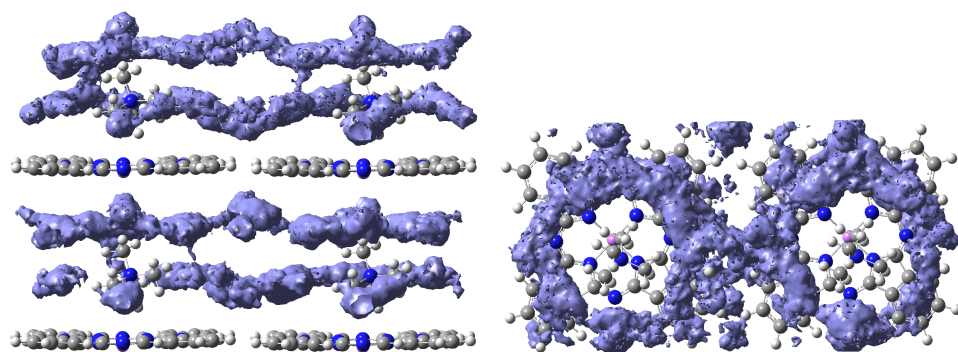
(b) ILD 10 Å

Fig. 22. TMA-LiPc H_2 probability surface at constant pressure and temperature and varying ILD

there is a larger single peak between r = 7 Å and r = 12 Å; these correspond directly to the different shapes of the high-density rings at the two ILD.

(a) ILD 8.49 Å   (b) ILD 10 Å   (c) Top view

Fig. 23. TMA-LiPc $g_{ij}(r)$ at $r \approx 5$Å compared to H_2 probability surface

(a) ILD 8.49 Å   (b) ILD 10 Å   (c) Top view
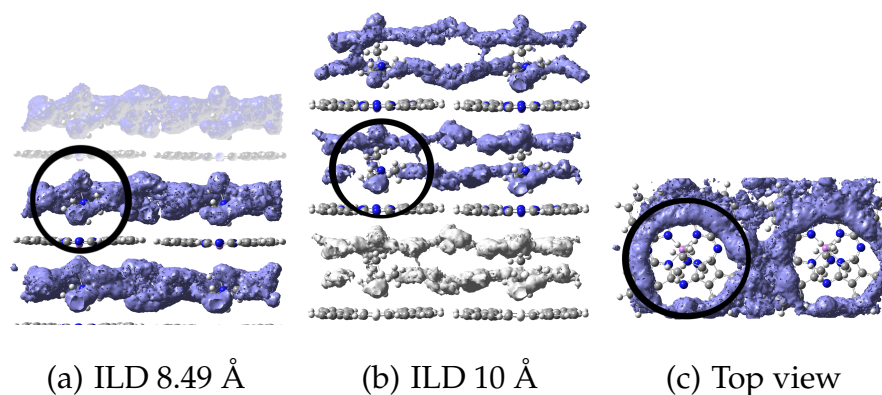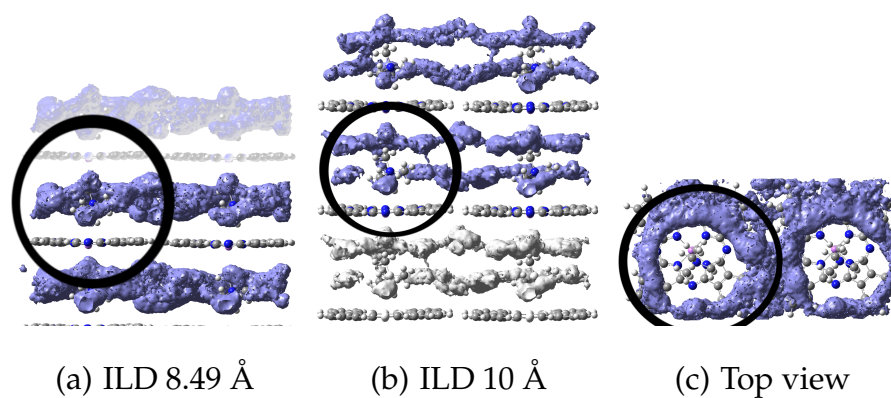
Fig. 24. TMA-LiPc $g_{ij}(r)$ at $r \approx 8$Å compared to H_2 probability surface

Figures 23, 24, and 25 show the top view and side views of the 5% H_2 probability surface at the two ILD with the radius around the cation N marked at approximately r = 5 Å, 8 Å, and 12 Å, respectively. The left column shows the side view at ILD 8.49 Å, the middle column shows the side view at ILD 10 Å, and the right column shows the top-down view. One can see that as the bounding sphere for $g_{ij}(r)$ grows

(a) ILD 8.49 Å   (b) ILD 10 Å   (c) Top view
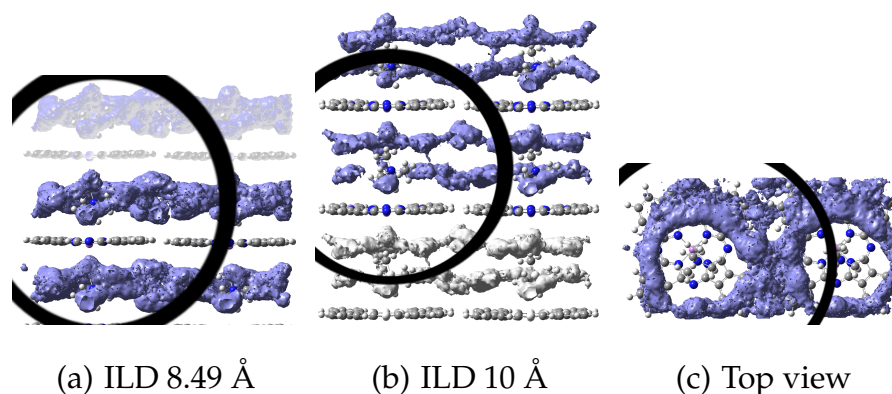
Fig. 25. TMA-LiPc $g_{ij}(r)$ at $r \approx 12$Å compared to H_2 probability surface

at ILD 8.49 Å, it first encounters a continuous region around the cation near r = 5 Å and then it encounters similar continuous regions in the inter-molecular layers both above and below. For ILD 10 Å the bounding sphere encounters the split density rings surrounding the cation, but the density is symmetric so a single peak appears in the $g_{ij}(r)$ graph near r = 5 Å. However, as the bounding sphere grows it encounters the split density rings surrounding the cation in the adjacent inter-molecular layers at different r values, which correspond to the two small peaks in the ILD 10 Å $g_{ij}(r)$ plot between r = 7 Å and r = 12 Å.

5. Z density profile

The H_2 high-density surfaces were very interesting, but still needed to be better validated quantitatively. The Z density profile provided a way to do this. The MD were oriented such that the Z axis was parallel to the phthalocyanine plane, i.e. the Z axis was directly vertical along the images of Figure 15. This allowed the Z density profile data (DL_POLY file ZDNDAT) to directly match the "top-down" view over the Pc plane as shown in Figure 9 A and in the H_2 density images.

Figure 26 shows the Z density profile for ILD 8.49 Å, 177 K, and 213 bar with the 25% H_2 probability surface graph overlaid at the same length scale. It is clear that they visibly correlate well: all of the spikes on the Z density line have corresponding high-density regions below them on the H_2 probability image. In particular, the edges of the circular region where the projection of density on the XY plane would be higher are in fact higher around r = 1, 10, 16, and 25 Å. The two spikes directly over the centers of the rings at r = 6 and 20 Å are supported by the large regions at the top and bottom of the rings; these are the regions at the intersections (6, 0.006), (6, 0.015), (20, 0.006), and (20, 0.015). However, the single very large spike between the two Pc does not seem to have a lot of corresponding high density.

The same data that generated the H_2 density images can easily be converted to a Z density profile. Plots of the Z density from the H_2 probability data in the `HISTORY` file against the real Z density from the `ZDNDAT` data are shown in Figure 27. Here the H_2 probability Z density has been rescaled as close as possible to match the scale of the `ZDNDAT` data. Though the peaks are not quite as sharp, they match up very well between the two data sets. The relative heights of the peaks within each data set are similar and are located at the correct Z distance. At lower temperatures the H_2 data matches even better, including the features at Z ~3.5 Å and Z ~17.5 Å.

The total density shows the spike at Z = 13.85 Å but the high-density surfaces do not. This implies that the local density at any particular point within the Z = 13.85 Å space is not significantly higher than the bulk density, yet the bulk density in total is still high.
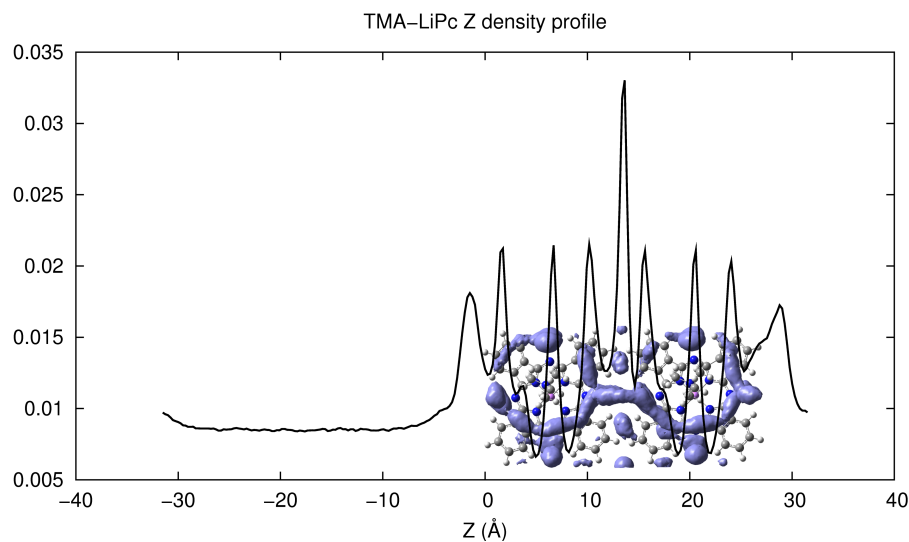
Fig. 26. TMA-LiPc Z density profile

6. Binding energy surfaces

Since the only potential allowed was van der Waals interactions, and since the solid was fixed in space, it seemed reasonable to expect that the H_2 density profile might be directly predictable by analysis of the binding energy field produced from the MD force field Lennard Jones parameters. The ChENL application `h_lj_density` was written to generate the binding energy force field from stock DREIDING parameters to test this. Note that these surfaces only show the binding energy from the Lennard-Jones interaction of H_2 and the sites on the macromolecule; the Lennard-Jones interactions of H_2 with H_2 are not computed, yet at high adsorption densities this H_2 -H_2 interaction will contribute positively to the total binding energy.

Figure 28 shows the 0.9 kcal/mol and 1.2 kcal/mol binding energy surfaces for TMA-LiPc at ILD 8.49 Å. Figure 29 shows the 0.9 kcal/mol and 1.2 kcal/mol binding
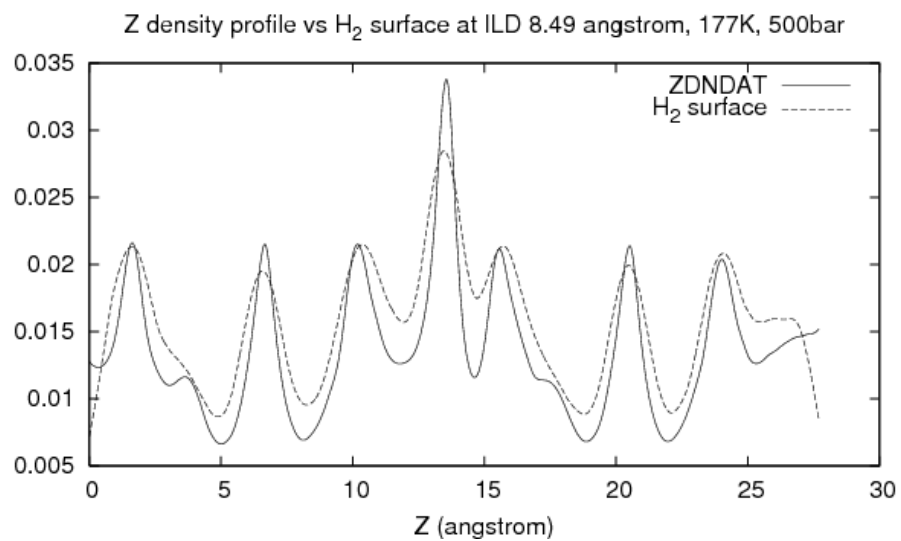
(a) 177 K
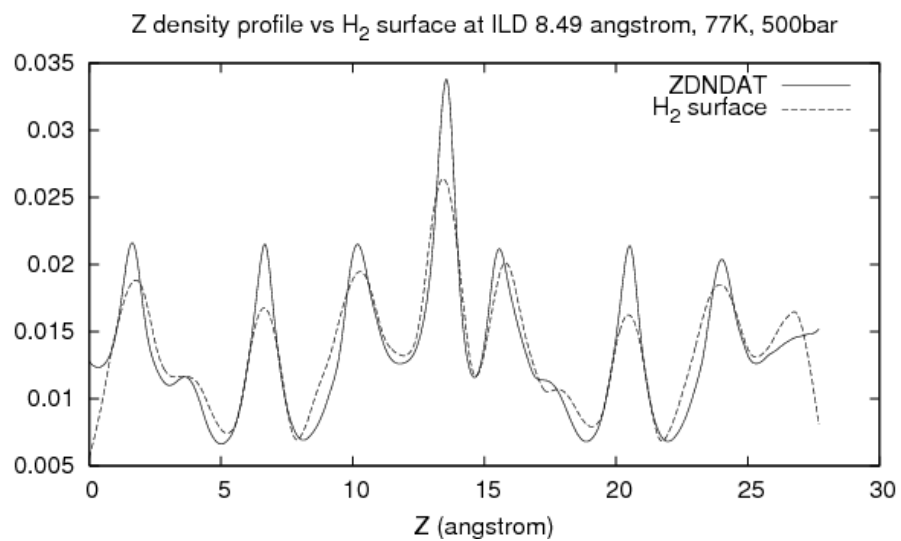
(b) 77 K

Fig. 27. TMA-LiPc Z density profile versus H_2 probability density

energy surfaces for TMA-LiPc at ILD 10 Å. These surfaces closely mirror the actual H_2 density profiles depicted in Figures 20 through 22, including the splitting of the high density region from ILD 8.49 Å to ILD 10 Å. These figures appear to directly correlate quite well to the high-density region in the H_2 probability surfaces. As in the H_2 density graphs, the 0.9 kcal/mol binding region splits between ILD 8.49 Å and ILD 10 Å. Looking down at the 0.9 kcal/mol images, one sees protrusions along the centers of the rings around the cation above the void spaces between the outer phenyl groups on the Pc; these regions directly correspond to the high-density regions on the H_2 graph under the spikes of the Z density profile at r = 6 and 20 Å. However, the binding energy does not correlate to the Z density profile as shown in Figure 30.

In general, this means that the high-density portions of the H_2 probability surfaces can be predicted and do visibly correlate with the actual structure of the adsorbed H_2 , but they do not by themselves directly predict the total adsorption. One possible reason for this is that the binding energy drives the adsorption only near the atoms of the macromolecule; in the larger void spaces of the crystal the binding energy is negligible. The void volume thus must somehow be taken into account before the total adsorption could be predicted.
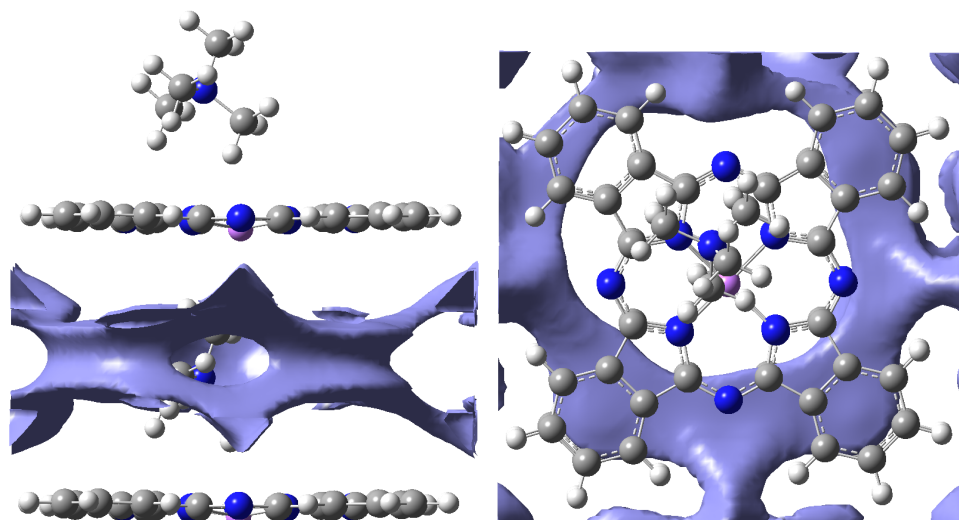
(a) 0.9 kcal/mol
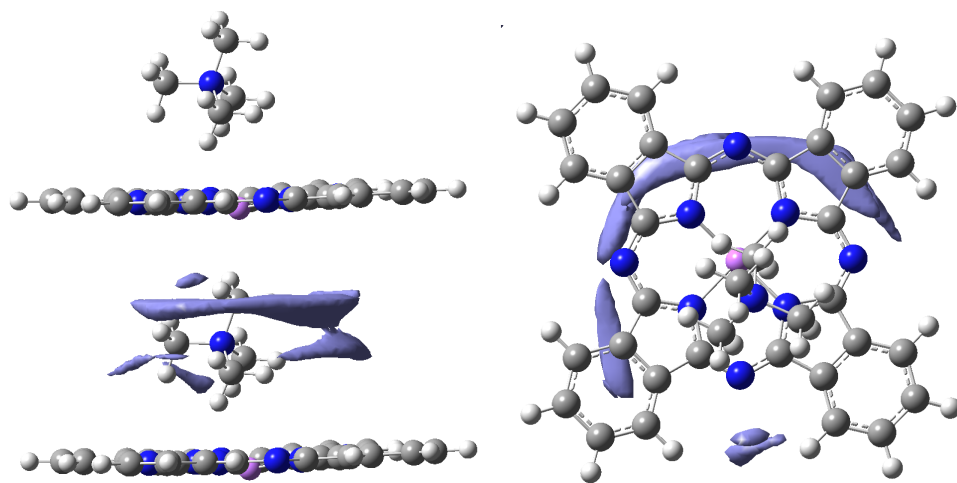
(b) 1.2 kcal/mol

Fig. 28. TMA-LiPc H_2 Lennard-Jones binding energy surfaces at ILD 8.49 Å
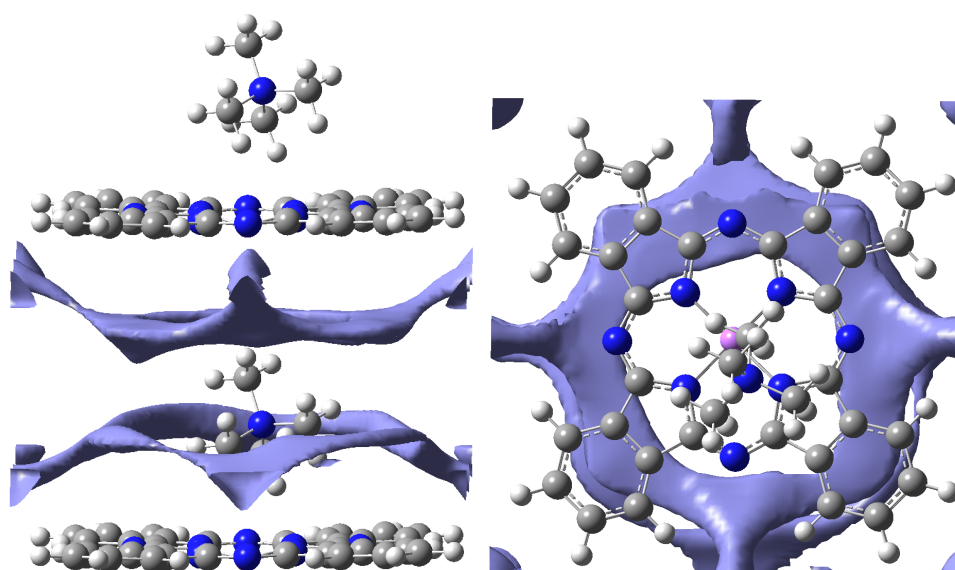
(a) 0.9 kcal/mol
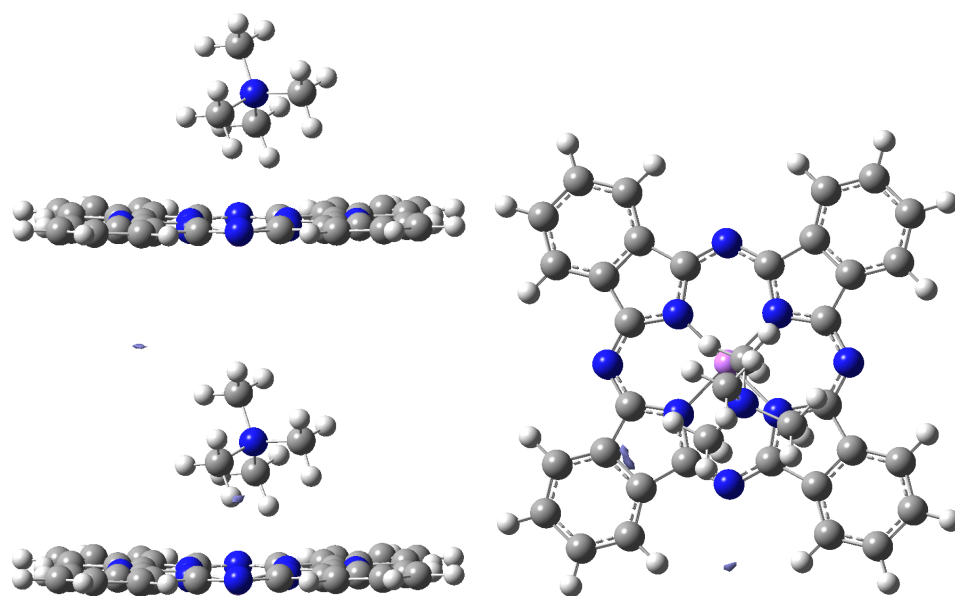
(b) 1.2 kcal/mol

Fig. 29. TMA-LiPc H$_2$ Lennard-Jones binding energy surfaces at ILD 10 Å
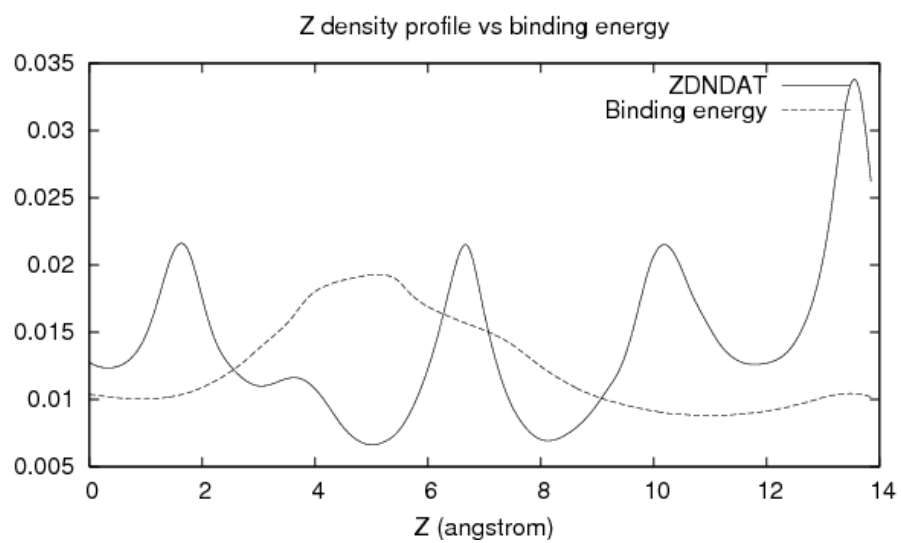
Fig. 30. TMA-LiPc Z density profile versus binding energy density

CHAPTER III

H$_2$ ADSORPTION IN TRIMETHYL-(2-TRIMETHYL AZANIUMYLETHYL) AZANIUM PHTHALOCYANINE (TMA2-PC)

A. Optimized geometry

B3LYP DFT with a basis set of 6-31g(d,p) was used to optimize the geometry of a single molecule; the resulting geometry in shown in Figure 31. The computed dipole moment was 24.72 Debye and the volumetric polarizability was 673.85 Bohr^3 = 9.985×10^{-23} cm^3. The Mulliken charge distribution is shown in Figure 32. The charges range from -0.608 to +0.450; the maximum values are in the inner ring carbon and nitrogen atoms on the phthalocyanine (Pc). The separation between the TMA2 cation (+2) and the Pc anion (-2) causes the Pc π system to deform and deflect significantly out of plane away from the TMA2 cation.

(a) Top   (b) Side
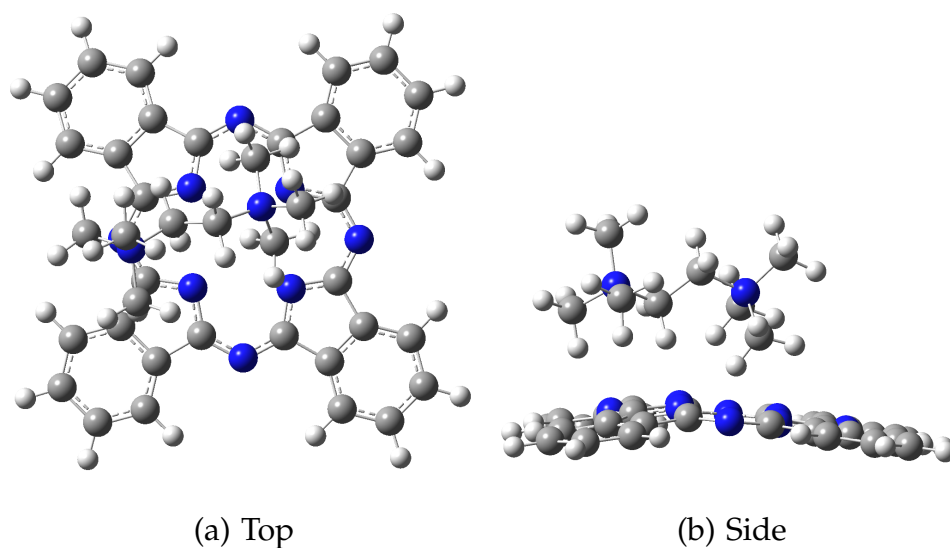
Fig. 31. TMA2-Pc optimized geometry
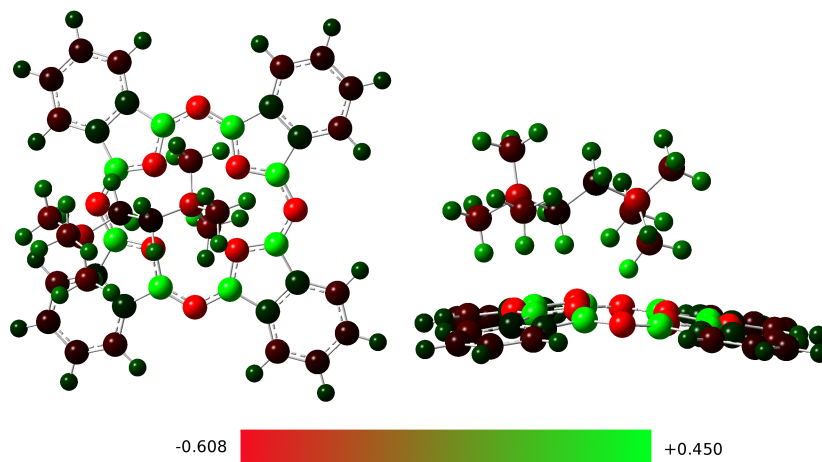
Fig. 32. TMA2-Pc charge distribution

B.   Crystal structure

This system is not yet known to have been synthesized, and similar systems were not found in the Cambridge Structural Database [27].

DFT with the B3LYP/6-31g(d,p) basis set was used to optimize a dimer system. The initial distance between molecules was 8.07 Å. During optimization the two TMA2-Pc units separated slightly, translated horizontally, and the two Pc tilted to form an angle of about 36 degrees. The final distance between the TMA2 cations was 8.3 Å and the top molecule was horizontally offset by about 3.5 Å. The average total distance between corresponding atoms was 8.38 Å, and the average vertical distance (corresponding to the ILD) was 8.12 Å. Figure 33 shows the side view of initial and final configurations where one can see the horizontal translation of the top molecule. Figure 34 depicts the initial and final configurations looking down the cation axis to show the tilted angle of the Pc.

MD systems (using the TMA2-Pc Li ion force field described in Chapter IV)

(a) Beginning structure

(b) Ending structure
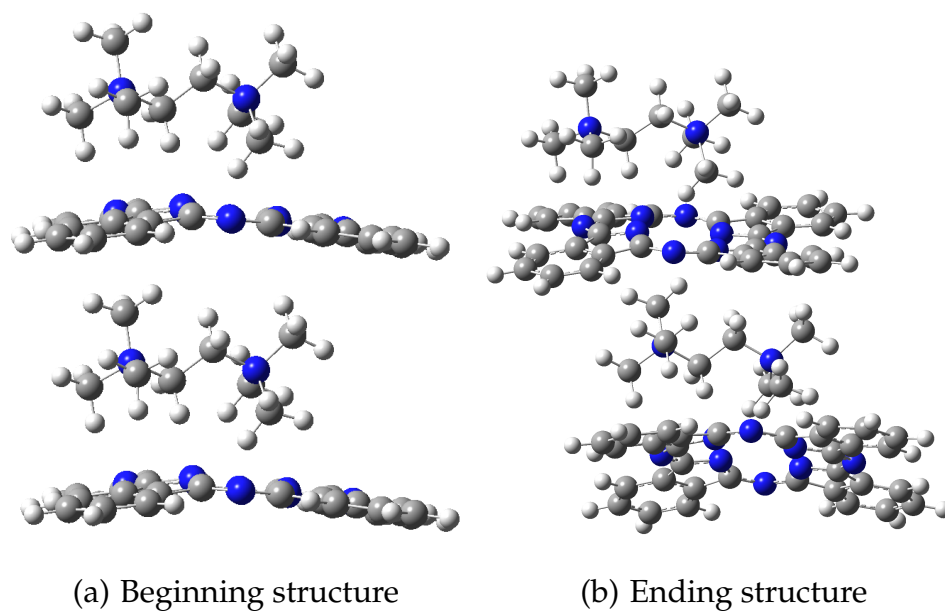
Fig. 33. TMA2-Pc optimized dimer - first angle

(a) Beginning structure

(b) Ending structure
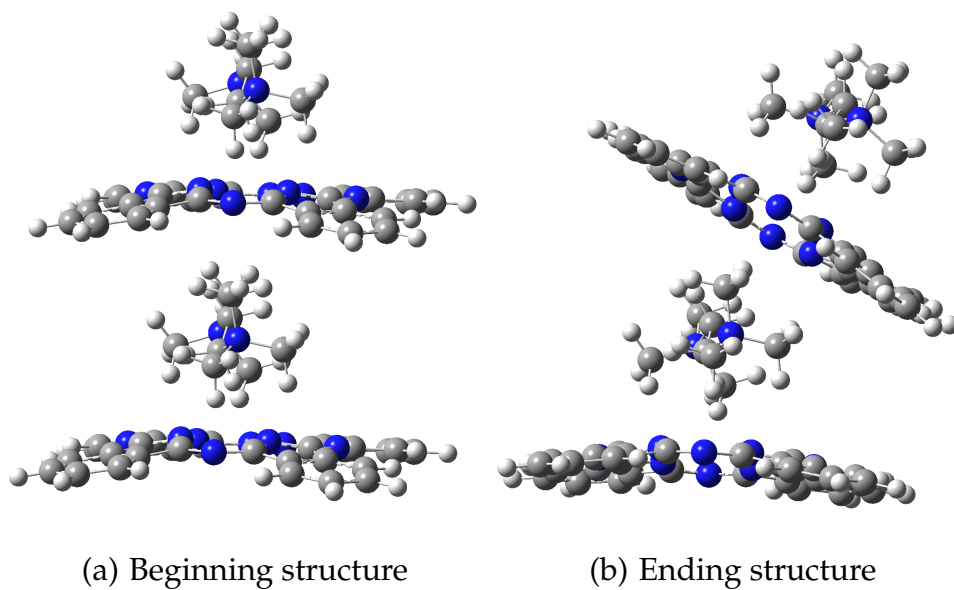
Fig. 34. TMA2-Pc optimized dimer - second angle

were run at various temperatures to estimate the true crystal structure. One representative resulting crystal structure is shown in Figure 35. The MD structure started as a stacked paralleliped system with inter-layer distance 8.12 Å; the final structure remains stacked but the crystal units are staggered such that the Pc project into the space near the adjacent unit's cation. The resulting structure resembles the starting structure but uses less overall volume, as shown by the void volume in Figure 35.
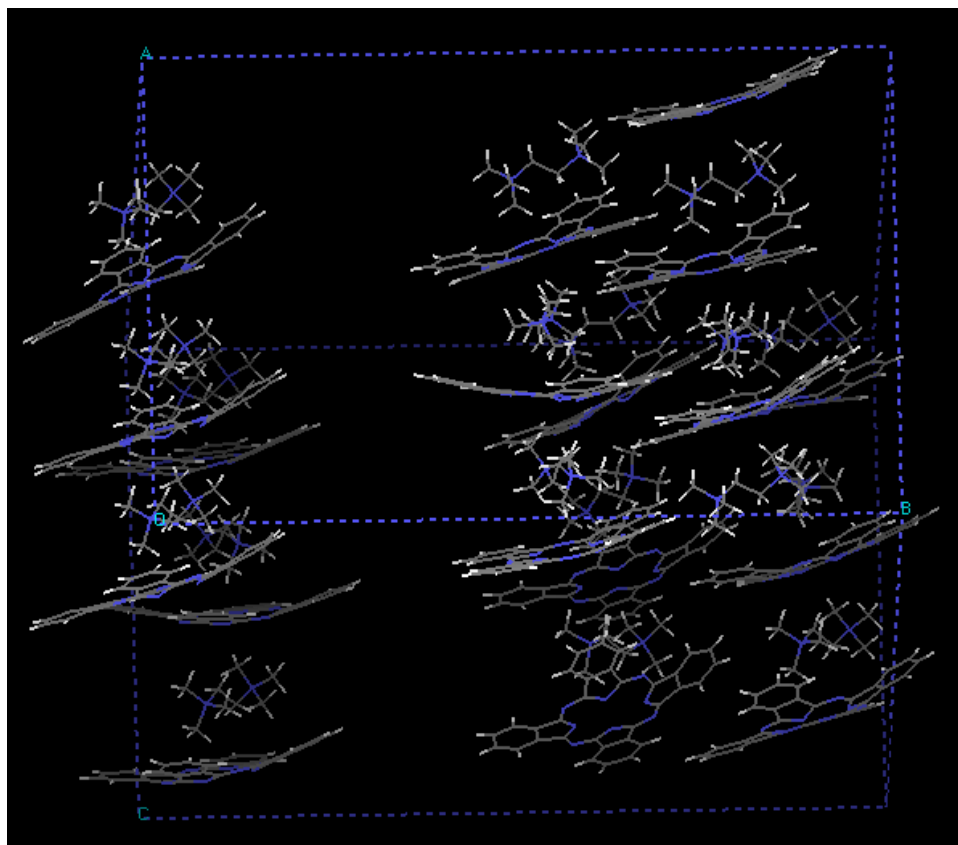
Fig. 35. TMA2-Pc crystal structure

C.   MD force field

Like the TMA-LiPc system of Chapter II, the TMA2-Pc system was modeled as a system of fixed solid crystal atoms with H_2 molecules allowed to move. It was noted during the work in weighting the induced dipole term for TMA-LiPc that some sites on the macromolecule had a net repulsive force on the H_2, e.g. they contributed against the permanent dipole attraction between the H_2 and the macromolecule. A new method was developed to try to apportion the induced dipole term in such a way that this effect would be supported, i.e. that those "repulsive" sites would have a shallower energy well in the van der Waals interaction potential. Also, it was hoped the new model would better reflect the highly asymmetric geometry of TMA2-Pc compared to TMA-LiPc. The new model depended only on the computed binding energy ΔE_i from many systems and could be easily automated. It is important to stress that this was *not* a rigorous calculation, but rather simply a method to apportion the induced dipole attraction. The model was as follows:

1. *M* systems, each containing one TMA2-Pc and one H_2 molecule, were gener-
   ated with the H_2 located with its bond along a path radiating from the mass-
   weighted center of TMA2-Pc. The H_2 was spaced at 1 Å intervals inclusive
   between 2 and 18 Å from the center and every 45 degrees from the azimuth and
   zenith, i.e. for a spherical coordinate denoted (ρ, θ, ϕ): $\rho = \{2, 3, 4, ..., 18\}$, $\theta =$
   $\{0, 45, 90, 135, 180, 225, 270, 315\}$ degrees, $\phi = \{0, 45, 90, 135, 180\}$ degrees. Any
   systems that would have placed either atom of the H_2 within 1.5 Å of any
   other atom were discarded to avoid high-energy systems from skewing the
   results. A total of 366 such systems were created.

2. ΔE_i was computed for each system as the difference between the infinite-

separation energy of the system and H_2 and the energy for the ith system, i.e. ΔE_i was the binding energy.

3. ΔE_i was expanded as a weighted sum of Coulombic interaction energies between each of the two atoms of the H_2 molecule and each site on the macromolecule:

$$\Delta E_i = c_1 U_1 + c_2 U_2 + \cdots + c_n U_n$$

$$U_j = \frac{q_{site} q_1}{r_1} + \frac{q_{site} q_2}{r_2}$$

q_{site} is the charge on the TMA2-Pc atom; q_1 is the charge on the first H_2 atom located r_1 from the TMA2-Pc site; likewise for q_2 and r_2. U_j is the total Coulombic interaction between the H_2 molecule and the site on the macromolecule. The atomic charges were taken from the electrostatic potential function (G03 keyword `pop=(chelpg, dipole)`).

4. The binding energy ΔE_i depended on both location and orientation of H_2 around the macromolecule. Since the binding energies of many such orientations were computed, the c_j coefficients could be fitted via linear regression. In matrix form:

$$\underbrace{\begin{pmatrix} \Delta E_1 \\ \vdots \\ \Delta E_m \end{pmatrix}}_{\mathbf{Y}} = \underbrace{\begin{pmatrix} U_1 & \cdots & U_n \\ \vdots & \ddots & \vdots \\ U_1 & \cdots & U_n \end{pmatrix}}_{\mathbf{\Phi}} \underbrace{\begin{pmatrix} c_1 \\ \vdots \\ c_n \end{pmatrix}}_{\mathbf{\Theta}}$$

The least-squares fit solution for the c_j terms is given by [34] and is

$$\mathbf{\Theta} = \left(\mathbf{\Phi}^{\mathsf{T}} \mathbf{\Phi} \right)^{-1} \mathbf{\Phi}^{\mathsf{T}} \mathbf{Y}$$

5. The c_j coefficients were normalized via:

$$w_i = \frac{c_j}{\sum\limits_{i=1}^{n} c_i}$$

leading to the final weighting factors w_j.

6. The Lennard-Jones potential parameters were then refitted as for TMA-LiPc to include the weighted dipole term:

$$
\begin{aligned}
E_{vdw,i} &= 4\epsilon_{ij}\left(\left(\frac{\sigma_{ij}}{r_{vdw}}\right)^{12} - \left(\frac{\sigma_{ij}}{r_{vdw}}\right)^{6}\right) + w_i\Gamma_{ij} \\
&= 4\epsilon_{ij}\left(\left(\frac{\sigma_{ij}}{r_{vdw}}\right)^{12} - \left(\frac{\sigma_{ij}}{r_{vdw}}\right)^{6}\right) - w_i\frac{1}{4\pi\epsilon_0}\frac{\mu_{molecule}\alpha'_{H_2} + \mu_{H_2}\alpha'_{molecule}}{r_\Gamma^6} \\
&\approx 4\epsilon'_{ij}\left(\left(\frac{\sigma'_{ij}}{r_{vdw}}\right)^{12} - \left(\frac{\sigma'_{ij}}{r_{vdw}}\right)^{6}\right)
\end{aligned}
$$

Here ϵ_{ij} and σ_{ij} are the original Lennard-Jones parameters derived from the Lorentz-Berthelot mixing rules; ϵ'_{ij} and σ'_{ij} are the values that were used in the MD simulations. The Lennard-Jones contribution was computed along the path between the H_2 bond center and the atom site on the macromolecule; however, the induced dipole contribution was computed along the path between the H_2 bond center and the molecule center. This is shown in Figure 36: r_{vdw} was measured from the site center to the H_2; r_Γ was measured from the mass-weighted center of the macromolecule to the H_2.

The pure species ϵ_i and σ_i values for C, N, H, and O were taken from DREIDING [32] and H_2 from Diep and Johnson [35]. H_2 parameters were fitted from Diep and Johnson Table I from $r = 3$ to 10 Å. All pure species values are shown in Table III.
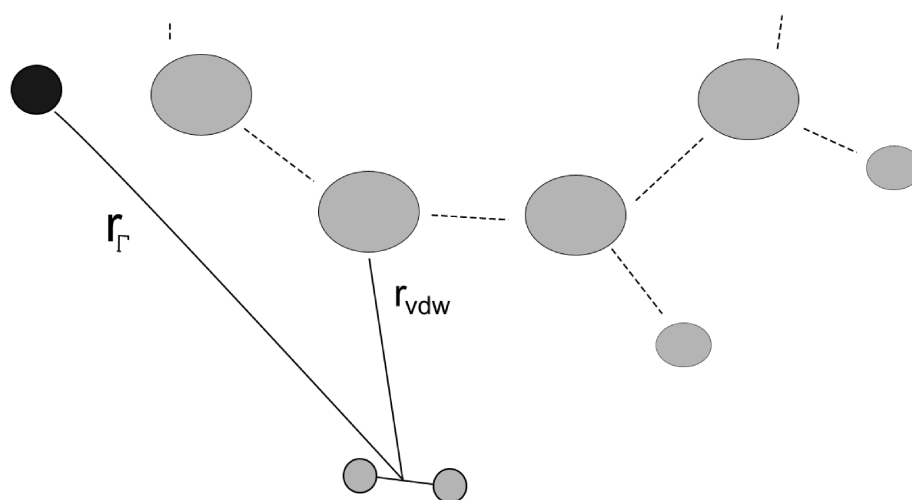
Fig. 36. TMA2-Pc depiction of r_Γ and r_{vdw}

Table III. TMA2-Pc Lennard Jones pure species parameters for H_2 adsorption

Atom	ϵ_i kcal/mol	σ_i Å
H	0.0152	2.8464
C	0.0951	3.4730
N	0.0774	3.2626
O	0.0957	3.0332
H_2	0.0652	3.0659

D. MD procedure

For the MD crystal structure, an orthorhombic paralleliped system was chosen with unit cell vectors a = $\langle 8.12, 0.0, -3.5 \rangle$ Å, b = $\langle 0.0, 13.85, 0.0 \rangle$ Å, and c = $\langle 0.0, 0.0, 13.85 \rangle$ Å. 8.12 Å was the inter-layer distance and 13.85 Å was the inter-molecule distance in accordance with earlier studies involving phthalocyanine [33]. Molecules were arranged in a $3 \times 3 \times 3$ structure as depicted in Figure 37. An additional gas-phase volume containing 770 H_2 molecules arranged in a uniform grid was appended to each system with the gas-phase volume chosen such to match the desired initial pressure. The pressure in the gas-phase region was approximated by the ideal gas law. A paralleliped periodic boundary condition was used. The TMA2-Pc molecules were frozen and only Lennard-Jones interactions were allowed between them and the H_2 molecules and between pairs of H_2 molecules. Each simulation ran for a total of 800 ps, with the first 300 ps used to reach equilibrium. System configurations were recorded every 2 ps for the remaining 500 ps, for a total of 251 recorded system configurations. For each system configuration, the percent weight uptake of H_2 in the crystal was calculated and the number of H_2 molecules in the gas phase were counted to determine the gas-phase pressure. The weight uptake is the ratio of mass of H_2 adsorbed over mass of crystal plus mass of H_2 adsorbed.

Only H_2 molecules within 4 Å of a crystal atom were assumed to be adsorbed. This was different than for TMA-LiPc and was due to the paralleliped geometry: atoms within the void space near the cation but not within 4 Å of a crystal atom would have been counted as adsorbed for TMA-LiPc but not for TMA2-Pc.
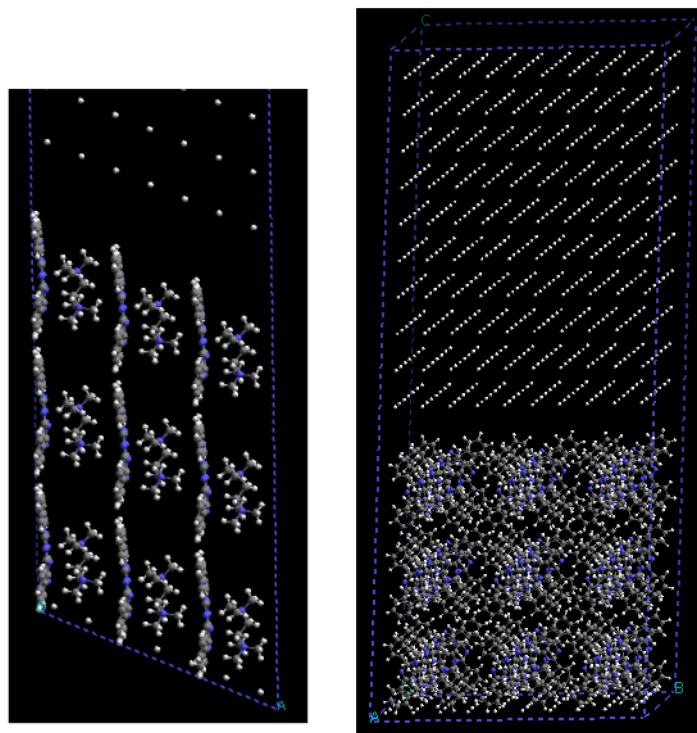
(a) Start
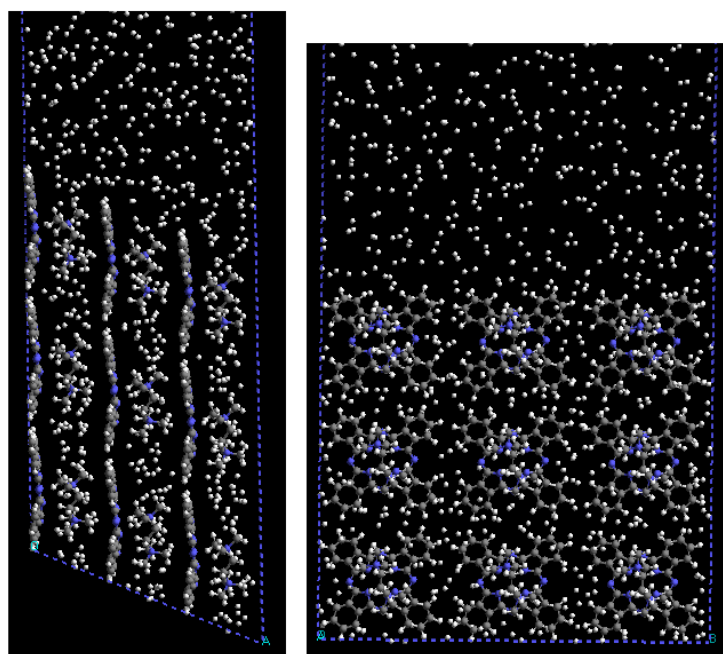
(b) End

Fig. 37. TMA2-Pc start and end configurations

E.   Results and discussion

1.   H$_2$ adsorption

The H$_2$ adsorption isotherms are shown in Figure 38. The raw data is reported in Appendix A Table X.

The maximum possible adsorption is about 7% at ILD 8.12 Å and 6% at ILD 10 Å at T = 77 K. Like TMA-LiPc, the adsorption is directly proportional to pressure and inversely to temperature. Also the adsorption is about 0.5% (wt/wt) higher at ILD 10 Å than at ILD 8.12 Å for all pressures and temperatures. This system can meet neither the minimum DOE target of 6% nor the ultimate target of 12%.

2.   H$_2$ self-diffusion coefficient

The H$_2$ self-diffusion coefficient was calculated and is shown in Figure 39 as a function of pressure and temperature and ILD. The raw data is reported in Appendix A Table XI. The H$_2$ self-diffusion coefficient appears to follow the same trend as for TMA-LiPc: increasing with temperature and decreasing with pressure. Also like TMA-LiPc, the trend does not directly correlate to ILD: it is slightly lower at ILD 10 Å and low temperature, but at higher temperatures it seems to be essentially identical at both ILD 10 Å and ILD 8.12 Å.

3.   Pair correlation functions

Figure 40 shows several $g_{ij}(r)$ pair correlation functions between the most central nitrogen atom in the TMA2 cation (the one directly over the inner ring of the Pc) and the H$_2$ gas. Figure 40 A shows $g_{ij}(r)$ at similar pressure and ILD but varying in temperature. The two graphs show a peak at about 5 Å with the higher peak at the lower temperature of 77 K. This seems a contradictory result since the total
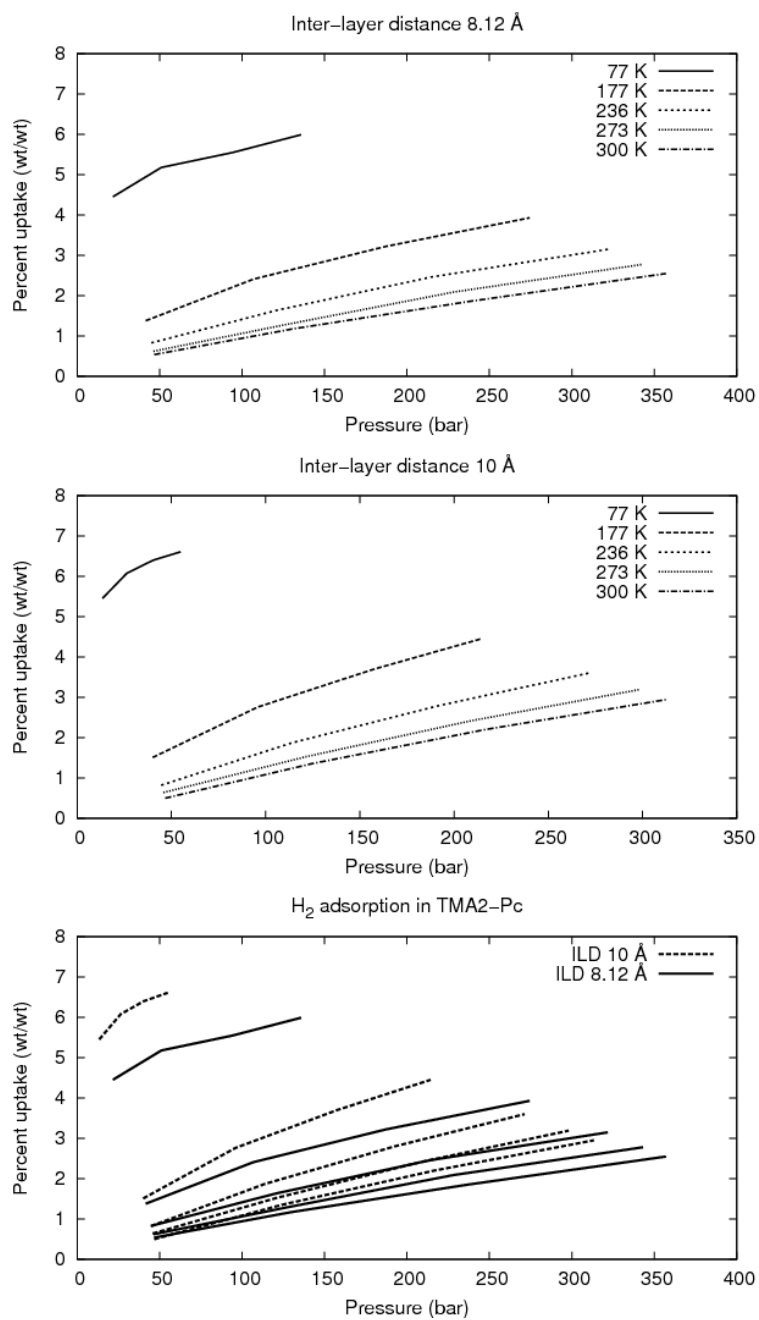
Fig. 38. TMA2-Pc adsorption isotherms
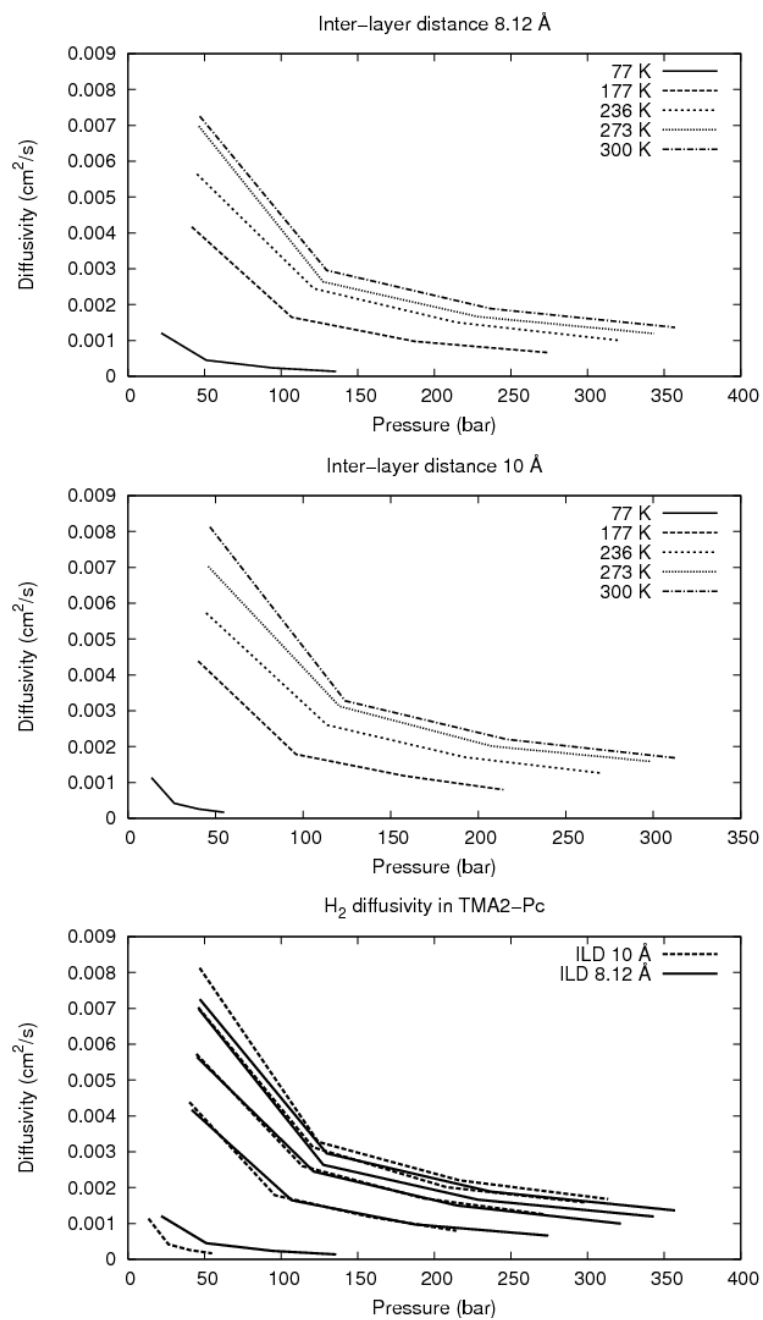
Fig. 39. TMA2-Pc H$_2$ self-diffusion coefficient

adsorption is indeed higher at 77 K. One possible explanation is that the bulk and local densities are of such different magnitudes that the pair correlation functions between these two systems cannot be directly compared. The 10% H_2 density surface shown in Figure 41 seems to support this idea: at lower temperature the adsorption is dramatically higher, and at high temperature there is practically no adsorption at all. Figure 40 B shows $g_{ij}(r)$ at the same temperature and ILD but at different pressures. The trend is clearly higher adsorption at higher pressure, consistent with the isotherms. Figure 40 C shows $g_{ij}(r)$ at similar temperature and pressure but different ILD. The trend is higher adsorption at higher ILD, also supported by the isotherms.

4. H_2 adsorption region

Figure 41 through Figure 43 show the H_2 probability surfaces corresponding to Figure 40. Figure 41 shows the 10% H_2 probability surface corresponding to Figure 40 A. Figure 42 shows the 10% H_2 probability surface corresponding to Figure 40 B. Figure 43 shows the 5% H_2 probability surface corresponding to Figure 40 C. Because of the paralleliped crystal structure, the top views are not oriented looking directly down on the XZ plane but rather are oriented to align similar atoms so that the regular structure can be better seen. The trends all follow the isotherms: greater adsorption with higher pressure and ILD, and lower adsorption with higher temperature. Like TMA-LiPc, at ILD 10 Å the high density region splits into two regions around the cation as shown in Figure 43. However, the regions are not as cohesive as for TMA-LiPc.
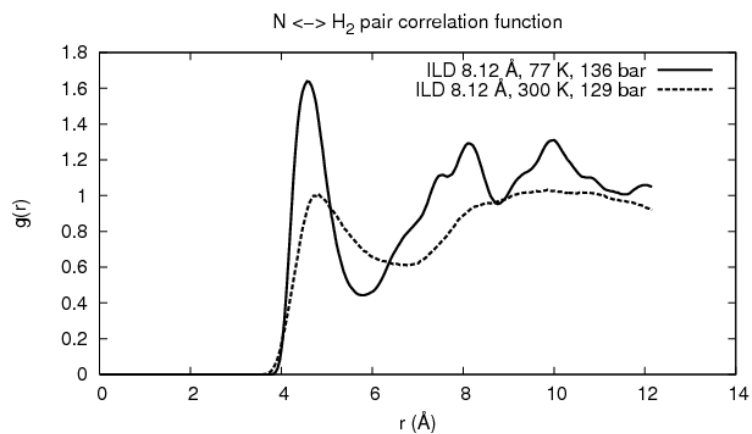
(a) At constant pressure and ILD
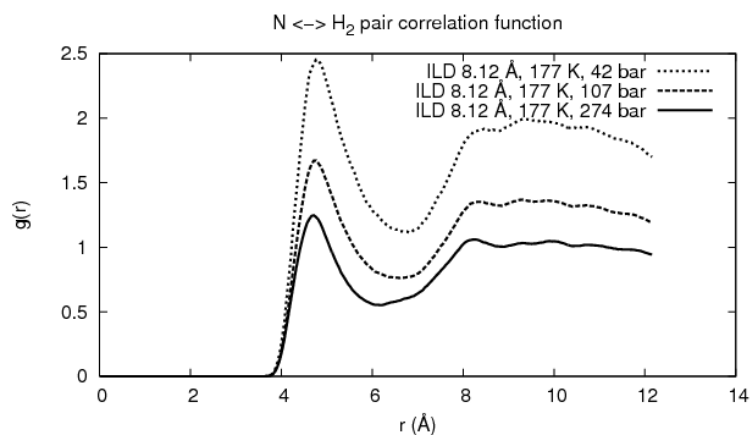
(b) At constant temperature and ILD
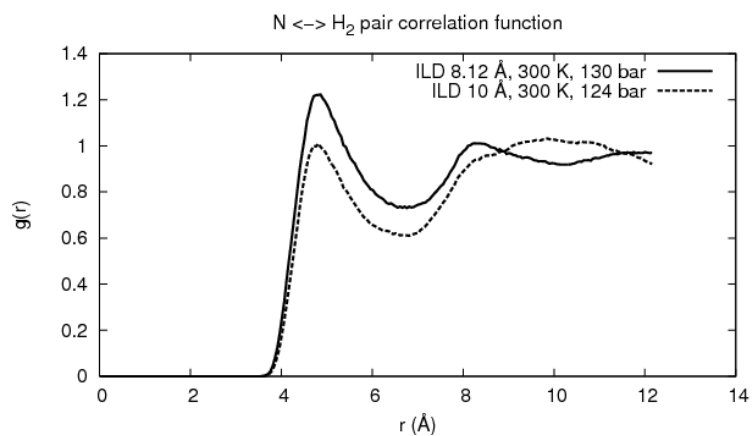
(c) At constant pressure and temperature

Fig. 40. Pair correlation functions between TMA2-Pc cation N and H_2
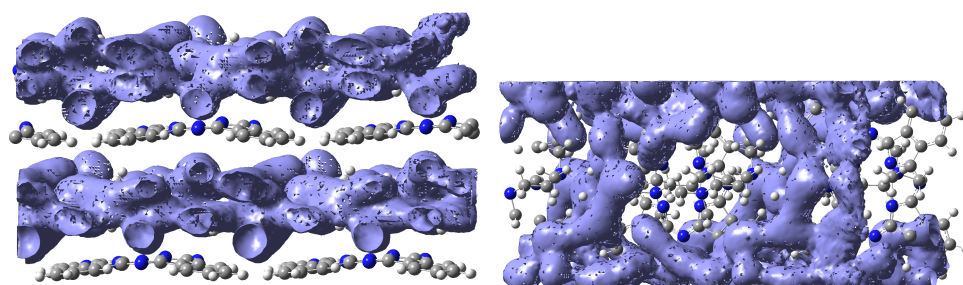
(a) 77 K
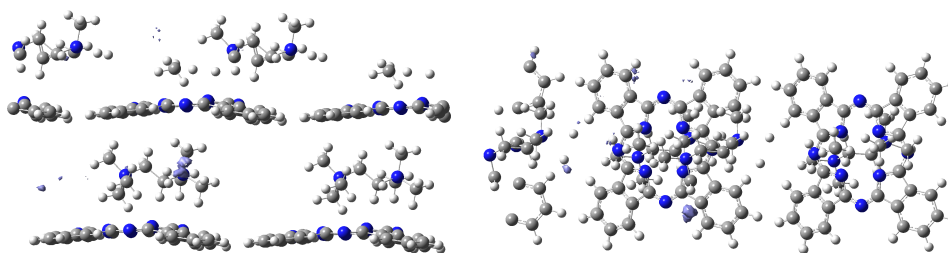
(b) 300 K

Fig. 41. TMA2-Pc H_2 probability surface at ILD 8.12 Å and constant pressure and varying temperature
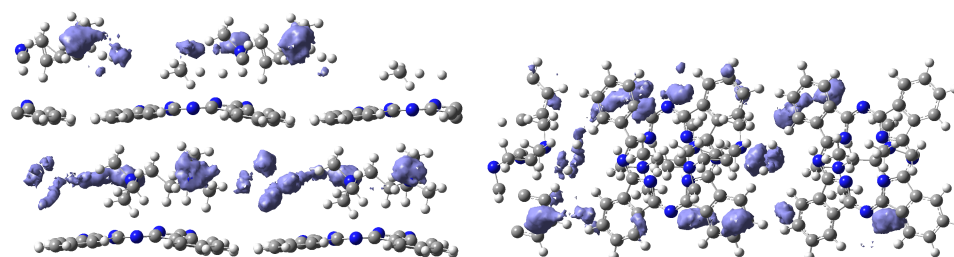
(a) 31 bar
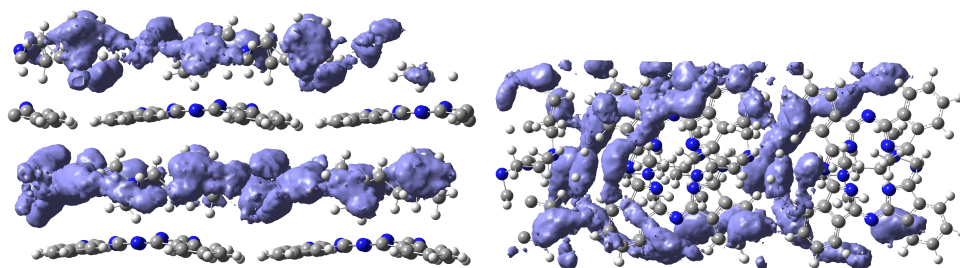
(b) 79 bar
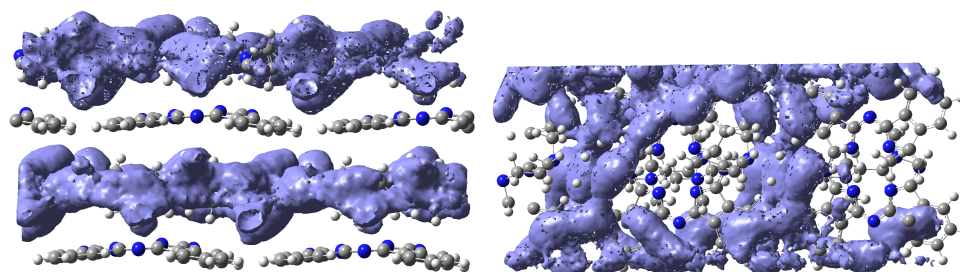
(c) 213 bar

Fig. 42. TMA2-Pc H_2 probability surface at ILD 8.12 Å and constant temperature and varying pressure
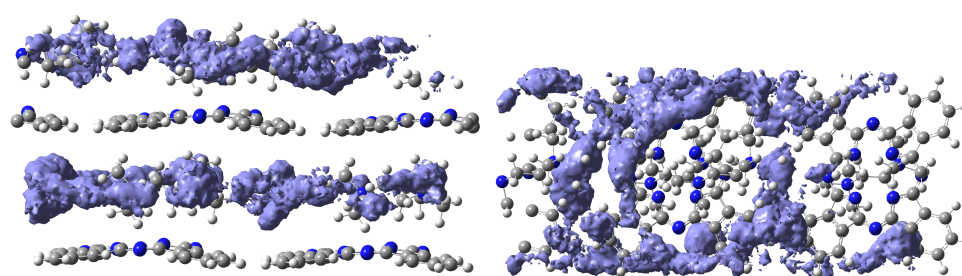
(a) ILD 8.12 Å
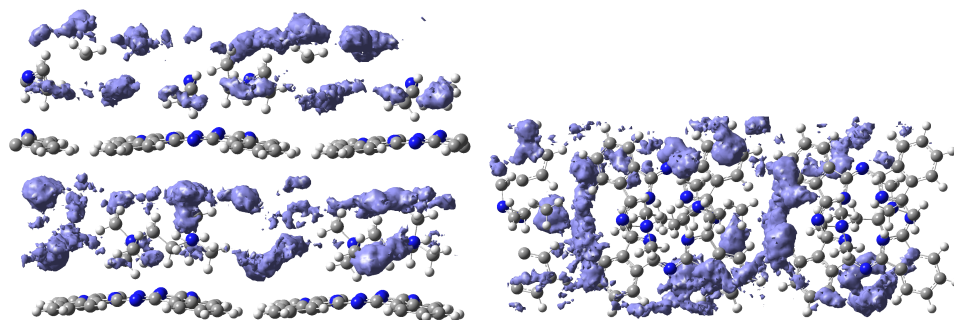
(b) ILD 10 Å

Fig. 43. TMA2-Pc H$_2$ probability surface at constant pressure and temperature and varying ILD

5. Binding energy surfaces

Figures 44 and 45 show the 0.9 kcal/mol and 1.2 kcal/mol binding energy surfaces for TMA2-Pc at ILD 8.12 Å and ILD 10 Å, respectively. Due to a limitation in GaussView, the surfaces are rendered within a cubic region rather than a paralleliped region. These surfaces approximately match the H_2 density: the high-binding energy region is near the cation. However, due to the paralleliped crystal structure the binding surface is distorted around the cation. The top edge of the high binding energy region near the Pc above is horizontally translated by about 3 Å due to the Pc being translated by that amount. This is most visible in the ILD 10 Å 0.9 kcal/mol view in Figure 45 A. This results in the multiple rings visible top-down on the H_2 density graphs of Figures 41, 42, and 43. In general the binding energy surfaces visibly match the H_2 density surfaces, but the latter show more noise in the images.

6. Z density profile

Figure 46 shows the Z density profile for ILD 8.12 Å, 177 K, and 274 bar. Like TMA-LiPc, there are numerous spikes across the crystal structure—the region between Z = 0 Å and Z = 40 Å. However, unlike TMA-LiPc these spikes cannot be directly correlated to the H_2 probability density because of the paralleliped crystal structure: the XY plane cutting through the crystal intersects different layers of the crystal at different points along the TMA2-Pc crystal unit. This limits the analysis to comparison of the gas-phase region versus the adsorbed crystal region. In this case the gas-phase density—the region between Z = -30 Å to Z = -10 Å—is higher than within the crystal. This is different than for TMA-LiPc, and supports the isotherm data that shows TMA-LiPc adsorption is significantly higher than TMA2-
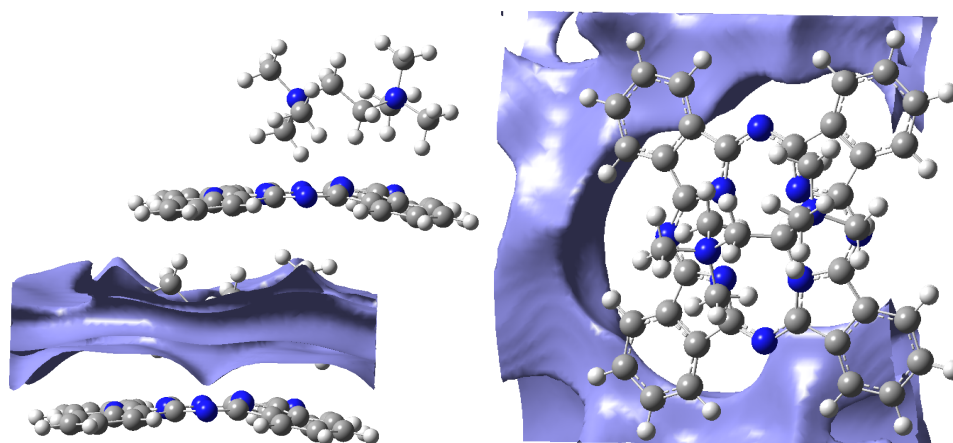
(a) 0.9 kcal/mol
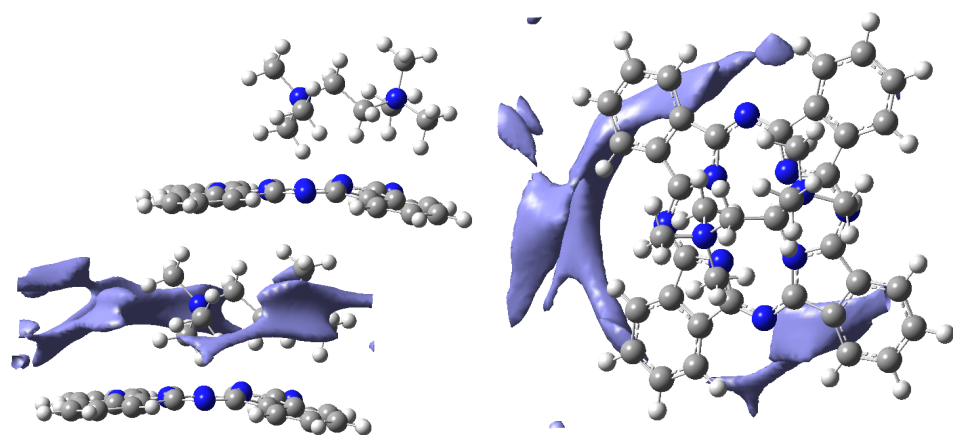
(b) 1.2 kcal/mol

Fig. 44. TMA2-Pc H_2 Lennard-Jones binding energy surfaces at ILD 8.12 Å
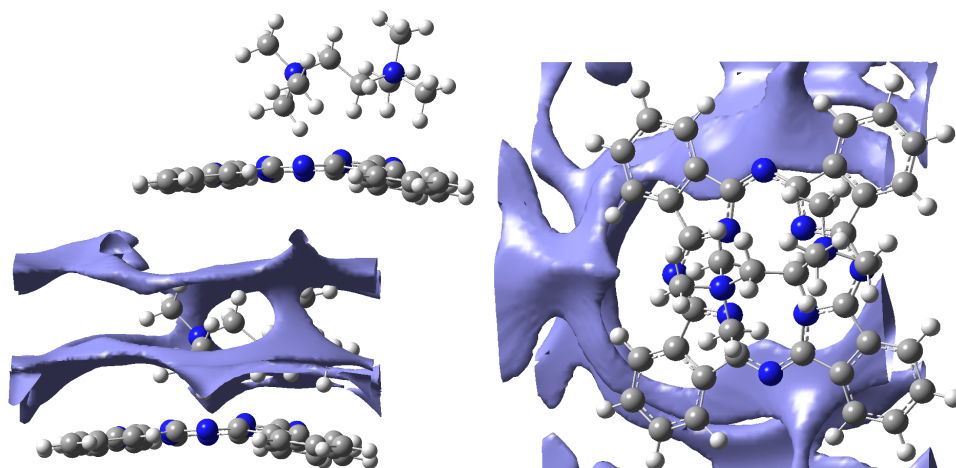
(a) 0.9 kcal/mol
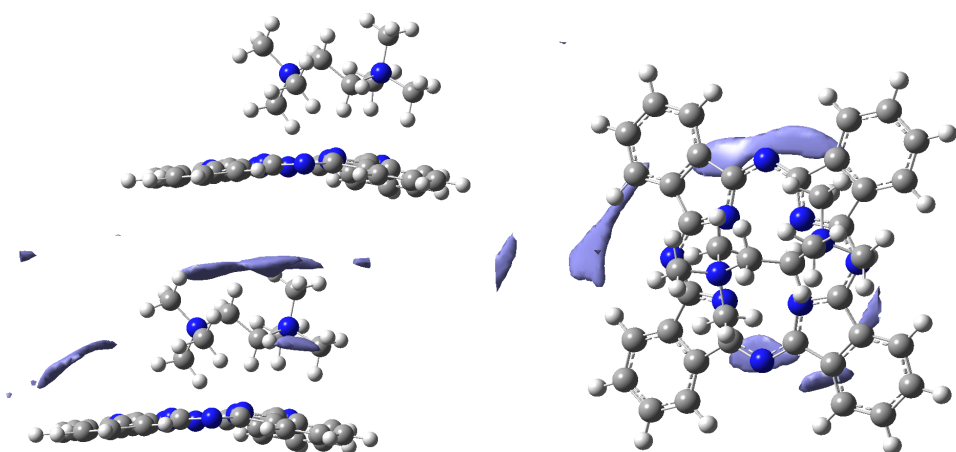
(b) 1.2 kcal/mol

Fig. 45. TMA2-Pc H_2 Lennard-Jones binding energy surfaces at ILD 10 Å

Pc adsorption at similar temperature and pressure.
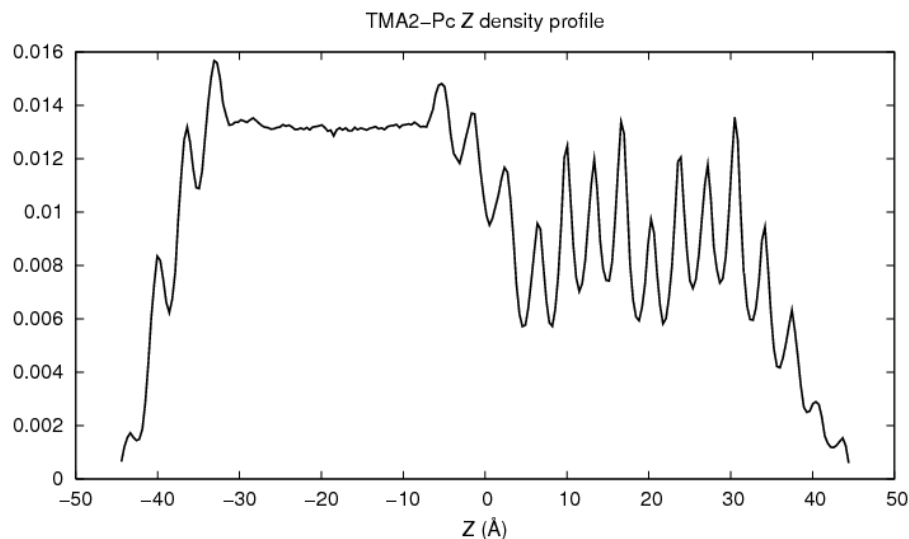
Fig. 46. TMA2-Pc Z density profile

F.   Crystal structure and H_2

Aga et al. [36] performed a computational study of H_2 adsorption in graphite and showed that increasing the inter-layer spacing 60% could improve adsorption at room temperature from 0.9% to 2.3% (wt/wt) at P = 5 MPa = 50 bar, and that this might be due to a physical process whereby H_2 adsorption increases the graphite inter-layer distance in a feedback loop until it reaches the maximum adsorption allowed by entropy. Similar calculations by Patchkovskii et al. on graphene [37] show that the adsorption can almost double as inter-layer distance increases from 5.50 Å to 7Å. It was wondered if TMA2-Pc might be capable of following a similar process.

A TMA2-Pc crystal-only system using the same force field and Lennard-Jones
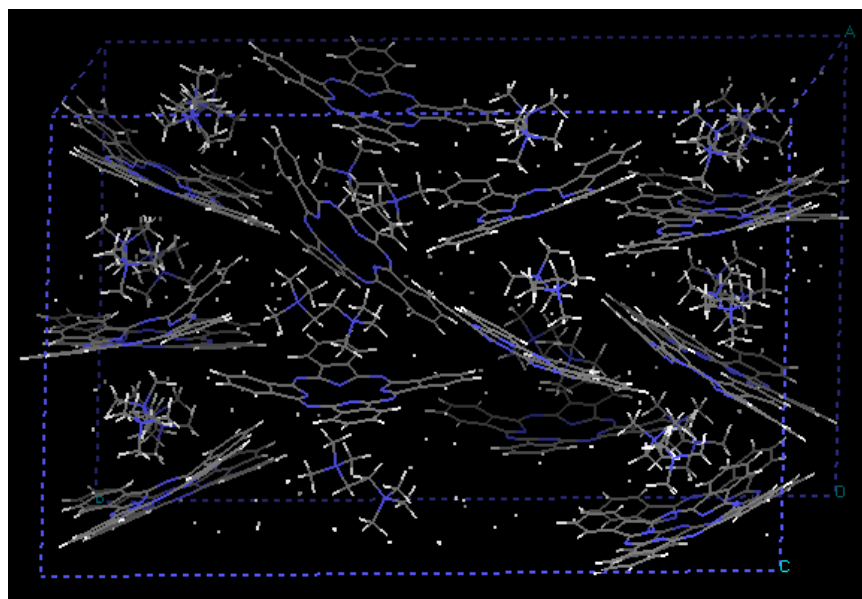
(a) Crystal + H$_2$
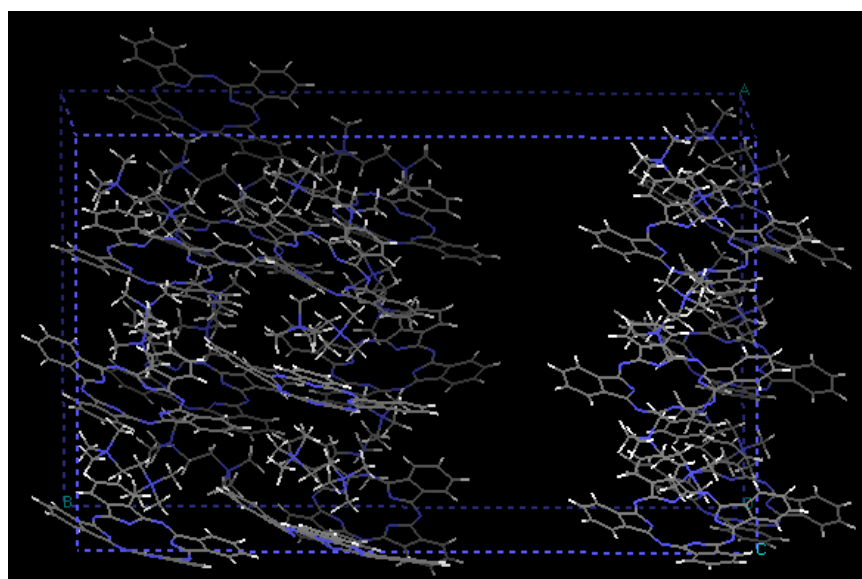
(b) Crystal only

Fig. 47. TMA2-Pc crystal structure

parameters as described in Chapter IV was constructed and approximately 2% (wt/wt) H_2 was added to it. The system ran for 400 ps with the first 200 ps used to reach equilibrium. Figure 47 A shows the final configuration of a system at T = 77 K. For comparison, Figure 47 B shows the final configuration of an identical system without the H_2 molecules. One can see that the Pc of the crystal + H_2 system are indeed separated slightly more and tilted to project more into the void space. Corresponding Pc atoms in the crystal only system are about 8.8 to 9.0 Å apart; in the crystal + H_2 system the atoms are 9.2 to 9.6 Å apart.

Unlike TMA-LiPc, the MD force field used here—which is based on generic force fields like DREIDING and UFF—produces structures that are regular crystals with clearly-defined Pc layers. Thus, it may be possible for TMA2-Pc to behave like the graphite system studied by Aga et al.: H_2 does increase the inter-layer distance which does correspondingly increases the total adsorption.

G.   Comparison of TMA-LiPc and TMA2-Pc H_2 adsorption behavior

Figure 48 shows the isotherms of both TMA-LiPc and TMA2-Pc at both of the available ILD. At all temperatures and pressures, TMA-LiPc shows both higher adsorption and higher slope of adsorption. This is also supported by the H_2 probability density graphs: graphs of the 20% surface for TMA-LiPc are most similar to graphs of the 10% surface for TMA2-Pc, implying that the adsorption of TMA2-Pc should be about half that of TMA-LiPc.

The binding energy surfaces do not visibly indicate that TMA-LiPc should be so significantly higher in binding energy than for TMA2-Pc. However, they can be analyzed quantitatively and suggest a higher adsorption for TMA-LiPc than TMA2-Pc. One can define the "available space" $V_{available}$ within a crystal unit cell
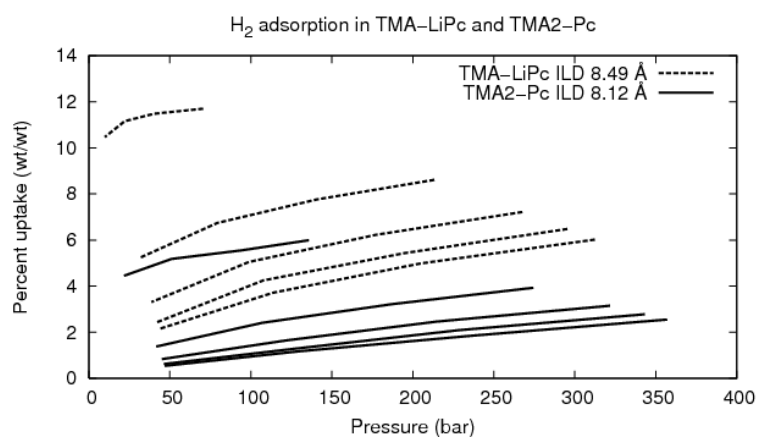
(a) TMA-LiPc ILD 8.49 Å and TMA2-Pc ILD 8.12 Å
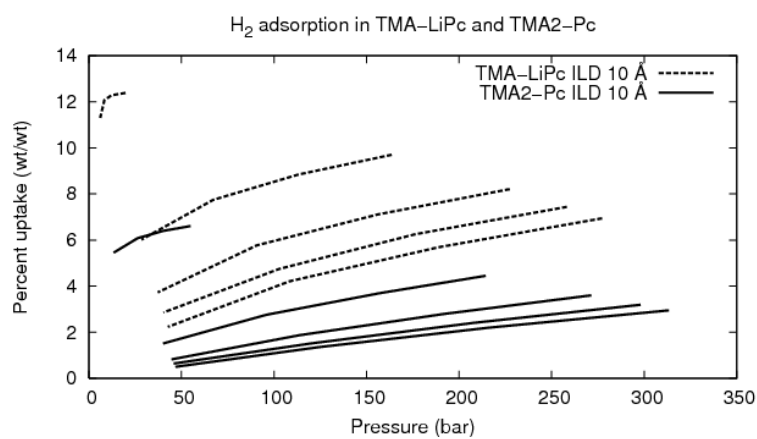
(b) TMA-LiPc and TMA2-Pc ILD 10 Å

Fig. 48. Comparison of TMA-LiPc and TMA2-Pc adsorption isotherms

as the number of points within that cell with a negative binding energy (i.e. not repulsed by the crystal atoms), and the "average unit cell binding energy" U_{avg} as the sum of binding energy potential taken only at every point within the available space. The ratio of these two terms for ILD ≈ 8 Å are:

$$\frac{U_{avg,TMA-LiPc,ILD\ 8.49Å}}{U_{avg,TMA2-Pc,ILD\ 8.12Å}} = 1.26$$

$$\frac{V_{available,TMA-LiPc,ILD\ 8.49Å}}{V_{available,TMA2-Pc,ILD\ 8.12Å}} = 1.44$$

Similarly for ILD 10 Å:

$$\frac{U_{avg,TMA-LiPc,ILD10\ Å}}{U_{avg,TMA2-Pc,ILD\ 10Å}} = 1.12$$

$$\frac{V_{available,TMA-LiPc,ILD\ 10Å}}{V_{available,TMA2-Pc,ILD\ 10Å}} = 1.23$$

In both cases TMA-LiPc has both greater available space and greater (more negative) average binding energy than TMA2-Pc. It is not immediately clear which parameter is more important important in controlling the adsorption behavior.

The available space immediately surrounding the cation (within 5 Å of the central nitrogen atom) is of particular interest. For TMA-LiPc, this area corresponds to both the first high peak on the $g_{ij}(r)$ graphs and the region of highest binding energy (between 0.9 and 1.2 kcal/mol). The binding energy is high due to the geometry: the Pc in TMA-LiPc layers above and below "box in" this space such that any H_2 in that space has many atoms surrounding it at about 3 Å to 5 Å away, and this distance is close to the minimum of the van der Waals potential for each site. However, TMA2-Pc has much less space available in this region due to the significantly larger cation. H_2 around the TMA2 cation are not near many atoms in the Pc layers above and below, as seen by directly comparing the binding energy graphs.

CHAPTER IV

Li ION TRANSPORT IN TMA2-PC

A.   Introduction

Other phthalocyanine salts have been tested for suitability for use as the lithium salt bridge in lithium ion batteries [33].   The governing transport property for this application is the binary diffusion coefficient of Li ion within the medium which can be estimated from MD results and related to the conductivity via the Nernst-Einstein equation [38]:

$$\kappa = \frac{c_{Li}\mathscr{D}_{\mathrm{Li}}z^2F^2}{RT}$$

Here c_{Li} is the concentration of Li ions, $\mathscr{D}_{\mathrm{Li}}$ is the diffusion coefficient, z is the charge on the Li ions (typically +1), F is the Faraday constant, R is the gas constant, and T is the temperature.

TMA2-Pc was studied in order to determine the diffusion coefficient of Li ion. The same geometry from the H_2 adsorption study in Chapter III was used for each crystal unit cell, however an orthorhombic cubic crystal structure was used instead of the paralleliped structure.

B.   MD force field

The MD systems were designed to estimate the diffusion of Li ion in solid TMA2-Pc. Unlike H_2 adsorption, the Li ions were dilute. It was thus necessary to use a force field that allowed the macromolecule to vibrate and deform in a manner consistent with molecular diffusion including its dependence on system properties like temperature and concentration of solute. The macromolecule force field de-

veloped here included terms for bond length, valence angle, dihedral angle, and non-bonded interactions. The Universal Force Field [39] (UFF) model was used for the bond length and valence angle terms, and the DREIDING model [32] was used for the dihedral angle and non-bonded interaction terms.

For the bond length (bond stretch) interaction, a harmonic oscillator function was used:

$$E_R = \frac{k}{2}\left(r - r_{ij}\right)^2 \ \text{kcal/mol}$$

$$k = 664.12 \frac{Z_i^* Z_j^*}{r_{ij}^3}$$

where r_{ij} is the ground-state bond length (Å) and Z_i^* and Z_j^* refer to the *effective charge* given in Table I of the UFF model (reproduced here in Table IV).

Table IV. UFF effective charge values

Atom	Z_i^*
H	0.712
Li	1.026
C	1.912
N	2.544
O	2.300

For the valence angle interaction, the SHAPES [40] Fourier expansion function was used with the UFF force constant A_{ijk}:

$$E_\theta = A_{ijk} \left[1 + \cos \left(m\theta - \delta \right) \right] \text{ kcal/mol}$$

$$m = \frac{\pi}{\pi - \theta_0}$$

$$\delta = -\pi + m\theta_0$$

$$= -\pi + \frac{\pi\theta_0}{\pi - \theta_0}$$

$$A_{ijk} = 664.12 \frac{Z_i^* Z_k^*}{r_{ik}^5} \left[3r_{ij}r_{jk} \left(1 - \cos^2 \theta_0 \right) - r_{ik}^2 \cos \theta_0 \right]$$

$$r_{ik} = \sqrt{r_{ij}^2 + r_{jk}^2 - 2r_{ij}r_{jk} \cos \theta_0}$$

where r_{ij} and r_{jk} are the ground-state bond lengths (Å), Z_i^* and Z_k^* refer to the effective charges of the terminal atoms, and θ_0 is the ground-state bond angle.

For the dihredral angle interaction, the DREIDING torsion potential was used.

$$E_{ijkl} = \frac{1}{2} V_{jk} \left[1 - \cos \left[n_{jk} \left(\phi - \phi_{jk}^0 \right) \right] \right] \text{ kcal/mol}$$

where ϕ_{jk}^0 is the dihedral angle at ground state, n_{jk} is the periodicity, and V_{jk} is a force constant dependent on the hybridization of the atoms in the central bond. V_{jk} and n_{jk} are determined as follows:

1. Two sp^3 atoms in a single bond: $V_{jk} = 2.0$ kcal/mol, $n_{jk} = 3$.

2. One sp^2 atom and one sp^3 atom in a single bond: $V_{jk} = 1.0$ kcal/mol, $n_{jk} = 6$.

3. Two sp^2 atoms in a double bond: $V_{jk} = 45.0$ kcal/mol, $n_{jk} = 2$.

4. Two sp^2 atoms in a resonant/aromatic bond: $V_{jk} = 25.0$ kcal/mol, $n_{jk} = 2$.

5. Two non-resonant sp^2 atoms, or one resonant atom and one non-resonant sp^2 atom, in a single bond (e.g. the middle bond of butadiene): $V_{jk} = 5.0$ kcal/mol,

$n_{jk} = 2.$

6. Two resonant sp^2 atoms in a single bond (e.g. the middle bond of biphenyl):

$V_{jk} = 10.0$ kcal/mol, $n_{jk} = 2$.

To convert to the DL_POLY cosine potential, the following transformation was required:

$$E_{ijkl} = A\left[1 + \cos\left(m\phi - \delta\right)\right] \text{ kcal/mol}$$

$$m = n_{jk}$$

$$A = \frac{V_{jk}}{2}$$

$$\delta = \pi - m\phi_{jk}^0$$

For the non-bonded interaction, the 12-6 Lennard-Jones potential function was used, with parameters derived from the Lorentz-Berthelot mixing rules. The pure species ϵ_i and σ_i values for C, N, H, O, and Cl were taken from DREIDING [32], and Li ion from [33]. All pure species values are shown in Table V.

Table V. TMA2-Pc Lennard Jones pure species parameters for Li ion transport

Atom	ϵ_i kcal/mol	σ_i Å
H	0.0152	2.8464
C	0.0951	3.4730
N	0.0774	3.2626
O	0.0957	3.0332
Li	0.0359	2.3700
Cl	0.2833	3.5193

Perchlorate was chosen as the counter-ion for the Li^+ due to its experimental familiarity [41] [42] [43] [44].

C. MD procedure

A simple stacked cubic system was chosen with unit cell vectors a = 8.38 Å, b = c = 13.85 Å. 8.38 Å was the inter-layer distance and 13.85 Å was the inter-molecule distance in accordance with earlier studies involving phthalocyanine [33]. The concentration of Li^+ and perchlorate (ClO_4^-) ions were controlled by altering both the number of salt dimers and the number of unit cells of the crystal. A rectangular orthorhombic periodic boundary condition was used. The force field for the TMA2-Pc molecules included bond stretch, bond angle, dihedral angle, and Lennard-Jones non-bonded interactions. The Li^+ and ClO_4^- ions had only Lennard-Jones non-bonded interactions. The bond lengths between the Cl and O in ClO_4^- were fixed at 1.5 Å. The atomic charges for the TMA2-Pc molecule were taken from the APT charges from a frequency calculation at the HF/6-31g level; the atomic charges for the ClO_4^- ion were taken from the APT charges from a frequency calculation at the B3LYP/6-31g(d,p) level. The Li^+ ion charge was set at +1.0.

Each simulation ran for a total of 700 ps, with the first 300 ps used to reach equilibrium. System configurations were recorded every 1 ps for the remaining 500 ps, for a total of 401 recorded system configurations. Figure 49 shows one example of the beginning and ending configurations.

D. Results and discussion

1. Li ion binary diffusion coefficient

The Li ion binary diffusion coefficient as a function of temperature and concentration is shown in Figure 50. The raw data is reported in Appendix A Table XII. The systems were stable; the MSD function were not perfectly smooth, but were
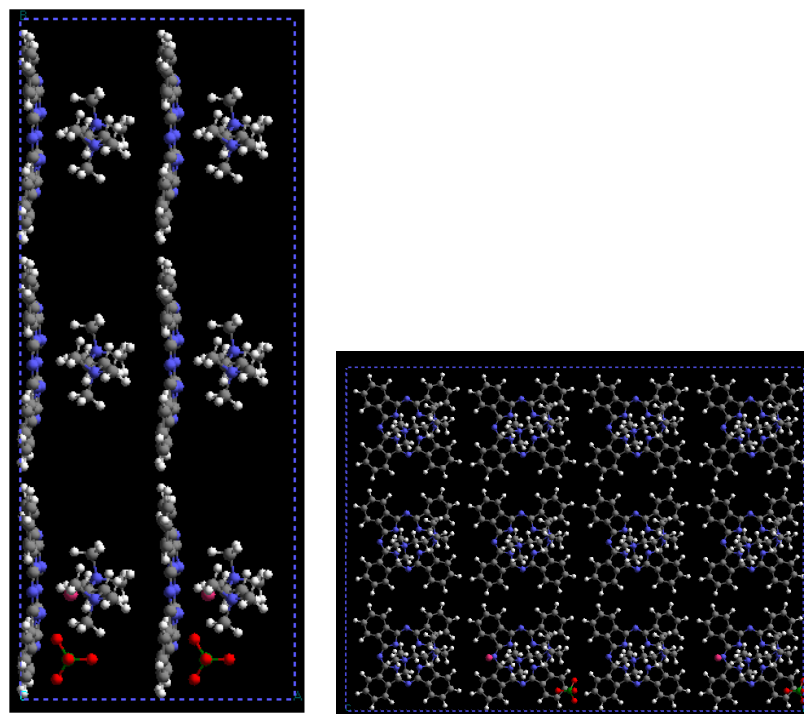
(a) Start
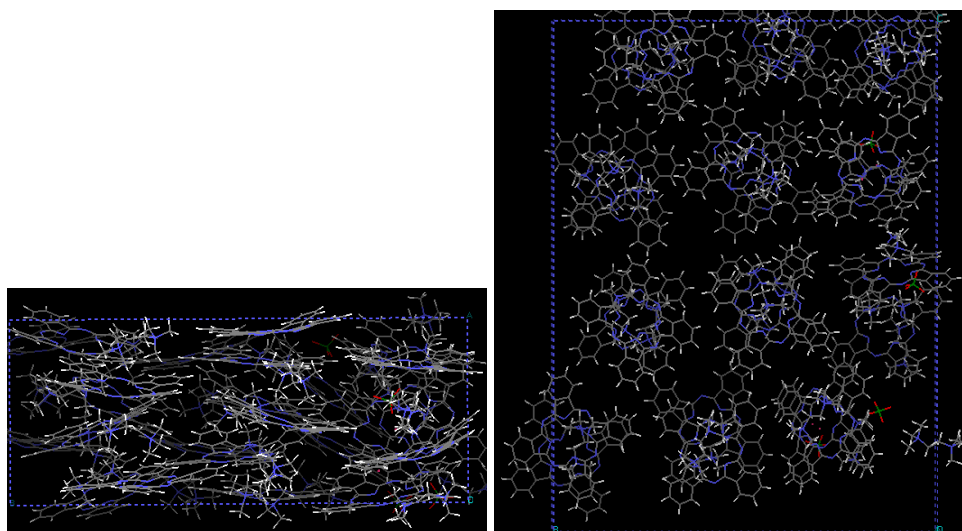
(b) End

Fig. 49. TMA2-Pc Li ion start and end configurations

oscillating regularly along a linear slope and hence the diffusion coefficients reported are reasonable. Figures 51 and 52 show the stability criteria and MSD for a representative system.

As shown in Figure 50, the lithium ion diffusion coefficient did not correlate well with temperature or concentration. Also, the values on the order of 10^{-5} cm^2/s differ significantly from experimental values of other carbon-based systems. Uchida et al. reported $\mathscr{D}_{Li}$ values between 10^{-12} and $10^{-9.5}$ cm^2/s in carbon fiber [45]; Wang et al. reported $\mathscr{D}_{Li}$ values between 10^{-10} and 10^{-7} cm^2/s in graphitized mesocarbon microbeads [46].

One possible explanation for the strange results is that the crystal structure of the TMA2-Pc changes with concentration of Li ion and counter-ion. Figure 53 shows sample systems at low, medium, and high concentrations. At low concentrations, the crystal is in a staggered arrangement with Pc anions "zig-zag"-like alternating angles between layers. At high concentrations the Pc anions are in a more "stair-step" arrangement, mostly remaining horizontal but alternating with the TMA2 cation. Medium concentrations show an intermediate structure. Since the crystal structure is not fixed, the transport properties of the Li ion may change with each new type of structure.

Fig. 50. TMA2-Pc Li ion binary diffusion coefficient

Li−TMA2−Pc velocity autocorrelation function (Å^2/ps^2) vs time
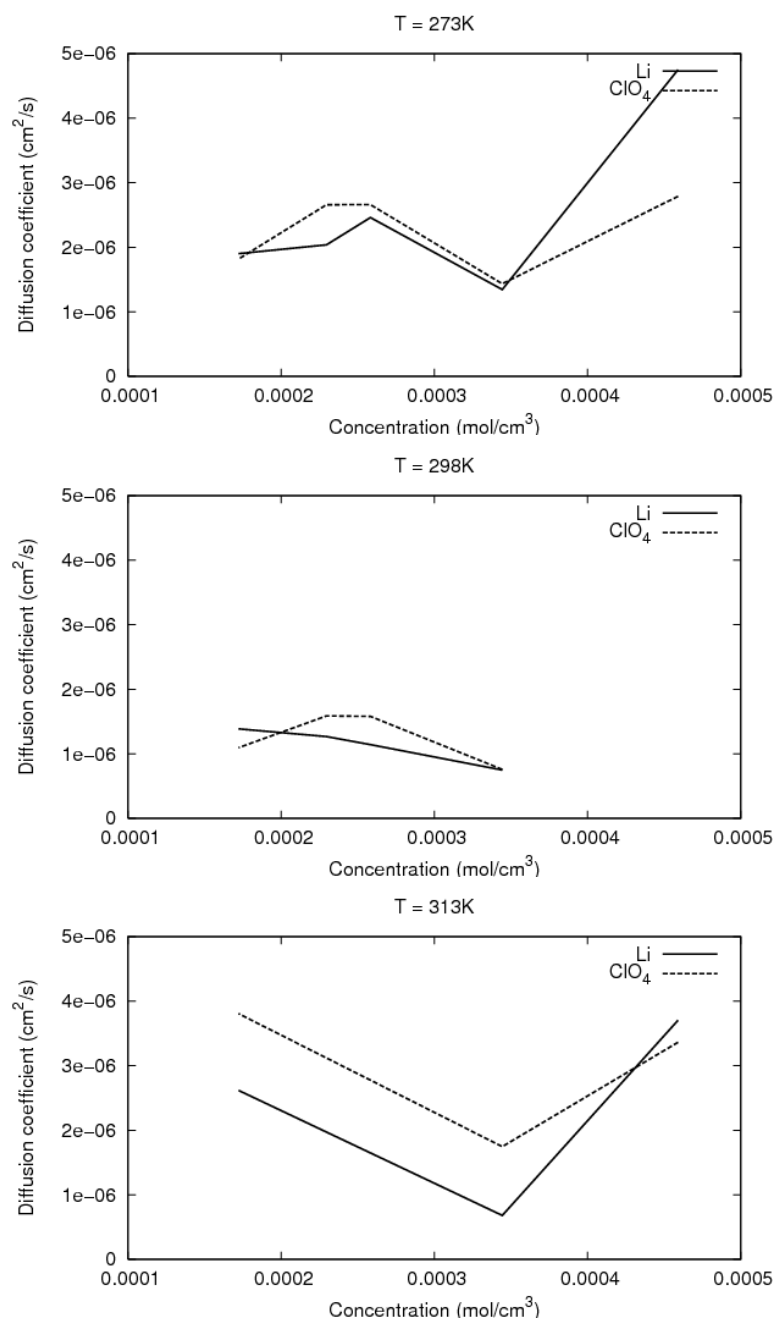
(a) Mechanically stable
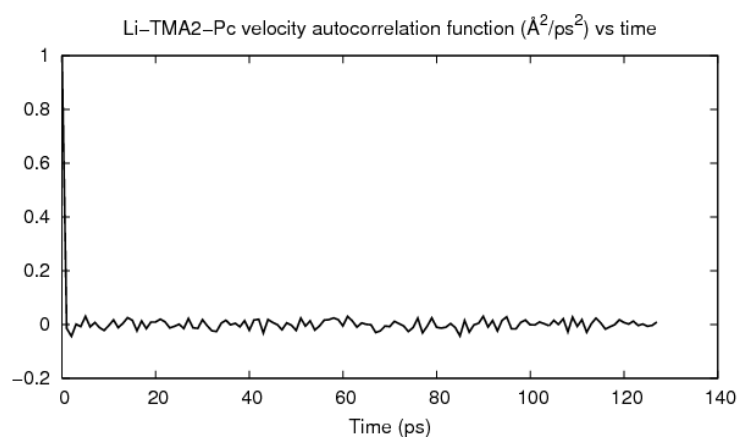
Li−TMA2−Pc energy (kcal/mol) vs time
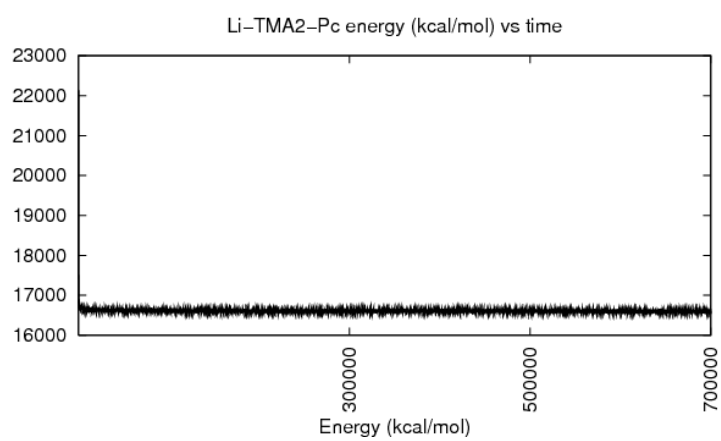
(b) Energetically stable

Fig. 51. TMA2-Pc system stability
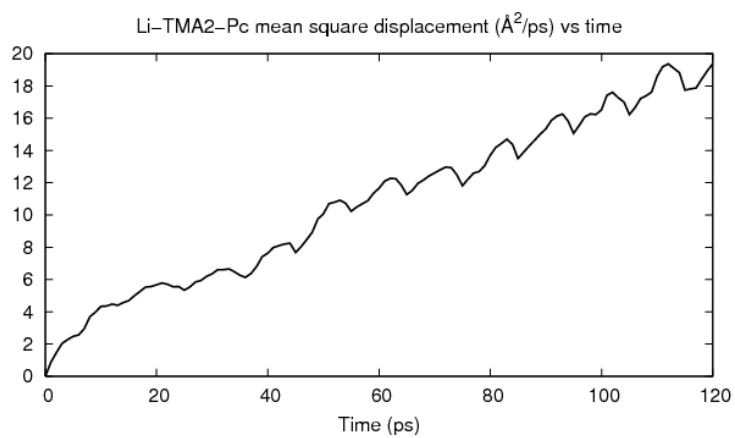
Fig. 52. TMA2-Pc system sample MSD
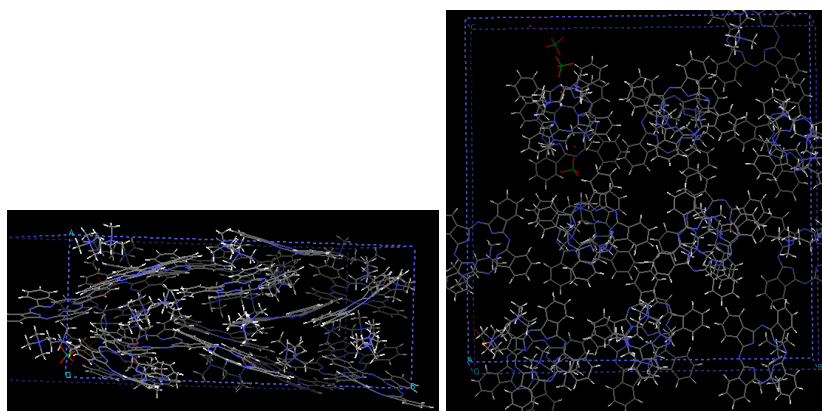
(a) Low concentration
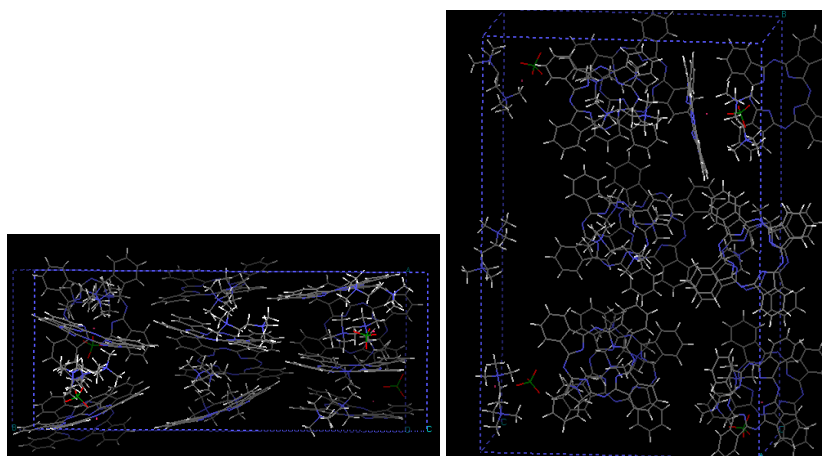
(b) Medium concentration
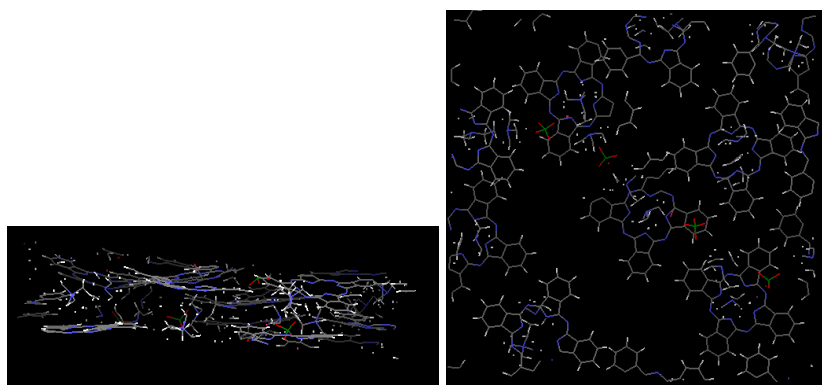
(c) High concentration

Fig. 53. TMA2-Pc Li ion - crystal structure changes by concentration

CHAPTER V

CONCLUSIONS

Phthalocyanine salts have the potential to adsorb enough H_2 to meet the Department of Energy H_2 storage targets. Whether or not they will do so in actuality depends first on the cation and second on the real crystal structure of the salt. The TMA-LiPc salt in a stacked cubic crystal structure looks very promising with adsorption in the range of 2% (wt/wt) at room temperature, 6% at 177 K, and 11% at 77 K, all at pressures less than 50 bar. However, the stacked cubic crystal structure does not appear to be the most physically likely. The first recommendation for future work is to determine a stable crystal structure for TMA-LiPc.

The TMA2-Pc salt appears to have a stable crystal structure not unlike the staggerred paralleliped arrangement tested in this study, and at 77 K and 55 bar it too can meet the Department of Energy minimum storage target of 6% uptake (wt/wt). It also seems to share the positive feedback loop of graphite identified by Aga et al. that leads to an increase in the H_2 adsorbtion. Finally, it has a much stronger permanent dipole than TMA-LiPc that may result in increased adsorption. Though its uptake is significantly less than the MD results for TMA-LiPc, it may be that TMA2-Pc is in fact more physically realizable than TMA-LiPc, and thus TMA2-Pc could be a viable place to start from to find a structure that meets the 12% uptake (wt/wt) target at commodity temperatures and pressures. The second recommendation for future work is physical synthesis and testing of TMA2-Pc or another phthalocyanine salt with an even larger cation.

REFERENCES

[1] S. I. Sandler, *Chemical, Biochemical, and Engineering Thermodynamics*, John Wiley & Sons, Inc., Hoboken, NJ, 4th edition, 2006.

[2] G. Thomas, "Overview of storage development DOE Hydrogen Program," in *US DOE Hydrogen Program 2000 Annual Review*, Sandia National Laboratories, Livermore, CA, May 2000.

[3] U.S. Department of Energy, "National Hydrogen Energy Roadmap," United States Department of Energy, Washington, DC, 2002.

[4] A. C. Dillon, K. M. Jones, T. A. Bekkedahl, C. H. Kiang, D. S. Bethune, and M. J. Heben, "Storage of hydrogen in single-walled carbon nanotubes," *Nature*, vol. 386, no. 6623, pp. 377–379, 1997.

[5] S. Yamanaka, M. Fujikane, M. Uno, H. Murakami, and O. Miura, "Hydrogen content and desorption of carbon nano-structures," *Journal of Alloys and Compounds*, vol. 366, no. 1–2, pp. 264–268, 2004.

[6] E. Poirier, R. Chahine, P. Bénard, D. Cossement, L. Lafi, E. Mélancon, T.K. Bose, and S. Désilets, "Storage of hydrogen on single-walled carbon nanotubes and other carbon structures," *Appl. Phys. A*, vol. 78, pp. 961–967, 2004.

[7] V. Gayathri and R. Geetha, "Hydrogen adsorption in defected carbon nanotubes," *Adsorption*, vol. 13, pp. 53–59, 2007.

[8] P. Hou, S. Xu, Z. Ying, Q. Yang, C. Liu, and H. Cheng, "Hydrogen adsorption / desorption behavior of multi-walled carbon nanotubes with different diameters," *Carbon*, vol. 41, pp. 2471–2476, 2003.

[9] Y. Zhang, "Computation Study of the Transport Mechanisms of Molecules and Ions in Solid Materials," Ph.D. dissertation, Texas A&M University, College Station, 2006.

[10] A. Szabo and N. S. Ostlund, *Modern Quantum Chemistry*, Dover Publications, Inc., Mineola, NY, 1st edition, 1989.

[11] P. Hohenberg and W. Kohn, "Inhomogeneous electron gas," *Physical Review*, vol. 136, no. 3B, pp. B864–B871, 1964.

[12] J. B. Foresman and Æ . Frisch, *Exploring Chemistry with Electronic Structure Methods*, Gaussian Inc., Pittsburgh, PA, 2nd edition, 1996.

[13] P. J. Stephens, F. J. Devlin, C. F. Chabalowski, and M. J. Frisch, "*Ab Initio* calculation of vibrational absorption and circular dichroism spectra using density functional force fields," *Journal of Physical Chemistry*, vol. 98, no. 45, pp. 11623–11627, 1994.

[14] Michael J. S. Dewar, Eve G. Zoebisch, Eamonn F. Healy, and James J. P. Stewart, "AM1: a new general purpose quantum mechanical molecular model," *Journal of the American Chemical Society*, vol. 107, no. 13, pp. 3902–3909, 1985.

[15] J. J. P. Stewart, "Optimization of parameters for semiempirical methods II. Applications," *Journal of Computational Chemistry*, vol. 10, no. 2, pp. 221–264, 1989.

[16] R. A. Serway, *Physics for Scientists & Engineers*, Harcourt Brace & Company, Orlando, FL, 3rd edition, 1992.

[17] D. Xenides, B. R. Randolf, and B. M. Rode, "Hydrogen bonding in liquid water: An *ab initio* QM/MM MD simulation study," *Journal of Molecular Liquids*, vol. 123, no. 2-3, pp. 61–67, 2006.

[18] K. Meier, A. Laesecke, and S. Kabelac, "Transport coefficients of the Lennard-Jones model fluid. II Self-diffusion," *The Journal of Chemical Physics*, vol. 121, no. 19, pp. 9526–9535, 2004.

[19] A. Hinchliffe, *Molecular Modelling for Beginners*, John Wiley & Sons Ltd., Orlando, FL, 1st edition, 2003.

[20] M. J. Frisch, G. W. Trucks, H. B. Schlegel, G. E. Scuseria, M. A. Robb, J. R. Cheeseman, J. A. Montgomery, Jr., T. Vreven, K. N. Kudin, J. C. Burant, J. M. Millam, S. S. Iyengar, J. Tomasi, V. Barone, B. Mennucci, M. Cossi, G. Scalmani, N. Rega, G. A. Petersson, H. Nakatsuji, M. Hada, M. Ehara, K. Toyota, R. Fukuda, J. Hasegawa, M. Ishida, T. Nakajima, Y. Honda, O. Kitao, H. Nakai, M. Klene, X. Li, J. E. Knox, H. P. Hratchian, J. B. Cross, V. Bakken, C. Adamo, J. Jaramillo, R. Gomperts, R. E. Stratmann, O. Yazyev, A. J. Austin, R. Cammi, C. Pomelli, J. W. Ochterski, P. Y. Ayala, K. Morokuma, G. A. Voth, P. Salvador, J. J. Dannenberg, V. G. Zakrzewski, S. Dapprich, A. D. Daniels, M. C. Strain, O. Farkas, D. K. Malick, A. D. Rabuck, K. Raghavachari, J. B. Foresman, J. V. Ortiz, Q. Cui, A. G. Baboul, S. Clifford, J. Cioslowski, B. B. Stefanov, G. Liu, A. Liashenko, P. Piskorz, I. Komaromi, R. L. Martin, D. J. Fox, T. Keith, M. A. Al-Laham, C. Y. Peng, A. Nanayakkara, M. Challacombe, P. M. W. Gill, B. Johnson, W. Chen, M. W. Wong, C. Gonzalez, and J. A. Pople, *Gaussian 03, Revision C.02*, Gaussian, Inc., Wallingford, CT, 2004.

[21] W. Smith, C. W. Yong, and P. M. Rodger, "DL_POLY: Application to molecular

simulation," *Molecular Simulation*, vol. 28, pp. 385–471, 2002.

[22] R. Dennington II, T. Keith, J. Millam, K. Eppinnett, W. L. Hovell, and R. Gilliland, *GaussView, Version 3.09*, Semichem, Inc., Shawnee Mission, KS, 2003.

[23] Molecular Simulations Inc., *CERIUS 2*, San Deigo, CA, 1997.

[24] T. Williams, C. Kelley, J. Campbell, D. Kotz, and R. Lang, *GNUPLOT-An Interactive Plotting Program*, Free Software Foundation, Boston, MA, Aug 1990.

[25] J. W. Eaton and J. B. Rawlings, *Ten Years of Octave - Recent Developments and Plans for the Future*, Retrieved from: http://citeseer.ist.psu.edu/eaton03ten.html, Jan 2008.

[26] K. Lamonte, "ChENL: The ChemE Numerical Library," College Station, TX, 2007.

[27] F. H. Allen, "The Cambridge Structural Database: a quarter of a million crystal structures and rising," *Acta Crystallographica Section B*, vol. 58, no. 3 Part 1, pp. 380–388, Jun 2002.

[28] J. M. Prausnitz, R. N. Lichtenthaler, and E. G. Azevedo, *Molecular Thermodynamics of Fluid Phase Equilibria*, Prentice Hall, Upper Saddle River, NJ, 3rd edition, 1999.

[29] C. G. Gray and K. E. Gubbins, *Theory of Molecular Fluids*, vol. 1, Clarendon Press, Oxford, England, 1984.

[30] E. Ishiguro, T. Arai, M. Mizushima, and M. Kotani, "On the polarizability of the hydrogen molecule," *Proceedings of the Physical Society*, vol. 65, no. 3, pp. 178–187, 1952.

[31] Q. Wang and J. K. Johnson, "Phase equilibrium of quantum fluids from simulation: Hydrogen and neon," *Fluid Phase Equilibria*, vol. 132, pp. 93–116, 1997.

[32] S. L. Mayo, B. D. Olafson, and W. A. Goddard III, "DREIDING: A generic force field for molecular simulations," *J. Phys. Chem.*, vol. 94, pp. 8897–8909, 1990.

[33] Y. Zhang, P. R. Alonso, A. Martinez-Limia, L. G. Scanlon, and P. B. Balbuena, "Crystalline structure and lithium-ion channel formation in self-assembled di-lithium phthalocyanine: theory and experiments," *J. Phys. Chem. B*, vol. 108, no. 15, pp. 4659–4668, 2004.

[34] D. E. Seborg, T. F. Edgar, and D. A. Mellichamp, *Process Dynamics and Control*, John Wiley & Sons, Inc., Hoboken, NJ, 2nd edition, 2004.

[35] P. Diep and J. K. Johnson, "An accurate H_2-H_2 interaction potential from first principles," *J. Phys. Chem.*, vol. 112, pp. 4465–4472, March 2000.

[36] R. S. Aga, C. L. Fu, M. Krčmar, and J. R. Morris, "Theoretical investigation of the effect of graphite interlayer spacing on hydrogen absorption," *Physical Review B (Condensed Matter and Materials Physics)*, vol. 76, no. 16, pp. 165404–1—165404–7, 2007.

[37] S. Patchkovskii, J. S. Tse, S. N. Yurchenko, L. Zhechkov, T. Heine, and G. Seifert, "Graphene nanostructures as tunable storage media for molecular hydrogen,"

PNAS, vol. 102, no. 30, pp. 10439–10444, 2005.

[38] R. B. Bird, W. E. Stewart, and E. N. Lightfoot, *Transport Phenomena*, John Wiley & Sons, Inc., New York, 1st edition, 1960.

[39] A. K. Rappé, C. J. Casewit, K. S. Cowell, W. A. Goddard III, and W. M. Skiff, "UFF, a full periodic table force field for molecular mechanics and molecular dynamics simulations," *J. Am. Chem. Soc.*, vol. 114, pp. 10024–10035, 1992.

[40] V. S. Allured, C. M. Kelly, and C. R. Landis, "SHAPES empricial force field: New treatment of angular potentials and its application to square-planar transition-metal complexes," *J. Am. Chem. Soc.*, vol. 113, pp. 1–12, 1991.

[41] T. Piao, S. Park, C. Doh, and S. Moon, "Intercalation of lithium ions into graphite electrodes studied by AC impedance measurements," *Journal of the Electrochemical Society*, vol. 146, pp. 2794–2798, 1999.

[42] A. Funabiki, M. Inaba, Z. Ogumi, S. Yuasa, J. Otsuji, and A. Tasaka, "Impedance study on the electrochemical lithium intercalation into natural graphite powder," *Journal of the Electrochemical Society*, vol. 145, no. 1, pp. 172–178, 1998.

[43] M. Wakihara, "Recent developments in lithium ion batteries," *Materials Science and Engineering: R: Reports*, vol. 33, pp. 109–134, June 2001.

[44] T. Furukawa, Y. Mukasa, T. Suzuki, and K. Kano, "Microphase separation and ion-conduction mechanisms in polypropylene oxide/lithium perchlorate (liclo$_4$) complexes," *Journal of the Electrochemical Society*, vol. 40, pp. 613–622, 2002.

[45] T. Uchida, Y. Morikawa, H. Ikuta, M. Wakihara, and K. Suzuki, "Chemical diffusion coefficient of lithium in carbon fiber," *Journal of the Electrochemical Society*, vol. 143, no. 8, pp. 2606–2610, 1996.

[46] Q. Wang, H. Li, X. Huang, and L. Chen, "Determination of chemical diffusion coefficient of lithium ion in graphitized mesocarbon microbeads with potential relaxation technique," *Journal of the Electrochemical Society*, vol. 148, no. 7, pp. A737–A741, 2001.

APPENDIX A

Table VI. TMA-LiPc system geometry

Atom label	X Å	Y Å	Z Å	ϵ_i kcal/mol	σ_i Å
C1	4.2232	4.9814	4.8287	0.190	3.30
C6	3.6139	4.5711	7.1726	0.190	3.30
C7	3.2282	6.7905	6.1576	0.190	3.30
C8	5.5211	6.0282	6.6407	0.066	2.90
C18	0.4654	1.6227	2.4247	0.175	3.30
C19	0.4095	1.9379	3.7815	0.175	3.30
C20	0.4942	2.6332	1.4437	0.175	3.30
C22	0.3850	3.2877	4.1399	0.164	3.21
C23	0.4671	3.9812	1.7976	0.175	3.30
C26	0.3302	3.9782	5.4312	0.220	3.25
C27	0.4124	4.3011	3.1561	0.164	3.21
C30	0.3737	5.5731	3.8824	0.220	3.25
C32	0.2715	3.9416	7.7867	0.220	3.25
C35	0.2957	3.2129	9.0601	0.164	3.21
C36	0.3802	7.9242	3.9175	0.220	3.25
C40	0.3174	1.8556	9.3825	0.180	3.25
C41	0.2834	5.4912	9.3731	0.220	3.25
C42	0.3043	4.1988	10.0688	0.164	3.21
C43	0.4253	9.2199	3.2282	0.164	3.21
C44	0.3183	7.8407	9.4094	0.220	3.25
C45	0.3462	9.4297	7.8633	0.220	3.25
C46	0.3650	9.4640	5.5138	0.220	3.25
C47	0.3475	1.5051	10.7326	0.180	3.25

Atom label	X Å	Y Å	Z Å	ϵ_i kcal/mol	σ_i Å
C49	0.4156	10.1984	4.2424	0.164	3.21
C50	0.4736	9.5800	1.8821	0.180	3.25
C51	0.3349	3.8467	11.4180	0.180	3.25
C54	0.3641	9.1152	10.1405	0.164	3.21
C55	0.3812	10.1246	9.1583	0.164	3.21
C56	0.3564	2.4889	11.7387	0.180	3.25
C57	0.5110	10.9402	1.5714	0.180	3.25
C58	0.4542	11.5568	3.9314	0.180	3.25
C62	0.3925	9.4320	11.4974	0.175	3.30
C63	0.4280	11.4719	9.5114	0.175	3.30
C64	0.5017	11.9166	2.5836	0.180	3.25
C68	0.4382	10.7818	11.8514	0.175	3.30
C70	0.4559	11.7893	10.8708	0.175	3.30
N2	4.1536	5.5943	6.2029	0.100	3.10
N29	0.3134	3.3279	6.6006	0.120	3.05
N31	0.3309	5.3313	5.2277	0.120	3.05
N33	0.4056	6.7603	3.2684	0.120	3.05
N37	0.2594	5.2869	8.0253	0.120	3.05
N38	0.3055	8.0815	8.0658	0.120	3.05
N39	0.3384	8.1234	5.2698	0.120	3.05
N48	0.3113	6.6584	10.0243	0.120	3.05
N53	0.3702	10.0798	6.6991	0.120	3.05
H3	4.6044	5.7271	4.1304	0.066	2.90
H4	4.8898	4.1186	4.8605	0.066	2.90
H5	3.2204	4.6733	4.5326	0.066	2.90
H9	3.4988	5.0399	8.1494	0.066	2.90
H10	2.6465	4.2200	6.8183	0.066	2.90
H11	4.3217	3.7429	7.2274	0.066	2.90
H12	3.6629	7.5393	5.4948	0.066	2.90
H13	2.2618	6.4607	5.7782	0.066	2.90

Atom label	X Å	Y Å	Z Å	ϵ_i kcal/mol	σ_i Å
H14	3.1096	7.1899	7.1644	0.066	2.90
H15	5.9022	6.7665	5.9346	0.066	2.90
H16	5.4462	6.4707	7.6343	0.066	2.90
H17	6.1814	5.1602	6.6679	0.066	2.90
H21	0.4819	0.5816	2.1145	0.066	2.90
H24	0.5326	2.3530	0.3947	0.066	2.90
H25	0.3790	1.1655	4.5436	0.066	2.90
H28	0.4807	4.7660	1.0479	0.066	2.90
H52	0.3051	1.1022	8.6009	0.066	2.90
H59	0.4767	8.8198	1.1073	0.066	2.90
H60	0.3381	4.6128	12.1869	0.066	2.90
H61	0.3603	0.4562	11.0158	0.066	2.90
H65	0.5450	11.2535	0.5316	0.066	2.90
H66	0.4440	12.3034	4.7191	0.066	2.90
H67	0.3767	2.1825	12.7808	0.066	2.90
H69	0.3760	8.6480	12.2479	0.066	2.90
H71	0.4387	12.2424	8.7471	0.066	2.90
H72	0.5290	12.9673	2.3082	0.066	2.90
H73	0.4580	11.0619	12.9010	0.066	2.90
H74	0.4893	12.8304	11.1794	0.066	2.90
Li34	0.0640	6.7143	6.6554	0.230	2.55

Table VII. TMA2-Pc system geometry

Atom label	X Å	Y Å	Z Å	ϵ_i kcal/mol	σ_i Å	w_i
C1	5.6550	6.2135	7.7397	0.07729	3.27221	-0.0611
C6	4.1209	4.7319	6.5245	0.07590	3.27547	0.0494
C7	5.1779	6.6913	5.4065	0.07890	3.26912	0.0041
C8	3.3966	7.0172	7.1385	0.08141	3.26338	0.0173
C17	4.2122	6.6360	4.2169	0.08112	3.26461	-0.0435
C21	3.9672	6.9702	1.7799	0.07927	3.26846	0.0310
C22	4.4399	8.9158	3.2148	0.07948	3.26806	0.0357
C23	6.1855	7.2370	2.7651	0.07958	3.26798	0.0833
C33	0.3243	2.4274	11.3434	0.07686	3.27266	-0.2742
C34	0.4532	3.7867	11.0412	0.07929	3.26846	0.0438
C35	0.3831	1.4537	10.3333	0.07837	3.27007	-0.0538
C37	0.6528	4.1447	9.7107	0.07648	3.27391	-0.0747
C38	0.5728	1.8146	8.9957	0.08183	3.26406	0.2393
C41	0.8250	5.4434	9.0222	0.08863	3.24974	-0.1206
C42	0.7113	3.1674	8.6967	0.08157	3.26406	0.0916
C45	0.9193	3.9168	7.4383	0.07280	3.28297	0.0704
C47	0.8471	7.8046	9.0904	0.08048	3.26574	-0.0215
C49	0.7700	9.0691	9.8545	0.07981	3.26738	0.0353
C50	1.0394	3.9714	5.0838	0.06666	3.29886	0.1312
C53	0.6238	9.3618	11.2076	0.07905	3.26889	0.0244
C54	1.0064	9.4110	7.5931	0.07168	3.28570	0.0833
C55	0.8729	10.0980	8.8954	0.08059	3.26589	0.0598
C56	0.7978	3.3062	3.7920	0.07792	3.27106	-0.0233
C57	1.1048	5.5699	3.5653	0.08500	3.25629	-0.0615
C58	0.5883	10.7066	11.5889	0.07896	3.26907	0.0319
C60	0.8369	4.3289	2.8196	0.07592	3.27514	-0.0782
C61	0.5366	1.9846	3.4324	0.07568	3.27511	-0.2152
C62	0.8316	11.4370	9.2745	0.07754	3.27160	-0.0923
C64	1.1319	9.4627	5.2407	0.08442	3.25753	-0.0587
C66	0.6907	11.7313	10.6342	0.07973	3.26777	0.1440

Atom label	X Å	Y Å	Z Å	ϵ_i kcal/mol	σ_i Å	w_i
C67	0.3364	1.6973	2.0807	0.07932	3.26846	0.0750
C68	0.6089	4.0438	1.4727	0.07618	3.27417	-0.1735
C73	1.1063	7.9437	3.6377	0.06958	3.29137	0.0902
C74	0.8919	10.2021	3.9919	0.07877	3.26937	0.0010
C75	0.3707	2.7160	1.1116	0.07777	3.27112	-0.1245
C79	0.8605	9.2289	2.9652	0.07241	3.28269	0.1731
C80	0.6763	11.5515	3.7048	0.07850	3.26987	-0.0164
C82	0.6108	9.5959	1.6395	0.08264	3.26260	0.2600
C83	0.4534	11.9162	2.3769	0.07816	3.27043	-0.0731
C85	0.4187	10.9481	1.3546	0.07957	3.26803	0.1048
N2	4.5851	6.1589	6.6879	0.07078	3.16478	0.0037
N18	4.7187	7.4428	3.0129	0.07176	3.16278	-0.0293
N44	0.7897	6.6049	9.6881	0.06682	3.17391	-0.0655
N46	1.0059	5.2458	7.6920	0.05616	3.20818	-0.0649
N48	0.9622	3.3080	6.2467	0.07839	3.14889	0.1023
N51	0.9882	8.0667	7.7715	0.08021	3.14252	0.0383
N52	1.2856	5.2967	4.8869	0.09567	3.11102	0.0838
N59	1.0878	10.0716	6.4346	0.07117	3.16392	0.0019
N65	1.0889	6.7734	2.9711	0.07140	3.16340	0.0044
N72	1.3175	8.1399	4.9661	0.06770	3.17323	-0.0115
H3	5.9681	7.2493	7.8780	0.03179	2.95491	-0.0126
H4	5.2348	5.8350	8.6706	0.03283	2.95077	-0.0453
H5	6.5027	5.5959	7.4362	0.03439	2.94545	-0.1614
H9	3.2654	4.7237	5.8480	0.03380	2.94548	0.0163
H10	4.9561	4.1289	6.1600	0.03365	2.94750	0.0602
H11	3.7847	4.3754	7.4963	0.03301	2.94954	0.0222
H12	5.4760	7.7196	5.6267	0.03088	2.95870	0.0152
H13	6.0808	6.1038	5.2186	0.02946	2.96470	0.0783
H14	2.5200	6.8530	6.5047	0.05459	2.86067	0.0299
H15	3.1525	6.7025	8.1481	0.02501	2.99275	0.0418
H16	3.7228	8.0582	7.1239	0.03457	2.94235	-0.0244
H19	3.2283	7.0417	4.4816	0.03425	2.94321	0.0160
H20	4.0787	5.6139	3.8639	0.02563	2.98567	-0.0975
H24	4.2373	7.6298	0.9544	0.03355	2.94864	-0.1651

Atom label	X Å	Y Å	Z Å	ϵ_i kcal/mol	σ_i Å	w_i
H25	4.2817	5.9482	1.5640	0.02474	2.98727	0.3962
H26	2.8872	6.9951	1.9770	0.03011	2.96206	0.0384
H27	4.9329	9.2559	4.1252	0.03090	2.95852	0.0217
H28	4.8388	9.4574	2.3565	0.03142	2.95636	0.0038
H29	3.3625	9.0643	3.2886	0.04023	2.92486	0.2029
H30	6.7695	7.6800	3.5713	0.02973	2.96304	0.1497
H31	6.3890	6.1679	2.6903	0.03140	2.95645	0.0069
H32	6.4465	7.7239	1.8253	0.03126	2.95694	0.0268
H36	0.1706	2.1171	12.3737	0.03336	2.94979	-0.3793
H39	0.2728	0.4052	10.5977	0.03151	2.95603	-0.0073
H40	0.3978	4.5477	11.8136	0.02916	2.96545	0.1799
H43	0.6069	1.0692	8.2067	0.02750	2.97286	0.2988
H63	0.5372	8.5625	11.9374	0.03234	2.95291	-0.0672
H69	0.4885	1.2093	4.1909	0.03818	2.93374	-0.4585
H70	0.9021	12.2237	8.5292	0.03193	2.95444	-0.0337
H71	0.4754	10.9660	12.6383	0.03155	2.95588	-0.0157
H76	0.1394	0.6745	1.7704	0.03004	2.96145	0.2606
H77	0.6059	4.8386	0.7322	0.03376	2.94777	-0.1487
H78	0.6545	12.7677	10.9598	0.03037	2.96015	0.2196
H81	0.1964	2.4643	0.0686	0.03329	2.94996	-0.3202
H84	0.6793	12.2872	4.5033	0.03139	2.95648	0.0057
H86	0.5516	8.8417	0.8597	0.02676	2.97661	0.3088
H87	0.2904	12.9607	2.1249	0.03225	2.95345	-0.1375
H88	0.2252	11.2611	0.3319	0.02978	2.96246	0.2978

Table VIII. TMA-LiPc H_2 adsorption isotherms

	ILD = 8.49 Å		ILD = 10 Å	
	Pres. (bar)	% (wt/wt)	Pres. (bar)	% (wt/wt)
T = 77 K	9.865	10.47	6.111	11.30
	22.141	11.16	8.354	12.07
	40.339	11.48	12.290	12.28
	70.534	11.70	19.765	12.38
T = 177 K	31.461	5.23	28.399	6.02
	79.282	6.74	67.149	7.74
	140.568	7.76	113.085	8.84
	213.286	8.61	163.624	9.70
T = 236 K	38.664	3.31	37.187	3.73
	98.816	5.05	90.741	5.77
	176.779	6.22	156.122	7.11
	267.588	7.22	227.347	8.21
T = 273 K	41.885	2.43	40.351	2.86
	107.715	4.25	102.602	4.74
	194.734	5.43	176.349	6.25
	295.434	6.48	258.219	7.44
T = 300 K	42.919	2.13	42.655	2.23
	113.656	3.71	108.440	4.21
	204.481	4.98	189.076	5.69
	312.345	6.02	277.179	6.94

Table IX. TMA-LiPc H_2 self-diffusion coefficient

	ILD = 8.49 Å		ILD = 10 Å	
	Pres. (bar)	$\mathscr{D}_{H_2} \times 10^4$ (cm^2/s)	Pres. (bar)	$\mathscr{D}_{H_2} \times 10^4$ (cm^2/s)
T = 77 K	9.865	8.27	6.111	7.78
	22.141	3.08	8.354	2.59
	40.339	2.03	12.290	1.57
	70.534	1.34	19.765	1.28
T = 177 K	31.461	46.43	28.399	48.91
	79.282	19.30	67.149	19.27
	140.568	11.71	113.085	13.05
	213.286	7.99	163.624	9.30
T = 236 K	38.664	75.64	37.187	76.97
	98.816	29.23	90.741	33.77
	176.779	17.92	156.122	20.13
	267.588	13.09	227.347	14.91
T = 273 K	41.885	92.09	40.351	95.75
	107.715	35.43	102.602	40.88
	194.734	21.27	176.349	24.60
	295.434	16.41	258.219	18.60
T = 300 K	42.919	109.46	42.655	121.47
	113.656	41.56	108.440	43.14
	204.481	25.12	189.076	28.39
	312.345	17.29	277.179	20.39

Table X. TMA2-Pc H_2 adsorption isotherms

	ILD = 8.12 Å		ILD = 10 Å	
	Pres. (bar)	% (wt/wt)	Pres. (bar)	% (wt/wt)
T = 77 K	21.667	4.45	13.411	5.45
	51.071	5.18	26.404	6.08
	94.230	5.55	40.336	6.40
	135.822	5.99	54.931	6.61
T = 177 K	41.628	1.38	40.078	1.51
	106.920	2.41	95.922	2.76
	187.170	3.22	157.598	3.70
	274.361	3.93	214.370	4.45
T = 236 K	45.040	0.83	44.646	0.82
	121.257	1.64	113.812	1.87
	214.529	2.46	192.439	2.80
	321.729	3.15	271.388	3.60
T = 273 K	46.290	0.62	45.813	0.64
	127.518	1.29	120.726	1.52
	228.390	2.09	207.939	2.41
	343.152	2.78	298.069	3.19
T = 300 K	46.814	0.54	46.768	0.50
	129.726	1.17	124.135	1.35
	236.770	1.85	216.407	2.20
	357.051	2.55	313.351	2.95

Table XI. TMA2-Pc H_2 self-diffusion coefficient

	ILD = 8.12 Å		ILD = 10 Å	
	Pres. (bar)	$\mathscr{D}_{H_2}\times10^4$ (cm^2/s)	Pres. (bar)	$\mathscr{D}_{H_2}\times10^4$ (cm^2/s)
T = 77 K	21.667	12.07	13.411	11.36
	51.071	4.51	26.404	4.20
	94.230	2.35	40.336	2.59
	135.822	1.38	54.931	1.67
T = 177 K	41.628	41.71	40.078	43.84
	106.920	16.48	95.922	17.85
	187.170	9.77	157.598	11.88
	274.361	6.62	214.370	7.99
T = 236 K	45.040	56.42	44.646	57.29
	121.257	24.49	113.812	26.01
	214.529	15.04	192.439	17.04
	321.729	9.94	271.388	12.55
T = 273 K	46.290	69.74	45.813	70.26
	127.518	26.34	120.726	31.27
	228.390	16.63	207.939	20.12
	343.152	11.93	298.069	15.89
T = 300 K	46.814	72.55	46.768	81.28
	129.726	29.57	124.135	32.75
	236.770	18.90	216.407	22.01
	357.051	13.63	313.351	16.82

Table XII. TMA2-Pc Li ion binary diffusion coefficient

T = 273K			
Density (g/cm^3)	Concentration ×10^4 (mol/cm^3)	$\mathscr{D}_{Li}$×10^6 (cm^2/s)	$\mathscr{D}_{ClO_4}$×10^6 (cm^2/s)
0.729	4.591	4.752	2.790
0.708	2.582	2.461	2.662
0.717	3.443	1.344	1.434
0.705	2.295	2.039	2.659
0.699	1.722	1.902	1.819
T = 298K			
Density (g/cm^3)	Concentration ×10^4 (mol/cm^3)	$\mathscr{D}_{Li}$×10^6 (cm^2/s)	$\mathscr{D}_{ClO_4}$×10^6 (cm^2/s)
0.708	2.582	1.143	1.580
0.717	3.443	0.747	0.758
0.705	2.295	1.267	1.587
0.699	1.722	1.387	1.095
T = 313K			
Density (g/cm^3)	Concentration ×10^4 (mol/cm^3)	$\mathscr{D}_{Li}$×10^6 (cm^2/s)	$\mathscr{D}_{ClO_4}$×10^6 (cm^2/s)
0.729	4.591	3.705	3.364
0.717	3.443	0.680	1.747
0.699	1.722	2.618	3.807

VITA

Kevin Anthony Lamonte

Artie McFerrin Department of Chemical Engineering

Texas A&M University

College Station, TX 77843-3122

KevinL@tamu.edu

Education

Master of Science, Chemical Engineering, Texas A&M University, College Station, TX. May 2008.

Bachelor of Science, Computer Science, University of North Texas, Denton, TX. May 2000.

Work History

2004 to 2006. Research Assistant, Texas A&M University, College Station, TX. Designed and implemented onboard software for new generation of oceanographic buoys for the Texas Automated Buoy System.

1999 to 2004. Software Developer, IBM Corporation, Raleigh, NC. Professional software development.

The typist for this thesis was Kevin Lamonte.